Optical Metabolic Imaging to Characterize Early Treatment Response in Head and Neck Cancer

By

Amy Trushar Shah

Dissertation
Submitted to the Faculty of the
Graduate School of Vanderbilt University
in partial fulfillment of the requirements
for the degree of

DOCTOR OF PHILOSOPHY
in
Biomedical Engineering

August, 2016
Nashville, Tennessee

Approved:
Melissa C. Skala, Ph.D.
H. Charles Manning, Ph.D.
Rebecca S. Cook, Ph.D.
Rick R. Haselton, Ph.D.
Jill Gilbert, M.D.

To my family.

ACKNOWLEDGEMENTS

First, I would like to thank my advisor, Dr. Melissa Skala, for all her scientific and professional guidance throughout this dissertation work. I would also like to thank my committee members Dr. Charles Manning, Dr. Rebecca Cook, Dr. Rick Haselton, and Dr. Jill Gilbert for their complementary perspectives and insights toward this project. Additionally, I would like to thank all my collaborators, including Dr. Paula Pohlmann, Dr. Michelle Demory Beckler, Dr. Jonathan Irish, Kirsten Diggins, and Dr. Jim Higginbotham, for their valuable suggestions and for teaching me beneficial skillsets that were instrumental for these studies. Will Jones, as a high school student, and Taylor Cannon, as an undergraduate student, contributed toward cell culture assays and experiments. This work has used Vanderbilt core facilities, including the Translational Pathology Shared Resource, Cell Imaging Shared Resource, and Flow Cytometry Shared Resource. Additionally, the Cooperative Human Tissue Network was used for tissue collection. Funding sources for this work include the National Science Foundation (NSF) Graduate Research Fellowship. I would also like to thank all the graduate students in the Biophotonics Lab and Vanderbilt Biomedical Engineering department for their comradery. Finally, I would like to thank my parents and brother for their encouragement during this journey.

TABLE OF CONTENTS

Page

LIST OF TABLES

Table Page

LIST OF FIGURES

Figure Page

CHAPTER 1

INTRODUCTION

1.1 Motivation

Head and neck squamous cell carcinoma (HNSCC) is the sixth leading cancer by incidence in the world [1]. Each year, 500,000 new cases are diagnosed with a five-year survival rate between 40-50% [1]. Current standards of care for HNSCC patients include surgery, radiation therapy, and chemotherapy. However, surgeries often cause serious morbidities by impairing the ability to speak, chew, and swallow. Additionally, radiation therapy and chemotherapy introduce toxicities causing nausea, diarrhea, rash, dry mouth or thickened saliva, and changes in taste [2]. These negative side effects from HNSCC treatment justify the need for improved treatments and the development of biomarkers of early treatment efficacy.

Current treatments cure only 50-60% of HNSCC patients [3]. Measures of treatment response in HNSCC include x-ray computed tomography (CT), magnetic resonance imaging (MRI), and positron emission tomography (PET). However, these methods are only effective weeks to months after treatment begins and require contrast agents and/or expensive equipment. Additionally, tumor heterogeneity can contribute to treatment resistance, so single cell measurements would be beneficial to identify resistant cell subpopulations. Alternative treatment options for non-responders include re-irradiation, chemotherapy, or surgery [4]. Early predictors of drug efficacy would reduce toxicities, costs, and time associated with ineffective therapy. Therefore, there is a need for a cost-effective, noninvasive tool to determine treatment response at an early timepoint.

Therapeutic interventions for HNSCC include traditional chemotherapy and targeted inhibitors. Cisplatin is a common chemotherapy used in HNSCC [5]. In the past decade, targeted inhibitors have been developed to treat HNSCC. More than 90% of HNSCC cases exhibit upregulation of epidermal growth factor receptor (EGFR). The EGFR signaling pathway drives cell proliferation, growth, and survival. EGFR is the only proven molecular target for HNSCC therapy [4]. Cetuximab is a monoclonal antibody that inhibits EGFR activation, but clinical outcomes with cetuximab treatment have been poor and are not correlated with EGFR protein expression levels [6]. Improved technologies could guide the selection of drugs for individual patients so that alternative treatments can be administered.

The EGFR signaling pathway regulates cellular metabolism, including glycolysis and oxidative phosphorylation. Cancer often exhibits altered metabolism, particularly increased aerobic glycolysis (Warburg effect) [7], and metabolic pathways involve the autofluorescent cofactors NAD(P)H and FAD. The optical redox ratio and fluorescence lifetimes of NAD(P)H and FAD exploit intrinsic contrast to measure cellular metabolism at high resolution.

The overall goal of this dissertation is to enable improved response to therapy in head and neck cancer patients. Specifically, *in vitro* and *in vivo* models of head and neck cancer are treated with chemotherapy and targeted drugs, and endogenous fluorescence is measured from NAD(P)H and FAD, which are cofactors in glycolysis and oxidative phosphorylation. Ultimately, this technique could be applied to improve drugs and treatment regimens for head and neck cancer patients.

1.2 Specific Aims

A method to predict drug efficacy could enable optimal drug selection for individual HNSCC patients, thereby improving patient outcomes. Additionally, a method to monitor therapeutic effects at early timepoints after treatment onset would identify ineffective treatments. Molecular targets of HNSCC treatment include epidermal growth factor receptor (EGFR). EGFR participates in cellular signaling pathways that regulate metabolic cofactors including NAD(P)H and FAD, which are autofluorescent molecules involved in glycolysis and oxidative phosophorylation. The optical redox ratio is defined as the fluorescence intensity of NAD(P)H divided by that of FAD, and provides a global measure of metabolism. The fluorescence lifetime is a complementary optical measure that reports on the molecular microenvironment (protein-binding) of NAD(P)H and FAD. These fluorescence lifetimes and the optical redox ratio are parameters for "optical metabolic imaging".

Hypothesis: Optical metabolic imaging is sensitive to treatment response in HNSCC.

Aim 1 - *Characterize optical metabolic parameters in head and neck cancer cell lines early after treatment with approved and experimental drugs.* Feasibility will be established using human HNSCC cell lines. Cells will be treated with the clinically approved EGFR-targeting antibody cetuximab, the clinically approved chemotherapy cisplatin, or the experimental phosphoinositide 3-kinase (PI3K)/mammalian target of rapamycin (mTOR)-inhibitor BGT226 for 24 hours. NAD(P)H and FAD autofluorescence intensities and lifetimes will be characterized compared with control cells. Gold standard analysis will validate molecular targeting of cetuximab and BGT226 (western blot) and measure metabolic treatment response (lactate production/glucose consumption, proliferation).

Aim 2 - *Determine optical metabolic response to treatment in vivo in mouse xenografts using human head and neck cancer cells.* Male nu/nu mice will be injected with head and neck cancer cells. Once tumors reach ~100mm^3 the mice will be treated with cetuximab, cisplatin, or their combination. NAD(P)H and FAD autofluorescence intensities and lifetimes will be measured 48 hours after treatment, and cell subpopulation analysis will characterize tumor heterogeneity. Tumor growth over time, cell proliferation, and cell death will be used as gold standard measures of response.

Aim 3 – *Translate optical metabolic imaging to head and neck cancer patient tissues.* Human patient tissues of head and neck cancer will be acquired for *ex vivo* imaging. Samples will include tissue from multiple anatomical sites and cell types. Fluorescence lifetime images of NAD(P)H and FAD will probe tissue morphology and metabolism. Second harmonic generation (SHG) microscopy will image extracellular matrix composition, particularly collagen density and alignment.

Aim 4 - *Quantify optical metabolic parameters in organoid in vitro model of head and neck cancer after treatment.* Head and neck cancer xenografts will be excised, digested, and grown in culture (organoids). Metabolic phenotypes of organoids will be characterized alone and after treatment with cetuximab, cisplatin, or their combination. NAD(P)H and FAD autofluorescence intensities and lifetimes will be measured 24 hours after treatment. Additionally, cellular heterogeneity of organoids based on optical metabolic imaging parameters will be analyzed. Gold standard tumor response curves will be measured.

Impact: Optical metabolic imaging has potential to predict optimal drugs for HNSCC patients, enabling improved patient outcomes. Additionally, early measurement of response could identify ineffective treatment regimens, reducing unnecessary morbidities, toxicities, and costs.

1.3 Dissertation Outline

Chapter 1 explains the motivation behind this dissertation work. Chapter 2 provides relevant background information, particularly for head and neck cancer, methods for measuring treatment response, and optical techniques. The autofluorescence properties of NAD(P)H and FAD, as well as the roles of NAD(P)H and FAD in cell metabolism, are described. Chapter 3 characterizes optical metabolic imaging parameters, including the optical redox ratio and fluorescence lifetimes of NAD(P)H and FAD, in head and neck cancer cell lines after treatment with chemotherapy and targeted drugs. These optical parameters were compared with gold standard measures of cellular metabolism and therapeutic response. These studies provide a foundation for measurements in more complex systems. Chapter 4 shows feasibility of the optical redox ratio and fluorescence lifetime measurements of NAD(P)H and FAD *in vivo* for head and neck cancer xenografts to resolve response early after treatment. Chapter 5 translates optical metabolic imaging for *ex vivo* patient tissues of head and neck cancer. This study characterizes metabolic, morphologic, and structural properties on fresh, unprocessed human tissue from a variety of anatomical sites and cell types. Chapter 6 develops a protocol for generating three-dimensional organoid cultures from head and neck cancer tissue and characterizes the optical metabolic imaging properties of the organoids alone and after drug treatment. This type of physiologically-relevant *in vitro* model could provide a platform for streamlining drug discovery and predicting optimum treatments before administering drugs to individual patients. Chapter 7 presents the conclusions from this work, as well as future directions, contributions to the field, and broader impacts.

Appendices A and B include supplementary information for Chapters 4 and 6, respectively. Appendix C characterizes flow cytometry signals of cellular autofluorescence for

breast cancer cells with distinct phenotypes and applies flow sorting to separate heterogeneous samples into distinct cell subpopulations.

CHAPTER 2

BACKGROUND

Shah AT. 2013. Autofluorescence Imaging Reflects Metabolic Response to Treatment in Human Head and Neck Squamous Cell Carcinoma (Master's Thesis). Vanderbilt University

2.1 Anatomy and Physiology of the Head and Neck

The head and neck region includes the nasal cavity, oral cavity, pharynx, and larynx (Figure 2.1) [1]. These organs work together to perform critical functions, including chewing and swallowing food, speaking, and breathing.

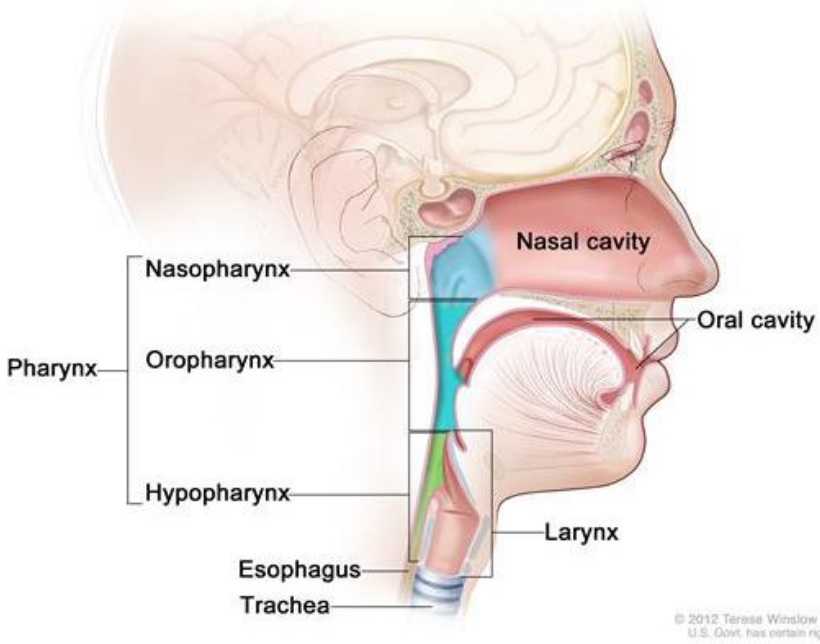

Figure 2.1. Anatomy of the head and neck region. Head and neck squamous cell carcinoma originates in squamous cells of the oral cavity, nasal cavity, pharynx, and larynx [8].

The oral cavity includes the lips, teeth, jaw, tongue, roof of the mouth, floor of the mouth, and salivary glands. The lips form the opening of the mouth and they are important in speech and containing food in the mouth. The tongue helps guide food and contains taste buds. The main function of the oral cavity is to chew and break down food mechanically using teeth and chemically using saliva produced by salivary glands.

The pharynx is a five-inch long tube located between the nose and the esophagus, and it consists of the nasopharynx, oropharynx, and hypopharynx. This cavity in the throat connects the nasal and oral cavities with the rest of the respiratory and digestive system, including the stomach, small intestine, and large intestine. Swallowing occurs in the pharynx, moving food from the mouth into the esophagus.

The larynx is situated below the pharynx. It is also called the voice box because it contains vocal chords that create sound and control pitch and volume. During swallowing, the larynx is elevated and the vocal chords move towards each other to move food through the esophagus and prevent it from going into the trachea, which leads to the lungs. The epiglottis, a layer of cartilage, moves over the laryngeal opening to prevent food from going into the respiratory pathways. The esophagus connects the pharynx to the stomach, where food is stored and broken down.

Prevalence and Diagnosis of Head and Neck Squamous Cell Carcinoma

Head and neck squamous cell carcinoma (HNSCC) originates in squamous cells of the oral cavity, nasal cavity, pharynx, and larynx. The hallmarks of cancer include evading apoptosis, self-sufficiency in growth signals, insensitivity to anti-growth signals, tissue invasion

and metastasis, and limitless replicative potential [9]. More than 90% of head and neck cancers are squamous cell carcinoma [10].

Incidence and mortality of HNSCC is correlated with long-term use of tobacco and alcohol. About 75% of HNSCC incidence occurs in men compared with 25% in women [11]. The stereotypical HNSCC patient is above 50 years old, but the younger population of HNSCC patients is increasing. In particular, this increase has been attributed to the prevalence of human papilloma virus (HPV), which affects about 25% of HNSCC cases [12][13]. Additionally, poor diet, particularly lacking vitamin A and iron, and poor oral hygiene can increase risk for developing HNSCC [14].

Early symptoms of HNSCC are usually vague. Symptoms of cancer in the oral cavity include persistent abnormal masses and sores [2]. Symptoms of cancer in the oropharynx, hypopharynx, and larynx include difficulty swallowing, sore throat, and hoarseness or other changes in voice quality. Symptoms of cancer in the nasal cavity include difficulty breathing through the nose and inflammation of the sinuses [15]. Screening is conducted using physical examination to inspect ulcers within the mouth and throat, palpation of the neck, and endoscopy. Additionally, magnetic resonance imaging (MRI), x-ray, and computed tomography (CT) can be used to detect HNSCC [16]. HNSCC is diagnosed by pathologic examination of surgical biopsy. Unfortunately, most cases are diagnosed at advanced stages, so effective treatment options are crucial to prevent unnecessary mortality and morbidity.

Treatment Methods for Head and Neck Cancer

Treatment techniques for HNSCC depend on the stage, location, and resectability of the primary tumor. Early stages are usually treated with surgery to remove tumor-containing tissue

and radiation, while advanced stages are treated with surgery and radiation in combination with chemotherapy, including cisplatin and fluorouracil (FU). Targeted therapies have also been investigated. HNSCC exhibits upregulation of epidermal growth factor receptor (EGFR) in more than 90% of cases [17]. EGFR activation leads to growth and proliferation of epithelial cells (Figure 2.2). Cetuximab is a monoclonal antibody that binds to EGFR, prevents activation, and leads to receptor degradation, and it has been used to inhibit EGFR-expressing tumors. Cetuximab is approved in combination with radiation therapy in patients with locally advanced HNSCC. However, since only a portion of patients respond to EGFR inhibitors, downstream targets have the potential to improve patient outcomes. Commonly mutated targets include phosphoinsitide 3-kinase (PI3K), signal transducer and activator of transcription 3 (STAT3), mammalian target of rapamycin (mTOR), Akt, vascular endothelial growth factor receptor (VEGFR), NF-κB, and human epidermal growth factor receptors 2 (HER2) and 3 (HER3) [18] [19].

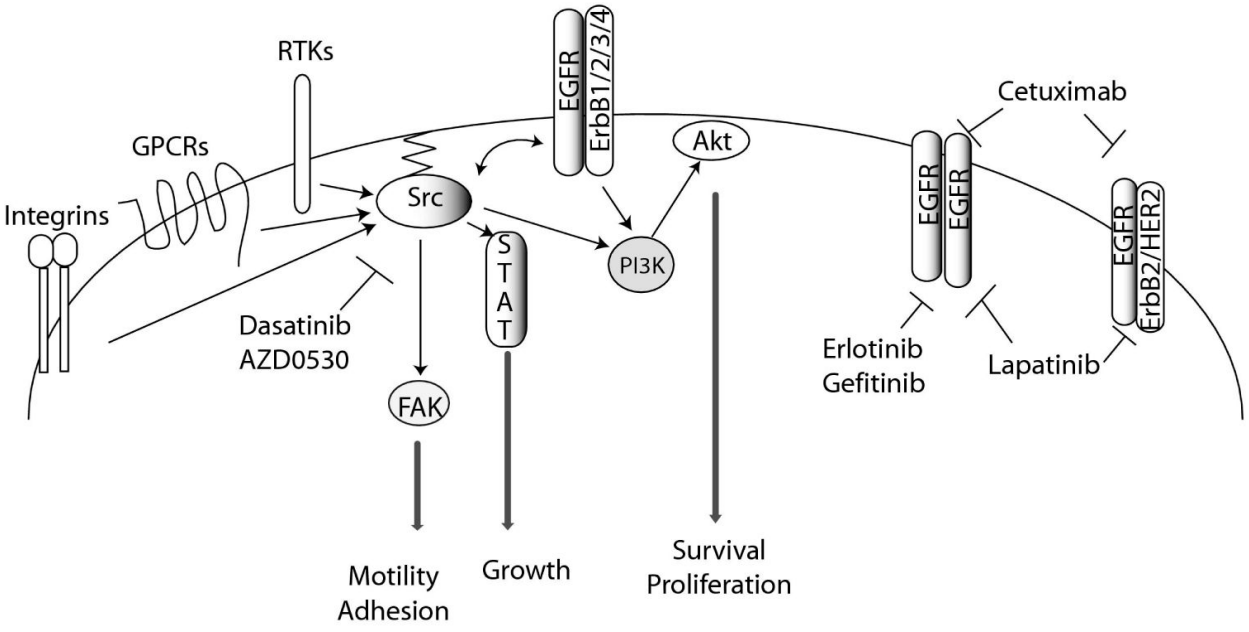

Figure 2.2. EGFR signaling pathway. EGFR activates pathways promoting cell survival and proliferation [20].

Current treatment options introduce toxicities and complications that impair the patient's quality of life. Surgeries often lead to serious morbidities, including difficulty or inability to speak and swallow, swelling, and changes in appearance. Therefore, organ preservation and function preservation are important considerations in HNSCC treatment. Additionally, radiotherapy and chemotherapy cause side effects, such as nausea, diarrhea, rash, dry mouth or thickened saliva, or changes in taste [2]. HNSCC can be aggressive depending on the location and proximity to lymph nodes, increasing the capability to metastasize [21]. The 5-year survival rate for HNSCC patients is between 40-50% [1]. Despite advancements and improvements in surgical techniques, chemotherapy, and radiation delivery, long-term survival has not improved [22]. The current standard to measure cancer treatment response includes whole-body imaging methods, like CT, x-ray, MRI, and positron emission tomography (PET).

Optical Techniques for Head and Neck Squamous Cell Carcinoma

HNSSC is an ideal target for optical imaging because of easy access to the site using fiber optic probes [23][24]. Additionally, fiber optics can be incorporated into endoscopes that are currently in use.

Optical techniques have been investigated to detect HNSCC. High-resolution microendoscopic imaging has been used to distinguish cancerous versus benign sites for assessing tumor margins in surgery for HNSCC [23]. Reflectance spectroscopy using polarized light has also been shown to non-invasively extract morphologic information to detect neoplasia in epithelial tissue phantoms and oral tissue *in vivo* [25]. Additionally, fluorescence spectroscopy has been shown to identify oral neoplasias with sensitivities and specificities greater than 88% [26]. Muller, *et al.* combined intrinsic fluorescence spectroscopy, diffuse reflectance

spectroscopy, and light scattering spectroscopy and achieved a sensitivity and specificity of 96% and 96% in distinguishing dysplasia from normal tissue in HNSCC patients [27]. Contrast agents, particularly acetic acid, and blue-white light have been used to identify premalignancy in the oral cavity, but clinical studies will be required to determine the sensitivity and specificity of these techniques [28]. Furthermore, the autofluorescence intensity of NAD(P)H and FAD has been used to distinguish normal from dysplasia in oral tissue [29], and the NAD(P)H and FAD fluorescence lifetimes have been shown to identify precancer compared with normal in the DMBA-treated hamster cheek pouch model [30][31][32][33]. Optical coherence tomography has also been applied with fluorescence lifetime imaging to discriminate normal from cancer in the hamster cheek pouch [34]. Multiphoton microscopy of endogenous fluorescence has been used to quantify cellular and tissue morphology in the DMBA-treated hamster cheek pouch model [35][36].

Attempts have been made to monitor treatment response in HNSCC using fluorescently-labeled antibodies. In one study, mice with HNSCC xenografts treated with fluorescently-labeled cetuximab decreased in tumor volume, but tumor fluorescence did not correlate with response to treatment [37]. Gleysteen *et al.* used a similar approach of growing xenografts and treating the mice with fluorescently labeled cetuximab, cisplatin, and radiation. They found no change among fluorescence intensity before treatment, after six weeks of treatment, or at ten weeks of treatment, although tumor regression was observed based on histological analysis. This indicates that fluorescence intensity of labeled cetuximab does not reflect tumor response [38]. However, endogenous fluorescence has not been studied to measure treatment response in HNSCC.

Two-Photon Fluorescence Microscopy and Fluorescence Lifetime Imaging

Light can be described as packets of energy in photons. Fluorescence occurs when a molecule absorbs a photon of a particular energy and emits a photon of a different energy [39]. This absorption excites the molecule from the ground state, S, to the excited state, S*, and upon relaxation the emitted light has an energy less than the absorbed energy (Figure 2.3). Energy and wavelength are inversely related according to $E = hc/\lambda$, where E represents energy, h represents Planck's constant, λ represents wavelength, and c represents the speed of light. Therefore, a lower energy corresponds to a longer wavelength. Endogenous fluorophores, including NAD(P)H, FAD, tryptophan, collagen, and elastin, occur naturally in the body, and probing these can eliminate the need for dyes or contrast agents [40].

Two-photon excitation occurs by simultaneous absorption of two photons with half the energy required for single-photon excitation (Figure 2.3) [41]. Photons with half the energy correspond to twice the wavelength. Most endogenous fluorophores are excited in the ultraviolet (UV) to visible range (~300-500nm), so therefore two-photon excitation uses near-infrared (NIR) light (~700-900nm) for excitation [40]. UV or visible light is constrained to a penetration depth of about 100μm below tissue surface, whereas decreased scattering and absorption for NIR light allows for deeper penetration [42]. Additionally, since the absorption of two photons is required for excitation, sufficient photon flux is only present at the focal point, whereas single-photon excitation can produce fluorescence outside the focal point due to scattering (Figure 2.4). This allows for precise depth-sectioning and elimination of out-of-focus signal.

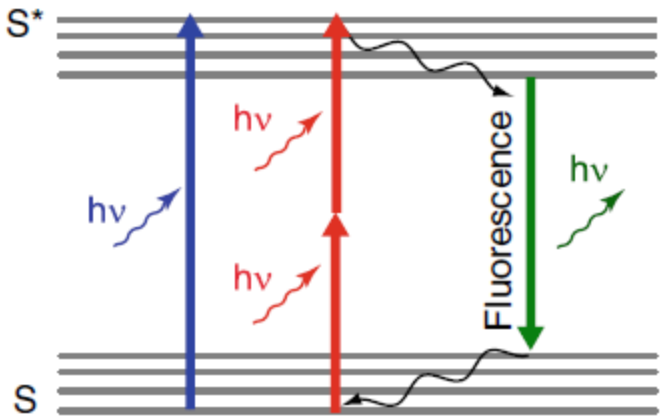

Figure 2.3. Absorption and fluorescence emission energy diagram. Single-photon (blue) and two-photon (red) excitation causes fluorescence emission (green) [43].

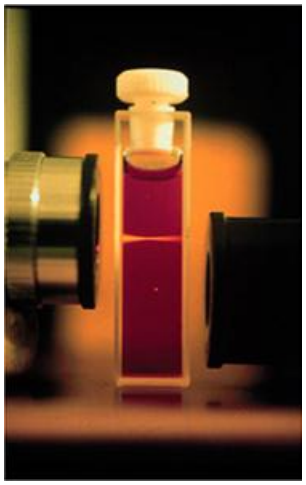

Figure 2.4. Comparison between single-photon and two-photon excitation. Single-photon fluorescence causes excitation at the focal point and outside the focal point (top), whereas two-photon fluorescence causes excitation only at the focal point (bottom) [44].

Fluorescence lifetime imaging probes the amount of time that a fluorophore is in the excited state before relaxing to the ground state [39][45]. The lifetime is sensitive to the microenvironment, including protein-binding, pH, and oxygen. In particular, the lifetime

discriminates between free and protein-bound conformations of molecules. To calculate the lifetime, a histogram of the lifetime events is plotted and fit to an exponential curve. The number of components in the exponential curve depends on the number of molecular species or binding configurations present. For example, NAD(P)H and FAD exist in free and protein-bound conformations, so these lifetime histograms are fit to a two-component exponential function: $F(t) = \alpha_1 e^{-t/\tau 1} + \alpha_2 e^{-t/\tau 2}$, where F represents the fluorescence as a function of time, α represents the contribution from each component and τ represents the lifetime of each component (Figure 2.5). The lifetime occurs on the order of picoseconds to nanoseconds. Applying two-photon fluorescence and fluorescence lifetime imaging of the metabolic cofactors NAD(P)H and FAD can provide insight into cellular metabolism and microenvironment *in vitro* and *in vivo* [46].

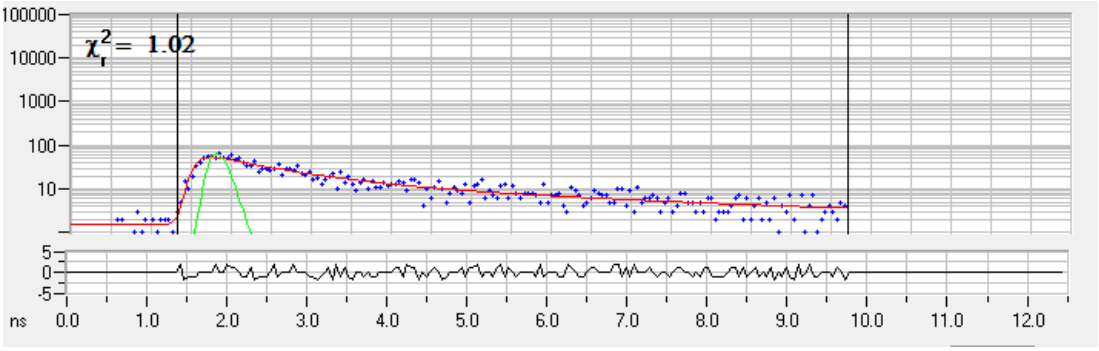

Figure 2.5. Fluorescence lifetime decay curve. The fluorescence lifetime is calculated by fitting the lifetime events (blue) to an exponential function (red).

Cellular Metabolism and Tumor Heterogeneity

During glycolysis, NAD^+ is reduced to nicotinamide adenine dinucleotide (NADH) (Figure 2.6). During oxidative phosphorylation, NADH is oxidized to NAD^+ and $FADH_2$ is oxidized to flavin adenine dinucleotide (FAD). NADH and FAD exhibit autofluorescence, whereas NAD^+ and $FADH_2$ do not. Additionally, NADH and FAD can be separated spectrally

based on their optimal excitation and emission wavelengths. NADPH exhibits similar fluorescence excitation and emission properties as NADH, so fluorescence from these molecules is termed NAD(P)H. NADPH is expected to contribute a low background signal because the concentration of NADH is about 5 times higher than NADPH [47], NADH has a 1.25 to 2.5 times higher quantum yield than NADPH [48], and metabolic perturbations have been shown to primarily affect NADH [49].

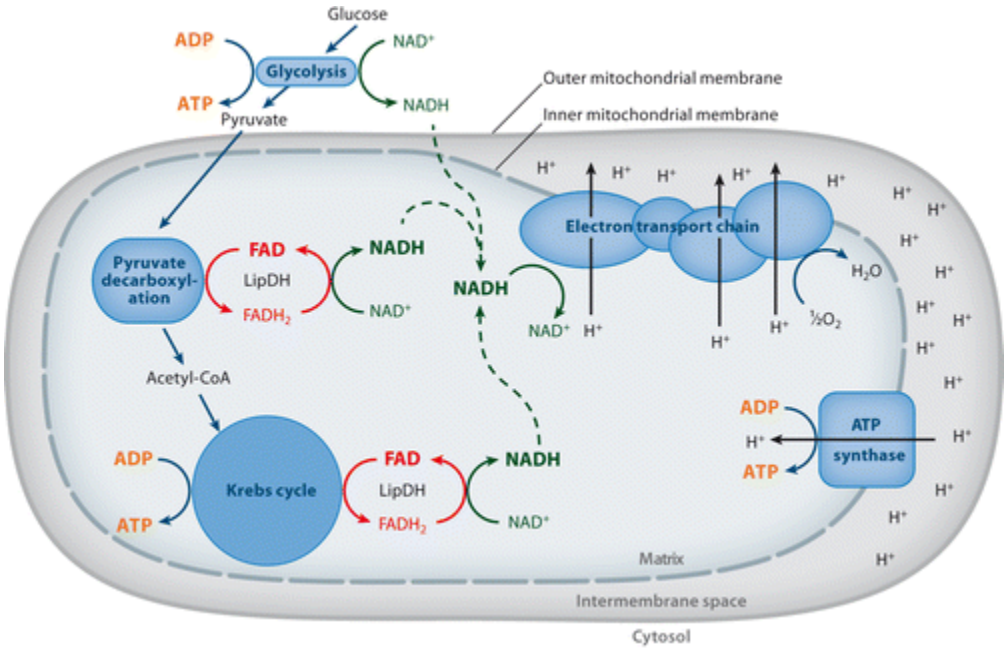

Figure 2.6. The role of NADH and FAD in cellular metabolism. Glycolysis occurs in the cell cytoplasm, whereas the Kreb's cycle and the electron transport chain occur in the mitochondria [50].

The optical redox ratio, defined as the fluorescence intensity of NAD(P)H divided by the fluorescence intensity of FAD is an established method for probing cellular metabolism [46][51][52]. For example, the redox ratio has been shown to be higher for cancer cells

compared with nonmalignant cells [53], which can be attributed to increased aerobic glycolysis in cancer. As a more sensitive measure, the fluorescence lifetime is the time a fluorophore stays in the excited state before relaxing to the ground state and reflects fluorophore microenvironment, including protein-binding and preferred metabolic pathways [39]. These measurements are advantageous because they use intrinsic contrast to probe cellular metabolism and can be applied on a single cell level.

Tumors can contain multiple subpopulations of cancer cells with different phenotypes and sensitivities to treatment [54][55], and this tumor heterogeneity can impact treatment response. In particular, subpopulations of cells that are resistant to treatment can continue to proliferate after therapy and be responsible for patient relapse. For example, previous work has shown that a minority subset of cells can drive tumor growth in HNSCC [56]. However, current methods for planning treatment regimens include targeting the majority population of cells [57]. Therefore, single cell measurements have potential to resolve cellular subpopulations and identify treatment-resistant cells that drive patient relapse.

CHAPTER 3

OPTICAL METABOLIC IMAGING OF TREATMENT RESPONSE IN HUMAN HEAD AND NECK SQUAMOUS CELL CARCINOMA

Shah AT, Demory Beckler M, Walsh AJ, Jones WP, Pohlmann PR, Skala MC. "Optical Metabolic Imaging of Treatment Response in Human Head and Neck Squamous Cell Carcinoma." PLOS ONE, 2014; 9(3) e90746

3.1 Abstract

Optical metabolic imaging measures fluorescence intensity and lifetimes from metabolic cofactors nicotinamide adenine dinucleotide (NADH) and flavin adenine dinucleotide (FAD). These molecular level measurements provide unique biomarkers for early cellular responses to cancer treatments. Head and neck squamous cell carcinoma (HNSCC) is an attractive target for optical imaging because of easy access to the site using fiber optic probes. Two HNSCC cell lines, SCC25 and SCC61, were treated with Cetuximab (anti-EGFR antibody), BGT226 (PI3K/mTOR inhibitor), or cisplatin (chemotherapy) for 24 hours. Results show increased redox ratio, NADH α_1 (contribution from free NADH), and FAD α_1 (contribution from protein-bound FAD) for malignant cells compared with the nonmalignant cell line OKF6 ($p<0.05$). In SCC25 and SCC61 cells, the redox ratio is unaffected by cetuximab treatment and decreases with BGT226 and cisplatin treatment ($p<0.05$), and these results agree with standard measurements of proliferation rates after treatment. For SCC25, NADH α_1 is reduced with BGT226 and cisplatin treatment. For SCC61, NADH α_1 is reduced with cetuximab, BGT226, and cisplatin treatment. Trends in NADH α_1 are statistically similar to changes in standard measurements of glycolytic

rates after treatment. FAD α_1 is reduced with cisplatin treatment ($p<0.05$). These shifts in optical endpoints reflect early metabolic changes induced by drug treatment. Overall, these results indicate that optical metabolic imaging has potential to detect early response to cancer treatment in HNSCC, enabling optimal treatment regimens and improved patient outcomes.

3.2 Introduction

Head and neck squamous cell carcinoma (HNSCC) is the sixth leading cancer by incidence in the world [1]. Each year, 500,000 new cases are diagnosed with a five-year survival rate between 40-50% [1]. Current standards of care for HNSCC patients involves multidisciplinary care, including surgery, radiation therapy, chemotherapy, and rehabilitation. Treatment is intense since it is frequently delivered with curative aims. Resultant toxicities comprise nausea, vomiting, diarrhea, neuropathy, skin rash, dry mouth or thickened saliva, changes in taste, hypothyroidism, as well as impaired ability to speak, chew, and swallow [2][58][59]. These negative side effects from HNSCC treatment justify the need for improved treatments and the development of biomarkers of early treatment efficacy.

Current measures of treatment response in HNSCC include physical examination with endoscopy, x-ray computed tomography (CT), magnetic resonance imaging (MRI), and positron emission tomography (PET). Deep invasion of tumor and subtle changes to its dimensions during different treatment phases may not be measurable by physical exam. Imaging studies are only effective weeks to months after treatment begins and require contrast agents and/or expensive equipment. Therefore, these methods have low sensitivity to detect beneficial effects of treatment before several weeks have elapsed since treatment onset. Alternative treatment options for non-responders include re-irradiation, chemotherapy, or surgery [4]. Early predictors of drug efficacy

would reduce toxicities, costs, and time associated with ineffective therapy. Therefore, there is a need for a cost-effective, noninvasive tool to determine treatment response at an early time point.

Therapeutic interventions for HNSCC include traditional chemotherapy and molecularly targeted inhibitors. Cisplatin is a common chemotherapy used in HNSCC [5]. In the past decade, targeted inhibitors have been developed to treat a number of solid tumors, including HNSCC. More than 90% of HNSCC cases exhibit upregulation of epidermal growth factor receptor (EGFR). The EGFR signaling pathway drives cell proliferation, growth, and survival. EGFR is the only proven molecular target for HNSCC therapy [4]. Cetuximab is a monoclonal antibody that effectively occludes ligand binding to EGFR, thereby inhibiting receptor activation, but clinical outcomes with cetuximab treatment vary and are not correlated with EGFR protein expression levels [6]. Therefore, downstream effectors, including phosphatidylinositol 3-kinase (PI3K) and mammalian target of rapamycin (mTOR), have been investigated as potential therapeutic targets. PI3K, a master regulator of metabolism, is mutated in about 37% of HNSCC [60]. BGT226 is a PI3K/mTOR inhibitor currently under clinical investigation for solid tumors [61]. However, there is a need for improved technologies to guide the selection of drugs for individual patients, so that alternative treatments such as BGT226 can be used at an early time point.

The EGFR and PI3K/mTOR signaling pathways regulate cellular metabolism, including glycolysis and oxidative phosphorylation [62]. Cancer often exhibits altered metabolism, particularly increased aerobic glycolysis (Warburg effect) [7]. During glycolysis, NAD^+ is reduced to nicotinamide adenine dinucleotide (NADH). During oxidative phosphorylation, NADH is oxidized to NAD^+ and $FADH_2$ is oxidized to flavin adenine dinucleotide (FAD). NADH and FAD exhibit autofluorescence, whereas NAD^+ and $FADH_2$ do not. The optical redox

ratio, defined as the fluorescence intensity of NADH divided by the fluorescence intensity of FAD, reflects relative amounts of glycolysis compared with oxidative phosphorylation and is an established method for probing cellular metabolism [46][51][52]. The fluorescence lifetime is the time a fluorophore stays in the excited state before relaxing to the ground state and reflects fluorophore microenvironment, including protein-binding and preferred metabolic pathways [39]. The optical redox ratio and fluorescence lifetimes of NADH and FAD exploit intrinsic contrast to measure optical endpoints of cellular metabolism. Furthermore, metabolic endpoints show particular promise because shifts in cellular metabolism often occur sooner than changes in tumor volume or glucose uptake.

Tissue autofluorescence has been previously used to detect HNSCC. The autofluorescence intensity of NADH and FAD has been used to distinguish normal from dysplasia in oral tissue [29], and the NADH and FAD fluorescence lifetimes have been shown to identify precancer compared with normal in the DMBA-treated hamster cheek pouch model [31][32][33][30]. Multiphoton microscopy of endogenous fluorescence has been used to quantify cellular and tissue morphology in the DMBA-treated hamster cheek pouch model [35][36]. However, no previous literature has characterized endogenous fluorescence in response to treatment in HNSCC. Fluorescent dyes have been used to monitor anti-EGFR antibody uptake in HNSCC, but results did not reflect response *in vivo* [37][38]. Optical metabolic imaging is sensitive to early metabolic shifts after cancer treatment and has potential to noninvasively detect treatment response sooner than current methods.

The serious morbidities and toxicities from HNSCC treatment, as well as treatment failures, justify the need for early predictors of treatment efficacy. This study tests the hypothesis that autofluorescence from metabolic cofactors NADH and FAD can resolve response to targeted

therapies and chemotherapy in HNSCC. Optical metabolic imaging was performed on two HNSCC cell lines, SCC25 and SCC61, treated for 24 hours with targeted drugs (cetuximab or BGT226) or chemotherapy (cisplatin). HNSCC is an ideal site for optical imaging because of easy access to the site with fiber optic probes. These results indicate that optical metabolic imaging has potential to expedite drug screenings, develop optimal treatments, and improve patient outcomes for HNSCC.

3.3 Materials and Methods

Cell Culture and Reagents

The TERT-immortalized human oral keratinocyte line OKF6/TERT-1 (OKF6) [63], the squamous cell carcinoma line SCC25 [64][65][66][67], and the squamous cell carcinoma line SCC61 [66] were acquired from J. Rheinwald and the Cell Culture Core of the Harvard Skin Disease Research Center, Boston, MA. OKF6 cells were cultured in keratinocyte serum-free medium (GIBCO K-sfm; Invitrogen) supplemented with 25µg/ml bovine pituitary extract, 1% penicillin/streptomycin, 0.2ng/ml epidermal growth factor, and 0.3mM $CaCl_2$. SCC25 and SCC61 cells were cultured in DMEM/F12 media (Invitrogen) supplemented with 10% fetal bovine serum and 0.4µg/ml hydrocortisone (Sigma).

For fluorescence imaging, 10^5 cells were plated on 35 mm glass-bottomed dishes (MatTek Corp.). The media was replaced 24 hours after plating with control media or treatment media containing 13nM cetuximab (Vanderbilt Pharmacy), 300nM NVP-BGT226 (Selleckchem), or 176µM cisplatin (Selleckchem). The drug doses were chosen to be 11 times the IC50 for each drug [3] [68] [69]. The cells were imaged 24 hours after treatment.

Imaging Instrumentation

Fluorescence lifetime images were collected using a custom-built multi-photon fluorescence microscope (Prairie Technologies). Images were acquired through an inverted microscope (TiE, Nikon) with a 40x oil immersion objective (1.3 NA). Fluorescence was excited using a titanium:sapphire laser (Chameleon, Coherent Inc.) and collected using a GaAsP photomultiplier tube (H7422P-40, Hamamatsu). NADH and FAD images were acquired sequentially for the same field of view. NADH fluorescence was isolated using an excitation wavelength of 750nm and an emission bandpass filter of 400-480nm. FAD fluorescence was isolated using an excitation wavelength of 890nm and an emission bandpass filter of 500-600nm. The average power incident on the sample was approximately 10mW. The acquired images consisted of 256 x 256 pixels (170μm x 170μm) with a 4.8μs pixel dwell time. Time-correlated single photon counting (TCSPC) electronics (SPC-150, Becker and Hickl) were used to collect fluorescence lifetime images over 60 seconds. The approximate rate of photon counting was $1\text{-}2*10^5$ photons/second. The absence of photobleaching was confirmed by monitoring photon count rates throughout image acquisition.

The instrument response function (IRF) was measured from second harmonic generation of urea crystals excited at 900nm, and the full width at half maximum (FWHM) was calculated to be 244 ps. A Fluoresbrite YG microsphere (Polysciences Inc.) was imaged as a daily standard. The lifetime decay curves were fit to a single exponential decay and the fluorescence lifetime was measured to be 2.13 ± 0.28ns (n=7), which is consistent with published values [32][70].

Cyanide Perturbation

The OKF6 cells were plated at a density of 10^5 cells per 35 mm glass-bottomed dish (MatTek Corp.). After 48 hours, fluorescence lifetime images of NADH and FAD were acquired. Then, the media was replaced with cyanide-supplemented media (4mM NaCN, Sigma). After five minutes of cyanide treatment, fluorescence lifetime images of NADH and FAD were acquired.

Image Analysis

Fluorescence lifetime images were analyzed using SPCImage software (Becker and Hickl). Binning included the selected pixel and the eight surrounding pixels. The fluorescence lifetimes were calculated by de-convolving the measured fluorescence decay curve with the IRF and fitting to a two-component exponential curve, $F(t) = \alpha_1 e^{-t/\tau 1} + \alpha_2 e^{-t/\tau 2} + c$. F(t) represents the fluorescence intensity as a function of time after the excitation pulse, τ_1 and τ_2 represent the short and long fluorescence lifetimes, respectively, α_1 and α_2 represent the contribution from each lifetime component ($\alpha_1+\alpha_2=1$), and c represents background light. A two-component decay curve was chosen to represent free and protein-bound conformations of NADH and FAD [32]. The weighted mean lifetime, τ_m, was calculated, $\tau_m = \alpha_1\tau_1+\alpha_2\tau_2$. The photon counts per pixel were summed over the 60 second collection time to calculate a fluorescence intensity image. A threshold was applied to exclude fluorescence from background and cell nuclei. The fluorescence intensities and lifetime values were imported into MATLAB (Mathworks) for further quantification. Redox ratio images were calculated by dividing the fluorescence intensity image of NADH by the fluorescence intensity image of FAD for the same field of view, and the average per image was computed. The redox ratio was normalized to control cells for comparing treatment groups within cell lines. The redox ratio was normalized to the nonmalignant OKF6

cells when comparing between cell lines. Average fluorescence lifetime values were calculated per image. For the control groups 30 images were analyzed, and for the treatment groups 18 images were analyzed.

Western Blotting Analysis

Cells were plated at $3*10^6$ cells per 10cm dish. After 24 hours, the media was removed, the cells were washed three times with phosphate buffered saline (PBS), and serum-free media was added. After another 24 hours, the media was replaced with treatment media for one hour. For the groups treated with epidermal growth factor (EGF) or transforming growth factor alpha (TGF-α), 10ng/mL EGF or TGF-α was added for 5 minutes. The cells were lysed with lysis buffer (1% Triton X-100, 10% Glycerol, 50 mM HEPES pH 7.2, and 100 mM NaCl) supplemented with sodium orthovanadate and protease inhibitor cocktail. Proteins were separated using a 10% SDS-PAGE separation gel at 100V. The gel was transferred at 27V overnight to a PVDF membrane. The membrane was blocked using 5% bovine serum albumin (BSA) for one hour and then incubated in the following primary antibodies overnight: EGFR (Millipore, 1:1000), pY1173 EGFR (Cell Signaling, 1:250), AKT (Cell Signaling, 1:250), pS473 AKT (Cell Signaling, 1:250), or GAPDH (Sigma, 1:1000). Membranes were washed four times, secondary antibodies were added for one hour, and electrogenerated chemiluminescence (ECL) was used to measure luminescence.

Proliferation Assay

Cells were plated in a 96 well plate at $3.3*10^3$ cells per well. Four wells per treatment group were plated. After 24 hours, the media was replaced with treatment media supplemented with

10μM BrdU. The cells incubated for 24 hours and then were fixed with 4% paraformaldehyde for 15 minutes. The cells were washed twice with PBS and permeabilized with 0.3% Triton X in PBS for 15 minutes. The DNA was denatured using hydrochloric acid, and the cells were blocked using 10% goat serum and 0.3% Triton X for one hour. Primary antibody (rat anti-BrdU, Abcam, 1:100) was incubated overnight. The cells were washed three times with PBS and incubated in secondary antibody (DyLight594-conjugated goat anti-rat, Jackson Immunoresearch, 1:200) for two hours. The cells were washed three times with PBS and counterstained with Hoechst 33528 (1:1000) for 10 minutes. Fluorescence images were acquired for three fields of view per well (n=12), and the number of cells per image was counted (ImageJ).

Glucose and Lactate Assays

Cells were plated at a density of 10^5 cells per 35 mm dish, and 24 hours later the media was replaced with treatment media. After 24 hours of treatment, glucose and lactate concentrations from four samples per group were measured according to the protocols of commercially available kits (Invitrogen; Eton Biosceience).

Statistical Analyses

Bar graphs are represented as mean ± standard error. Statistical significance was determined using two-way Wilcoxon rank sum tests in MATLAB (Mathworks). A p-value less than 0.05 indicated statistical significance.

3.4 Results

Redox ratio validation was performed by perturbing nonmalignant OKF6 cells with 4mM cyanide, which prevents oxidation of NADH to NAD^+ in the electron transport chain [71]. This accumulation of NADH causes an increase in the optical redox ratio (Figure 3.1a) and verifies isolation of NADH and FAD fluorescence. The contribution from free NADH (α_1) increases with cyanide treatment (Figure 3.1b), causing a decreased NADH mean lifetime (data not shown). The contribution from protein-bound FAD (α_1) decreases with cyanide treatment (Figure 3.1c), causing an increased FAD mean lifetime (data not shown).

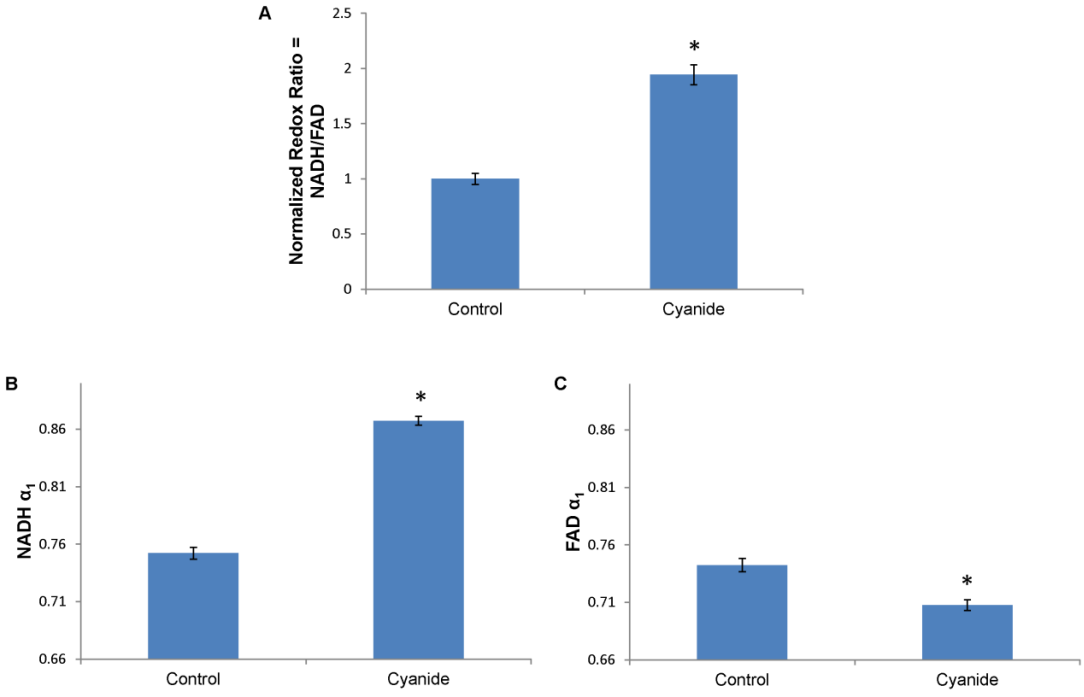

Figure 3.1. Cyanide treatment alters redox ratio, NADH α_1, and FAD α_1 in nonmalignant oral cells (OKF6). (a) Cyanide treatment (4mM) disrupts the electron transport chain, causing an increase in the optical redox ratio. (b) Cyanide treatment increases the contribution of free NADH (α_1) and (c) decreases the contribution of protein-bound FAD (α_1). * $p<0.05$, rank sum test; mean ± SEM.

The optical metabolic endpoints differentiate the malignant cell lines, SCC25 and SCC61, from the nonmalignant cell line, OKF6 (Figure 3.2). The malignant cell lines showed an increased redox ratio compared with the OKF6 cells ($p<0.05$). The malignant cell lines showed increased NADH α_1 compared with the OKF6 cells ($p<0.05$) and increased FAD α_1 compared with the OKF6 cells ($p<0.05$), suggesting differences in metabolic pathways between the malignant and nonmalignant cells.

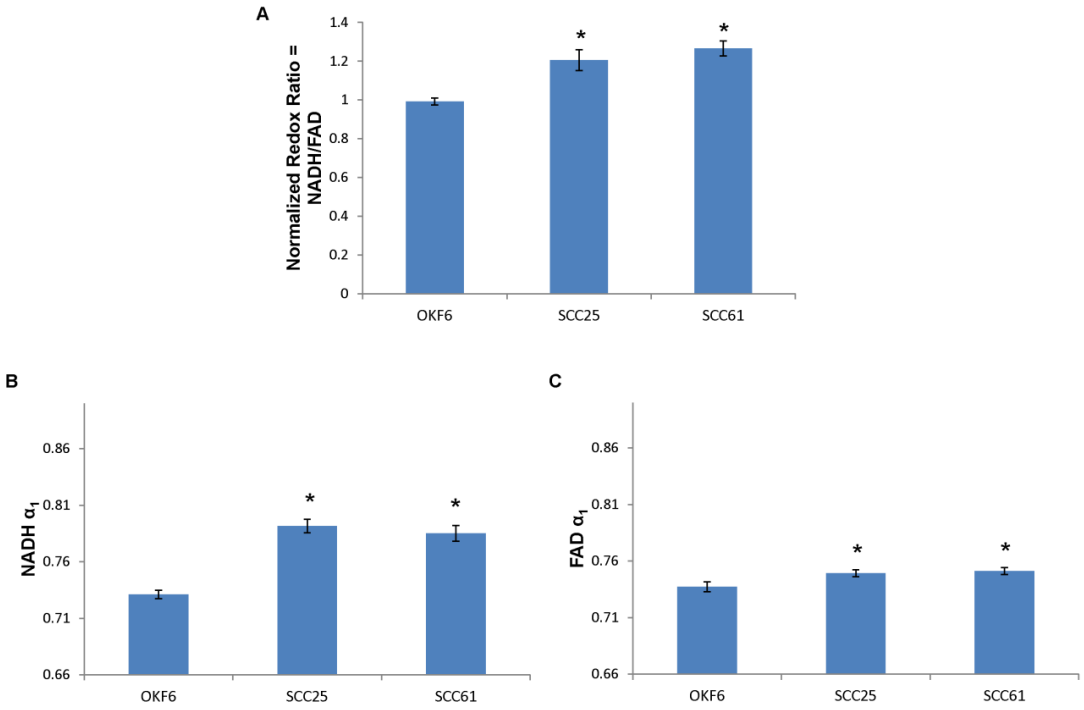

Figure 3.2. Optical metabolic endpoints distinguish malignant from nonmalignant cells. (a) The normalized redox ratio increases for the malignant cell lines (SCC25 and SCC61) compared to nonmalignant cells (OKF6), indicating increased glycolysis compared with oxidative phosphorylation. (b-c) The contribution of free NADH and protein-bound FAD (α_1) increase for the malignant cell lines compared with the nonmalignant cell line, reflecting shifts in metabolic pathways. * $p<0.05$, rank sum test; mean ± SEM.

Western blotting analysis was used to ensure target inhibition (Figure 3.3). Cetuximab targeting of EGFR was assessed by measuring phosphorylated tyrosine (Y) 1173 of EGFR (pEGFR), which is absent with cetuximab treatment. BGT226 targeting of PI3K/mTOR was assessed by measuring phosphorylated serine (S) 473 of Akt (pAkt) because PI3K and mTOR activation drive Akt activation in the PI3K/Akt signaling pathway. pAkt is absent with BGT226 treatment. These results indicate that cetuximab and BGT226 target EGFR and PI3K/mTOR, respectively. Western blotting analysis was also performed to characterize the SCC25 and SCC61 cell lines (not shown). SCC61 cells showed increased pAkt, reflecting upregulated PI3K, and agreeing with published results [72]. Additionally, SCC61 cells exhibited increased EGFR and pEGFR compared with SCC25 cells.

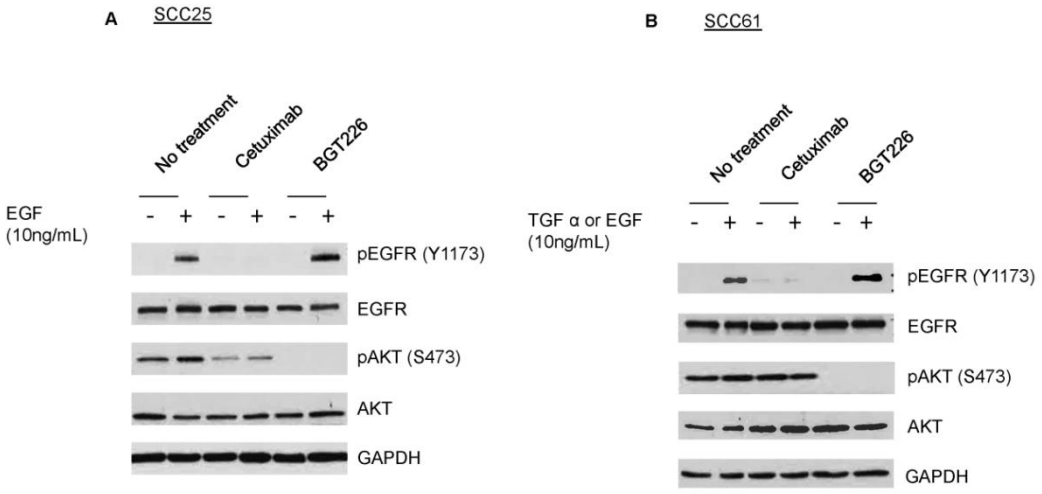

Figure 3.3. Western blotting analysis verifies molecular targeting of cetuximab and BGT226. Western blot for (a) SCC25 and (b) SCC61 cells. Epidermal growth factor (EGF) and transforming growth factor alpha (TGF α) activate the epidermal growth factor receptor (EGFR) and AKT pathways. Treatment with cetuximab decreases phosphorylated EGFR (pEGFR), and treatment with BGT226 decreases phosphorylated AKT (pAKT).

Representative images of SCC25 and SCC61 cells after 24 hours of treatment provide qualitative visualization of the redox ratio, NADH α_1, and FAD α_1 (Figure 3.4). NADH and FAD fluorescence from the cytoplasm was quantified across treatment groups and cell lines. The redox ratios of SCC25 and SCC61 cells show no significant changes with cetuximab treatment, and decrease with BGT226 and cisplatin treatment (Figure 3.5a). The fluorescence lifetimes of NADH and FAD reflect cellular microenvironment and protein-binding. NADH α_1 represents the contribution from free NADH. For SCC25 cells, NADH α_1 decreases with BGT226 and cisplatin treatment. For SCC61 cells, NADH α_1 decreases with cetuximab, BGT226, and cisplatin treatment (Figure 3.5b). FAD α_1 represents the contribution from protein-bound FAD. For SCC25 and SCC61 cells, FAD α_1 decreases with cisplatin treatment (Figure 3.5c). Combined, these data show that optical metabolic endpoints are sensitive to treatment with cetuximab, BGT226, and cisplatin in SCC25 and SCC61.

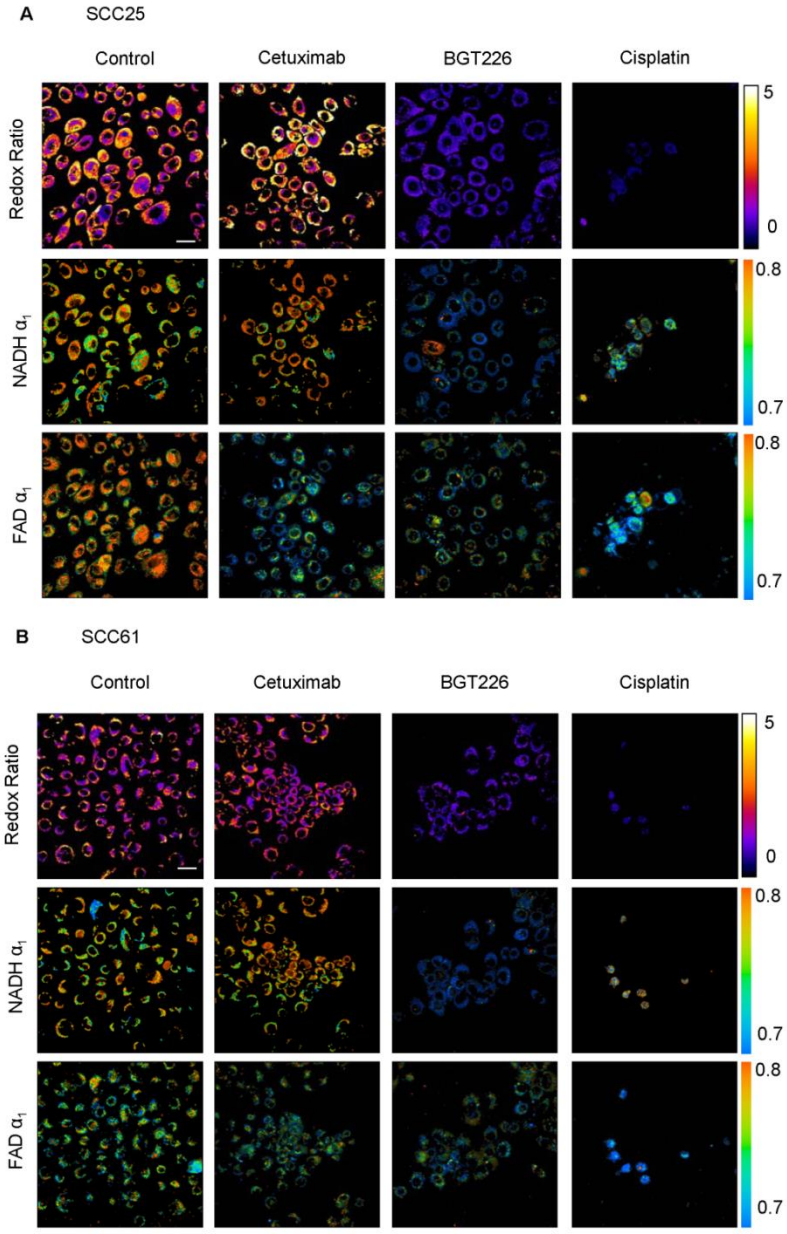

Figure 3.4. Representative autofluorescence images after treatment. Representative images of the redox ratio (1st row), NADH α_1 (2nd row), and FAD α_1 (third row) for (a) SCC25 cells and (b) SCC61 cells treated with control (1st column), cetuximab (2nd column), BGT226 (3rd column), or cisplatin (4th column). α_1 quantifies the short lifetime component ($\alpha_1+\alpha_2=1$). NADH α_1 represents the contribution from free NADH, while FAD α_1 conversely represents the contribution from protein-bound FAD. Scale bar represents 30um.

Proliferation was quantified as a standard measure of treatment response. Cetuximab treatment does not induce a statistically significant effect on proliferation, whereas BGT226 and cisplatin treatment decrease proliferation (Figure 3.5d). Additionally, glycolytic rates were quantified after treatment. SCC25 shows decreased lactate production/glucose consumption with BGT226 and cisplatin treatment, and SCC61 shows decreased lactate production/glucose consumption with cetuximab, BGT226, and cisplatin treatment (Figure 3.5e).

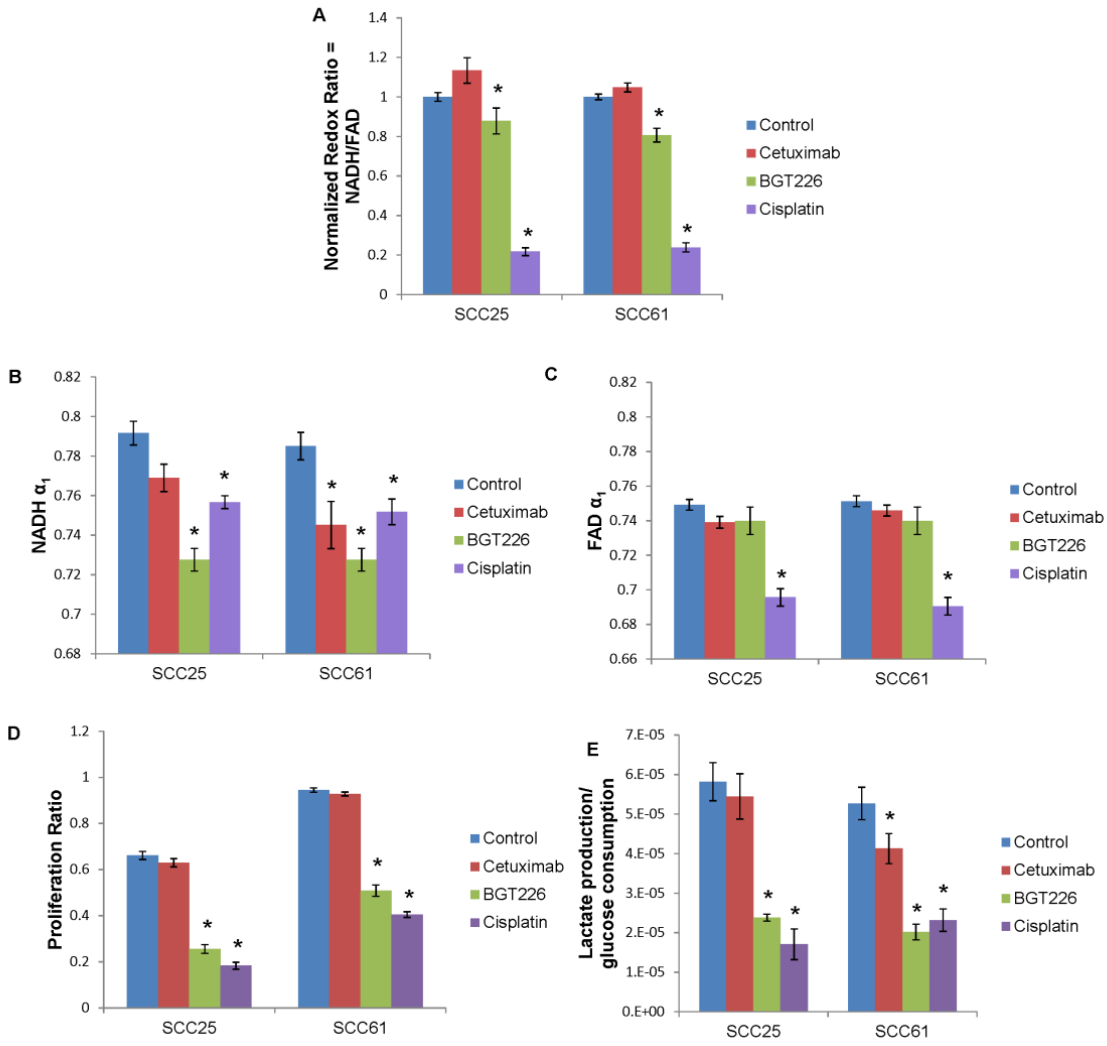

Figure 3.5. Metabolic endpoints measure response in SCC25 and SCC61 after treatment. (a) SCC25 and SCC61 cells were treated with cetuximab, BGT226, or cisplatin for 24 hours. The optical redox ratio is defined as the fluorescence intensity of NADH divided by that of FAD and is normalized by the redox ratio from control cells per day. Treatment with cetuximab does not affect the normalized redox ratio. Treatment with BGT226 or cisplatin decrease the normalized redox ratio. α_1 represents the contribution of the short fluorescence lifetime (free conformation for NADH and protein-bound conformation for FAD) ($\alpha_1+\alpha_2=1$). (b) NADH α_1 decreases after treatment with BGT226 and cisplatin in SCC25 cells and after treatment with cetuximab,

BGT226, and cisplatin in SCC61 cells. (c) FAD α_1 decreases after treatment with cisplatin in SCC25 and SCC61 cells. (d) Cells were treated for 24 hours and proliferating cells were labeled with BrdU. The ratio of proliferating cells was calculated by dividing the number of BrdU-labeled cells by the total number of cells per image. Treatment with cetuximab does not affect proliferation. Treatment with BGT226 or cisplatin treatment decrease proliferation. (e) The ratio of lactate production/glucose consumption reflects rates of glycolysis, which decreases after treatment with BGT226 and cisplatin in SCC25 cells and after treatment with cetuximab, BGT226, and cisplatin in SCC61 cells. * $p<0.05$ rank sum test, compared with control; mean ± SEM.

For SCC25, the free and protein-bound lifetimes of NADH and FAD (τ_1 and τ_2, respectively) show no significant change with any treatment (Table 3.1a). The NADH mean lifetime (τ_m) shows no change for any treatment, and the FAD mean lifetime increases with cisplatin treatment ($p<0.05$). For SCC61, free and protein-bound NADH lifetimes show no significant change with cetuximab and BGT226 treatment and increase with cisplatin treatment ($p<0.05$, Table 3.1b). For SCC61, the protein-bound FAD lifetime (τ_1) shows no change with any treatment, and the free FAD lifetime (τ_2) increases with cisplatin treatment ($p<0.05$). The NADH mean lifetime (τ_m) increases with BGT226 and cisplatin treatment ($p<0.05$), and the FAD mean lifetime increases with cisplatin treatment ($p<0.05$). NADH and FAD α_1 are also listed in Table 3.1. These data suggest that NADH α_1 is more sensitive to shifts due to treatment than τ_1, τ_2, or τ_m, and FAD α_1 is more sensitive to shifts due to treatment than τ_1 or τ_2. The NADH and FAD lifetime values for the OKF6 cells are included in Table 3.1c.

Table 3.1. The short and long fluorescence lifetime components (τ_1 and τ_2, respectively), mean lifetime (τ_m), and contribution of the short lifetime component (α_1) of NADH and FAD in SCC25 (a) and SCC61 (b) after treatment with cetuximab, BGT226, or cisplatin, as well as in OKF6 (c)

(a)	**SCC25**				
		Control	**Cetuximab**	**BGT226**	**Cisplatin**
NADH	τ_1 (ps)	528 ± 29	526 ± 34	468 ± 27	569 ± 37
	τ_2 (ps)	2899 ± 53	2889 ± 56	2726 ± 43	2955 ± 62
	τ_m (ps)	1019 ± 37	1068 ± 39	1083 ± 36	1130 ± 46
	α_1	0.792 ± 0.006	0.769 ± 0.007	0.728 ± 0.006 *	0.757 ± 0.003 *
FAD	τ_1 (ps)	426 ± 24	396 ± 20	372 ± 19	378 ± 18
	τ_2 (ps)	2667 ± 33	2624 ± 29	2633 ± 24	2630 ± 20
	τ_m (ps)	983 ± 30	913 ± 28	959 ± 33	1059 ± 29 *
	α_1	0.749 ± 0.003	0.746 ± 0.003	0.74 ± 0.008	0.696 ± 0.005 *
(b)	**SCC61**				
		Control	**Cetuximab**	**BGT226**	**Cisplatin**
NADH	τ_1 (ps)	480 ± 26	486 ± 40	460 ± 19	796 ± 54 *
	τ_2 (ps)	2760 ± 43	2763 ± 62	2673 ± 34	3335 ± 60 *
	τ_m (ps)	968 ± 28	1064 ± 50	1083 ± 36 *	1398 ± 50 *
	α_1	0.785 ± 0.007	0.745 ± 0.012 *	0.728 ± 0.006 *	0.752 ± 0.007 *
FAD	τ_1 (ps)	432 ± 25	363 ± 12	381 ± 20	450 ± 23
	τ_2 (ps)	2654 ± 35	2546 ± 15	2667 ± 28	2713 ± 25 *
	τ_m (ps)	978 ± 31	913 ± 17	959 ± 33	1142 ± 30 *
	α_1	0.751 ± 0.003	0.746 ± 0.003	0.74 ± 0.008	0.691 ± 0.005 *
(c)	**OKF6**				
		Control			
NADH	τ_1 (ps)	551 ± 38			
	τ_2 (ps)	3035 ± 61			
	τ_m (ps)	1209 ± 42			
	α_1	0.731 ± 0.0039			
FAD	τ_1 (ps)	455 ± 25			
	τ_2 (ps)	2706 ± 35			
	τ_m (ps)	1037 ± 33			
	α_1	0.737 ± 0.0043			

* $p<0.05$ rank sum test, compared with control; mean ± SEM.

3.5 Discussion

Optimized treatment regimens have potential to improve quality of life for HNSCC patients. The goal of this study is to characterize optical metabolic imaging for early assessment of treatment efficacy. The HNSCC cell lines SCC25 and SCC61 were treated with targeted therapies (cetuximab and BGT226) and chemotherapy (cisplatin) for 24 hours, and the optical redox ratio and fluorescence lifetimes of NADH and FAD were quantified. These molecular-level measurements that reflect cellular metabolism could resolve anti-cancer treatment effects sooner than current imaging modalities, including CT, MRI, and PET. Early measurement of treatment efficacy could accelerate drug screening and identify optimal treatment regimens for individual patients, thereby improving patient outcomes.

Isolation of NADH and FAD fluorescence emission was verified using cyanide perturbation (Figure 3.1). These shifts in the redox ratio and NADH and FAD lifetimes match published results for the MCF10A nonmalignant cell line from the breast [52][70][73][53]. However, these results have been previously unreported in cells from the oral cavity. Optical metabolic imaging distinguishes the malignant SCC25 and SCC61 cell lines from the nonmalignant OKF6 cell line (Figure 3.2). The increased redox ratio in HNSCC cells reflects increased reliance on glycolysis compared with oxidative phosphorylation, as expected in cancer cells (Warburg effect) [7]. This result agrees with previous findings that the redox ratio reports changes with malignancy [74]. The altered NADH and FAD fluorescence lifetimes reflect distinct signaling pathways in the HNSCC cells compared with nonmalignant cells. HNSCC cells exhibit modified intrinsic metabolic signaling that changes NADH binding sites [75], and the fluorescence lifetimes have been shown to change when NADH or FAD are bound to

different enzymes [45]. Previous studies have also shown that fluorescence lifetime imaging distinguishes normal from precancer in the DMBA-treated hamster cheek pouch model [32][33].

Changes in the redox ratio across treatment groups are consistent with proliferation rates after treatment. The redox ratio is a global measure of cellular metabolism, which drives proliferation. The redox ratio and proliferation ratio are unaffected by cetuximab treatment and show statistical differences with BGT226 and cisplatin treatment (Figure 3.5). The lack of effect from cetuximab treatment could be attributed to *in vitro* application as a single agent. In addition to inhibiting EGFR as a means of exerting effects, *in vivo* it has been shown that cetuximab initiates antibody-dependent cell-mediated cytotoxicity (ADCC) by binding to EGFR and recruiting natural killer cells and macrophages to digest the targeted cell [76]. However, immune cells are not present in these cell culture studies. *In vivo*, cetuximab treatment would be expected to have a greater impact on the optical redox ratio due to increased cell death through ADCC. This expectation is supported by our previous study, which showed more dramatic changes in redox ratio *in vivo* versus *in vitro* after treatment with the antibody trastuzumab [52]. Additionally, cetuximab is maximally effective in combination with radiotherapy and chemotherapy because it inhibits DNA repair mechanisms [18]. Conversely, BGT226 and cisplatin actively cause autophagy and cell death, respectively, in cell culture [61][77]. No previous literature has reported the effects of cetuximab or BGT226 on the optical redox ratio. Cisplatin has shown changes in the optical redox ratio in primary human foreskin keratinocytes [78].

The contribution from free NADH (NADH α_1) shows shifts in protein-binding of NADH with BGT226 and cisplatin treatment in SCC25 and SCC61 cells as well as with cetuximab treatment in SCC61 cells (Figure 3.5b). The ratio of lactate production divided by glucose

consumption reflects amounts of terminal glycolysis compared with total glucose metabolism. In glycolysis, glucose is consumed and pyruvate is produced. Pyruvate is either fermented into lactate as a terminal stage of glycolysis or converted to acetyl-coA as fuel for the citric acid cycle. Cetuximab treatment does not affect glycolysis rates in SCC25, but decreases glycolysis in SCC61. The decrease in glycolysis and NADH α_1 in SCC61 cells indicates shifts in metabolic pathways in response to treatment. However, proliferation is not affected by cetuximab in SCC61, indicating compensation by effectors downstream of EGFR. Cetuximab has been shown to not affect short-term cell growth in SCC25, which could explain the lack of statistical significance in the NADH α_1 and glycolytic index [79]. BGT226 and cisplatin treatments decrease glycolysis in SCC25 and SCC61. The effect of cetuximab or BGT226 on SCC61 cells has not been cited in previous literature, and the effect of BGT226 on glycolysis has not been reported in any model. The measurement of glycolysis rates calculated by lactate production/glucose consumption is correlated with NADH α_1 (0.81 Pearson's correlation coefficient, $p<0.05$). No other measurements produced a statistically significant correlation coefficient with lactate production/glucose consumption or proliferation. Cisplatin treatment produces outliers that impacted the correlations, particularly between lactate production/glucose consumption and the redox ratio. Previous studies have shown a correlation between glucose uptake/lactate production and the optical redox ratio in breast cancer cells [52]. However, this correlation was determined for basal metabolic rates in cells without treatment, and cells from a different organ site could rely on different metabolic mechanisms. Additionally, the control SCC61 cells show a higher proliferation ratio than SCC25 ($p<0.05$) (Figure 3.5d), but no statistical difference in redox ratio (Figure 3.2a). This is in contrast to the similar lactate production/glucose consumption between the control SCC25 and SCC61. Although the trends in

NADH α_1 and redox ratio agree with the gold standards, they are not surrogate measurements of proliferation or the amount of glycolysis compared with total glucose metabolism. For example, alternative metabolic pathways such as beta oxidation of fatty acids, the pentose phosphate pathway, and glutaminolysis are all captured differently by these gold standard measurements and our optical measurements [50][80]. The contribution from protein-bound FAD (FAD α_1) is unaffected by cetuximab and BGT226 treatments and decreases with cisplatin treatment (Figure 3.5c).

Early measures of treatment response could enable effective intervention while reducing the acute toxicities and serious morbidities from ineffective therapies. Molecular-level measurements that reflect cellular metabolism are well-suited to measure effects from cancer treatments that target metabolic pathways. The optical redox ratio and fluorescence lifetimes of NADH and FAD resolve a response after 24 hours of treatment with targeted therapies and chemotherapies in HNSCC cells. These results indicate that optical metabolic imaging shows promise to identify effective drug candidates during drug development. Additionally, applying optical metabolic imaging to measure treatment response early has potential to impact quality of life for HNSCC patients.

3.6 Acknowledgements

The proliferation experiment and glucose and lactate assays used equipment in Dr. Hak-Joon Sung's lab at Vanderbilt University. The western blotting analysis used materials in Dr. Robert Coffey's lab at Vanderbilt University. Thanks to Dr. Brent Rexer for helpful input and guidance as well as Spencer Crowder for help with the proliferation measurements.

CHAPTER 4

IN VIVO AUTOFLUORESCENCE IMAGING OF TUMOR HETEROGENEITY IN RESPONSE TO TREATMENT

Shah AT, Diggins KE, Walsh AJ, Irish JM, Skala MC, "*In Vivo* Autofluorescence Imaging of Tumor Heterogeneity in Response to Treatment." Neoplasia, 2015; 17(12):862-870

4.1 Abstract

Subpopulations of cells that escape anti-cancer treatment can cause relapse in cancer patients. Therefore, measurements of cellular-level tumor heterogeneity could enable improved anti-cancer treatment regimens. Cancer exhibits altered cellular metabolism, which affects the autofluorescence of metabolic cofactors NAD(P)H and FAD. The optical redox ratio (fluorescence intensity of NAD(P)H divided by FAD) reflects global cellular metabolism. The fluorescence lifetime (amount of time a fluorophore is in the excited state) is sensitive to microenvironment, particularly protein-binding. High-resolution imaging of the optical redox ratio and fluorescence lifetimes of NAD(P)H and FAD (optical metabolic imaging) enables single-cell analyses. In this study, mice with FaDu tumors were treated with the antibody therapy cetuximab or the chemotherapy cisplatin and imaged *in vivo* two days after treatment. Results indicate that fluorescence lifetimes of NAD(P)H and FAD are sensitive to early response (two days post-treatment, $p<0.05$), compared with decreases in tumor volume (nine days post-treatment, $p<0.05$). Frequency histogram analysis of individual optical metabolic imaging parameters identifies subpopulations of cells, and a new heterogeneity index enables quantitative comparisons of cellular heterogeneity across treatment groups for individual variables.

Additionally, a dimensionality reduction technique (viSNE) enables holistic visualization of multivariate optical measures of cellular heterogeneity. These analyses indicate increased heterogeneity in the cetuximab and cisplatin treatment groups compared with the control group. Overall, the combination of optical metabolic imaging and cellular-level analyses provide novel, quantitative insights into tumor heterogeneity.

4.2 Introduction

Cancer treatments often include chemotherapy, targeted therapy, and/or radiation therapy. Most cancer patients respond to treatment initially, exhibiting decreased tumor volume, and later relapse, exhibiting increased tumor volume. Chemotherapy and targeted treatments can eliminate the majority of cells in a tumor while subpopulations of cells can escape treatment [54][55]. These subpopulations of cells may be responsible for innate or acquired resistance, which can enable treatment failure, disease progression, and diminished patient outcomes.

Standard chemotherapies and radiation treatments are administered based on average response rates for a particular type and stage of cancer. Current methods for determining targeted treatment strategies rely on identifying the dominant subpopulation of cells, usually based on surface marker expression, and administering drugs that inhibit the overexpressed targets to decrease proliferation or increase death of the cells expressing those targets [57]. Resistant subpopulations existing within a tumor could escape the treatment, allowing relapse after therapy. Therefore, tumor heterogeneity poses a difficult challenge for optimizing treatment outcomes in cancer patients.

Tumor heterogeneity can be characterized as genetic, phenotypic, or functional [81][82]. Genetic measures focus on analysis of genes known to promote tumor progression. Phenotypic

characterization is usually established from histology to visualize cell morphology and from immunohistochemistry to measure expression of cell surface receptors, growth factors, and hormone receptors. However, these measures may not directly relate to cellular function [81]. Whereas genetic and phenotypic biomarkers provide static measurements, functional measures characterize dynamic tumor behavior or response to stimuli and therefore may be more attractive. Functional measures include cellular metabolism, oxygen consumption, and blood perfusion. In particular, cellular metabolism, which is altered in cancer [7], has been shown to be a good indicator of drug response and therefore may be a promising marker for tumor heterogeneity [62].

Numerous metabolic pathways involve the autofluorescent co-enzymes NAD(P)H (an electron donor) and FAD (an electron acceptor). The optical redox ratio is defined as the fluorescence intensity of NAD(P)H divided by that of FAD, and is an established method for monitoring relative amounts of electron donor and acceptor in a cell [46][51][52]. As a complementary measure, the fluorescence lifetime reports the amount of time a fluorophore is in the excited state before relaxing to the ground the state. Fluorescence lifetime is sensitive to conformational changes in enzyme structure that are caused by the microenvironment, particularly protein-binding [39]. The fluorescence lifetime of NAD(P)H has two distinct components, due to vastly different lifetimes when NAD(P)H is in the free and protein-bound states [45]. Similarly, FAD has two lifetimes due to its free and protein-bound states [83]. The short lifetimes of NAD(P)H (free state) and FAD (protein-bound state) are due to quenching by the adenine moiety of the molecule [39]. The redox ratio and fluorescence lifetime provide independent measurements of cellular metabolism [52], and can be performed using two-photon fluorescence microscopy, which enables cellular-level imaging and deeper penetration in tissue

than single-photon (e.g. confocal) microscopy [84]. This approach exploits the endogenous contrast of NAD(P)H and FAD autofluorescence to acquire quantitative measurements of cellular metabolism that can be used to characterize cellular heterogeneity.

There are few analysis approaches that are appropriate for quantifying cellular heterogeneity. The Shannon diversity index is a metric used in ecology literature that incorporates the number and relative proportions of species in a community [85], and it has also been applied to tumor heterogeneity [86][87][88]. However, the degree of separation between subpopulations is also an important consideration in tumor heterogeneity [89], which is not incorporated into the Shannon diversity index. A metric incorporating the number of cellular subpopulations, relative contributions of each subpopulation, and relative differences in subpopulations to quantify tumor heterogeneity could provide insight into optimal treatment strategies for cancer patients. This type of metric could be applied to each optical metabolic imaging parameter, including the redox ratio and fluorescence lifetime components of NAD(P)H and FAD.

Since optical metabolic imaging acquires multi-dimensional data sets of parameters, which can be difficult to interpret holistically, dimensionality reduction techniques can be applied as a complementary method to facilitate interpretation of these types of data sets. Traditional methods apply a linear transformation of the data, like principal component analysis (PCA) [90]. However, an alternative method that preserves nonlinear relationships at a single-cell level may be advantageous, like the viSNE technique [91]. ViSNE is a dimensionality reduction tool that uses t-distributed stochastic neighbor embedding (t-SNE) to plot high-dimensional single-cell data on a two-dimensional axis for visualization of cellular heterogeneity, and is well-suited for single-cell data acquired in optical metabolic imaging.

ViSNE is also attractive for identifying cell sub-populations because it preserves the relative distances between cells that are present in multi-dimensional space when projecting them into two-dimensional space, thereby maintaining relationships between individual cells in the reduced data set and identifying relationships that would not be apparent by manual analysis alone.

This study quantifies the optical redox ratio and fluorescence lifetimes of NAD(P)H and FAD in a xenograft model of head and neck cancer two days after treatment with the antibody therapy cetuximab or the chemotherapy cisplatin. Additionally, these *in vivo* high-resolution images enabled analysis of cellular metabolic heterogeneity in response to treatment at an early time point using endogenous contrast. An index to quantify heterogeneity was developed, validated on samples containing cultures of one cell line or co-cultures containing two cell lines, and applied *in vivo* to each individual optical metabolic imaging variable. Additionally, a dimensionality reduction technique (viSNE) was applied to enable holistic visualization of heterogeneity across all optical metabolic imaging variables combined. Immunohistochemistry stains for cell proliferation and cell death validated treatment efficacy, and tumor growth curves measured gold standard treatment response. Results indicate that *in vivo* optical metabolic imaging, combined with a quantitative metric of heterogeneity or a dimensionality reduction visualization of heterogeneity, has potential to resolve treatment-induced cellular-level heterogeneities in tumors. Ultimately, characterization of cellular heterogeneity could enable optimized treatment regimens and improved patient outcomes.

4.3 Materials and Methods

In Vivo Imaging and Tumor Growth Curves

FaDu cells were grown in DMEM media supplemented with 10% fetal bovine serum (FBS) and 0.4µg/mL hydrocortisone. Approximately 10^7 FaDu cells were injected into the flanks of 7 week old male nude mice and tumors were grown to approximately $100mm^3$. Mice in treated groups received treatment of cetuximab (33mg/kg) [92][93] or cisplatin (6mg/kg) [94] via intraperitoneal injection. To measure tumor growth curves, mice were treated three times a week for two weeks (6 tumors per group). Tumor volumes were measured daily and calculated by $(l*w^2)/2$, where l represents the tumor length in mm and w represents the tumor width in mm. Tumor volumes were normalized to the size on day 1. On day 13, tumors were excised and fixed for immunohistochemistry, and mice were euthanized. A separate cohort of mice were used for *in vivo* imaging studies, with only one dose per treatment group on day zero (6 tumors for control group, 5 tumors for cetuximab and cisplatin groups). Two days after treatment, each mouse was anesthetized and the skin covering the tumor was removed. A coverslip was placed over the exposed tumor, and the mouse was placed on the microscope to acquire *in vivo* images (3-7 images per tumor).

Imaging Instrumentation

Mice were imaged on a custom-built (Bruker) inverted two-photon fluorescence microscope (Ti-E Nikon) using a 40x oil immersion objective (1.3 NA). A titanium:sapphire laser (Chameleon, Coherent Inc.) was used for excitation, and a GaAsP photomultiplier tube (H7422P-40, Hamamatsu) was used for fluorescence collection. To measure NAD(P)H autofluorescence, an excitation wavelength of 750nm and an emission filter of 400-480nm was used. To measure

FAD autofluorescence, an excitation wavelength of 890nm and an emission filter of 500-600nm was used. Time correlated single photon counting electronics (SPC-150, Becker and Hickl) were used to acquire fluorescence lifetime images over 60 seconds, and photon count rates (~2-3 x 10^5) were monitored during this time to ensure the absence of photobleaching. A pixel dwell time of 4.8 μs was used to acquire 256x256 pixel images. First, an NAD(P)H lifetime image was acquired, and then an FAD lifetime image was acquired from the same field of view. Sequential fields of view were separated by at least one field of view. A Fluoresbrite YG microsphere (Polysciences Inc.) was imaged as a daily standard with a fluorescence lifetime of 2.11±0.05 ns (n=7), consistent with previous studies [32][95]. Instantaneous scattering from second harmonic generation of urea crystals excited at 900nm was measured to calculate the full width at half maximum of the instrument response function (244ps).

Image Analysis

Fluorescence lifetime images were analyzed as described previously [96]. Briefly, the fluorescence lifetime decay curves were fit to a two-component exponential function, $F(t) = \alpha_1 e^{-t/\tau 1} + \alpha_2 e^{-t/\tau 2} + c$, where F(t) represents the fluorescence intensity over time, α_1 and α_2 represent the contribution from the short and long lifetime components respectively ($\alpha_1+\alpha_2=1$), and τ_1 and τ_2 represents the fluorescence lifetime of the short and long lifetime components respectively (SPCImage, Becker and Hickl). A two-component fit has been shown to be appropriate for describing freely diffusing versus protein-bound conformations of NAD(P)H and FAD [32]. For NAD(P)H, the short lifetime represents free NAD(P)H, and for FAD the short lifetime represents protein-bound FAD [39]. The weighted mean lifetime, τ_m, was calculated by $\tau_m=\alpha_1\tau_1+\alpha_2\tau_2$. A fluorescence intensity image was generated by integrating the fluorescence lifetime decay over

time for each pixel in the lifetime image. The optical redox ratio was calculated by dividing the NAD(P)H fluorescence intensity by the FAD fluorescence intensity for each pixel to create a redox ratio image for each field of view. NAD(P)H and FAD fluorescence specific to cellular metabolism is localized in the cytoplasm and mitochondria. Therefore, the redox ratio and fluorescence lifetime images were thresholded to remove nuclear fluorescence, and the average redox ratio and fluorescence lifetime decay parameters for each remaining cell cytoplasm was computed. The optical redox ratio and NAD(P)H and FAD fluorescence lifetime images were quantified for each cytoplasm in each cell using a customized CellProfiler routine as described previously [97].

Heterogeneity Index and Validation

For subpopulation analysis, frequency histograms were plotted for the optical redox ratio, NAD(P)H τ_m, and FAD τ_m, as described and validated in [98]. The histograms were fit to one-, two-, or three-component Gaussian curves, and the lowest Akaike Information Criterion indicated optimal fitting [8]. Each Gaussian curve represents a subpopulation of cells, and the sum of the Gaussian curves was plotted for visualization. To quantify heterogeneity, a heterogeneity index was defined as $H = -\sum d_i p_i \ln p_i$, where i represents each subpopulation, d represents the distance between the median of the subpopulation and the median of all data within a group, and p represents the proportion of the subpopulation. Validation of the heterogeneity index was performed on co-cultures of MDA-MB-231 and SKBr3 breast cancer cell lines plated at ratios of 0:100, 50:50, and 100:0.

ViSNE

The viSNE dimensionality reduction tool was used to visualize cellular heterogeneity by incorporating all seven optical metabolic imaging parameters: the optical redox ratio, NAD(P)H α_1, NAD(P)H τ_1, NAD(P)H τ_2, FAD α_2, FAD τ_1, and FAD τ_2. The data from each parameter was transformed to a common scale of 0 to 100%, where 100% represented the highest value for that parameter across all treatment groups. Data were analyzed in Cytobank (www.cytobank.org) to create a viSNE map [91][99][100]. ViSNE performs t-distributed stochastic neighbor embedding (t-SNE) to minimize the differences between high-dimensional space and low-dimensional space, and produces a two-dimensional plot in arbitrary units. Briefly, a pairwise distance matrix is calculated in high dimensional space, which is transformed to a similarity matrix using a varying Gaussian kernel. The points are randomly mapped in low-dimensional space and iteratively rearranged to minimize the divergence between high-dimensional and low-dimensional similarity matrices.

Statistical Analyses

Bar graphs are shown as mean ± standard error. Kruskal-Wallis and two-way rank sum tests determined statistical significance with an α of 0.05.

4.4 Results

Tumor growth curves measure tumor volume changes in FaDu xenografts after treatment (Figure 4.1a). Compared with control, cetuximab and cisplatin treatments cause tumor volume decreases starting six and nine days, respectively after treatment onset ($p<0.05$). Immunohistochemistry was performed on excised tumor tissue at the end of the study to quantify

markers of treatment efficacy (Figure 4.1). Ki-67 staining shows decreased proliferation with each treatment group ($p<0.05$; Figure 4.1b). Cleaved caspase 3 shows increased cell death with cisplatin treatment ($p<0.05$; Figure 4.1c). These gold standard measurements verify drug efficacy in the xenografts.

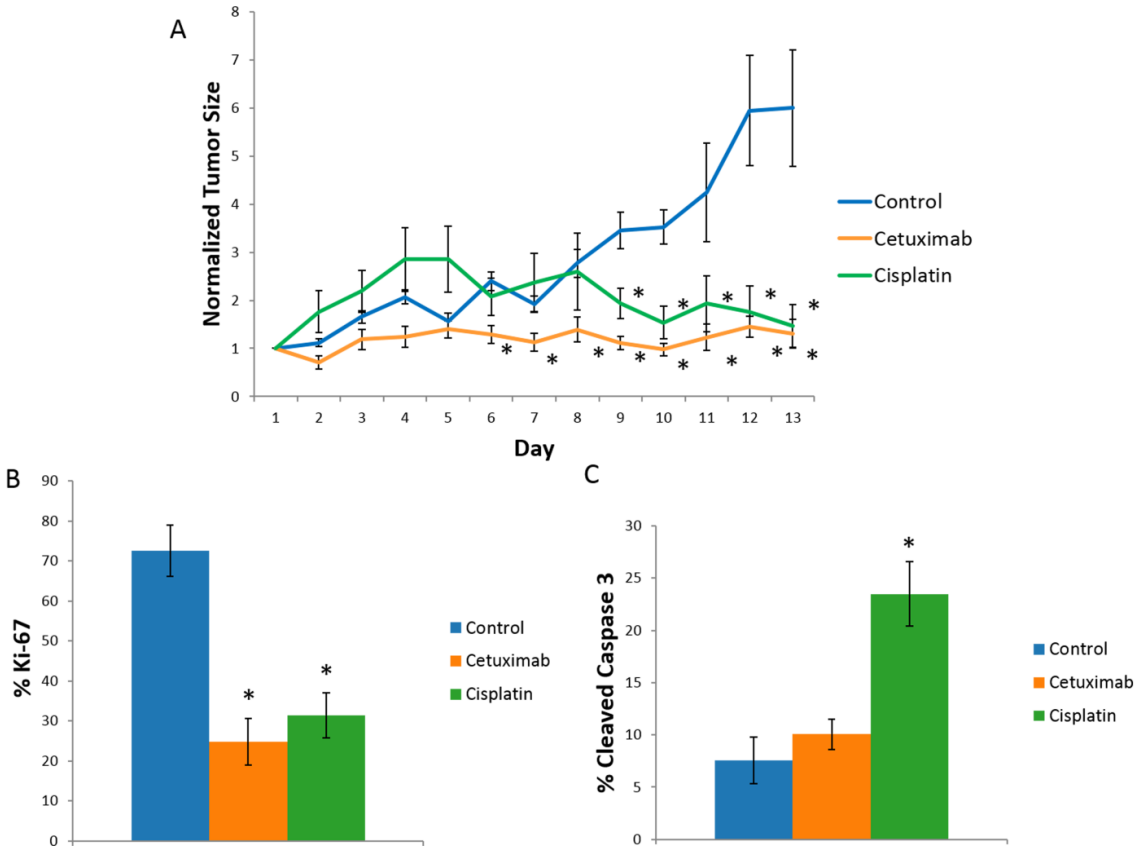

Figure 4.1. *In vivo* validation of treatment effects. (A) Tumor growth curves show a decrease (*$p<0.05$, compared with control) in tumor volume in cetuximab treated xenografts after 6 days of treatment and in cisplatin treated xenografts after 9 days of treatment. Xenografts were excised and stained for ki-67 (proliferation) and cleaved caspase 3 (cell death) on day 13. (B) Xenografts from cetuximab and cisplatin treated mice exhibited decreased proliferation. (C) Xenografts from cisplatin treated mice exhibited increased cell death. *$p<0.05$ compared with control, rank sum test

Representative *in vivo* images demonstrate cellular-level resolution of NAD(P)H and FAD autofluorescence imaging and enables visualization of qualitative differences in the optical metabolic imaging parameters two days after treatment (Figure 4.2). Images were quantified to calculate the average optical redox ratio, NAD(P)H fluorescence lifetime, and FAD fluorescence lifetime per-cell (Figure 4.3). The redox ratio shows no change with cetuximab treatment and decreases with cisplatin treatment ($p<0.05$). The NAD(P)H fluorescence lifetime decreases with cetuximab and cisplatin treatments ($p<0.05$). The FAD fluorescence lifetime decreases with cetuximab and cisplatin treatments ($p<0.05$). The shifts in fluorescence lifetime reflect shifts in microenvironment, particularly NAD(P)H and FAD protein-binding. NAD(P)H τ_1, NAD(P)H τ_2, FAD τ_1, and FAD τ_2 decrease with cetuximab and cisplatin treatments (Figure A.1, $p<0.05$). The relative amounts of free NAD(P)H and FAD increase and decrease, respectively, with cetuximab and cisplatin treatments (Figure A.1, $p<0.05$).

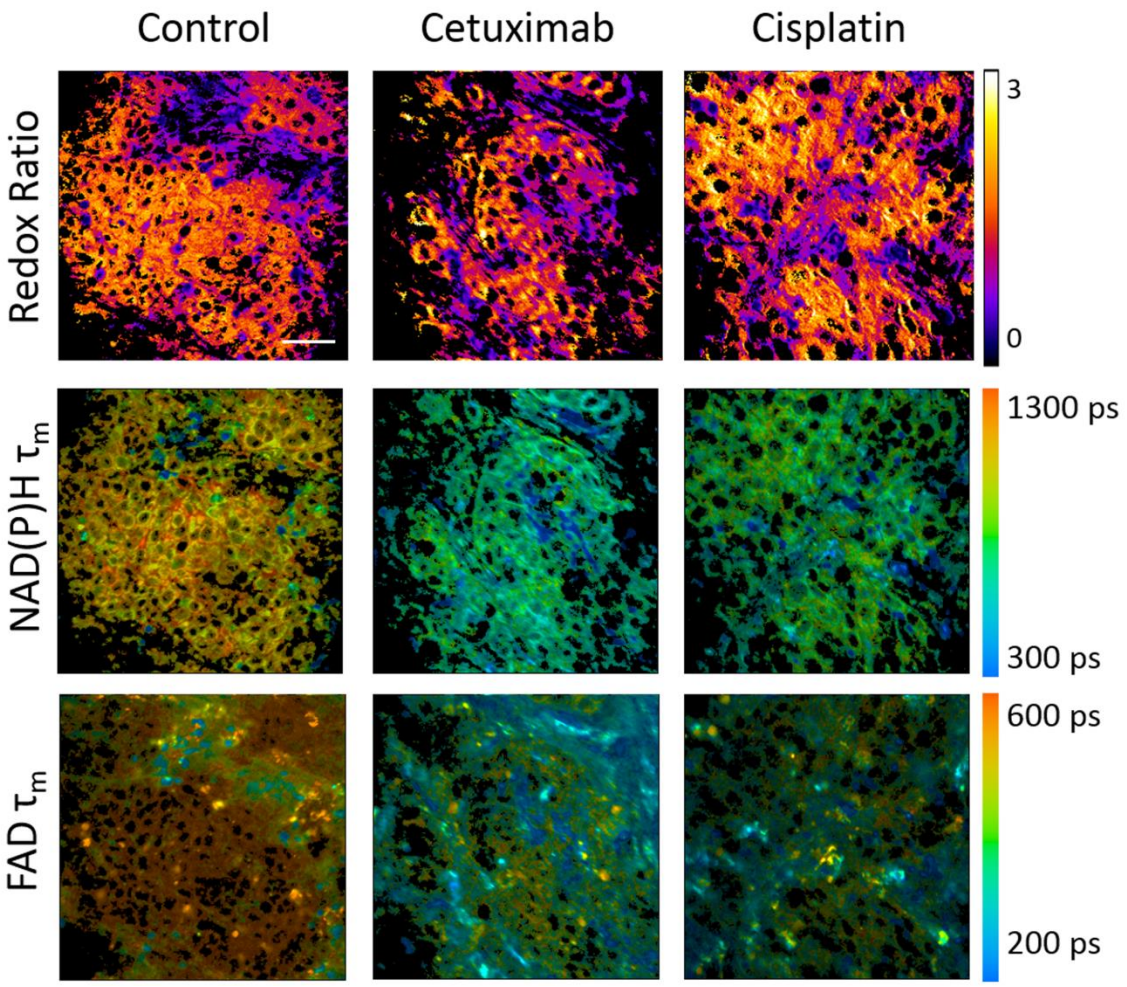

Figure 4.2. *In vivo* images of FaDu xenografts 2 days after treatment with cetuximab or cisplatin. NAD(P)H and FAD autofluorescence images were acquired from the same fields of view, and the redox ratio (top row), NAD(P)H fluorescence lifetime (middle row), and FAD fluorescence lifetime (bottom row) were calculated. Scale bar = 50um.

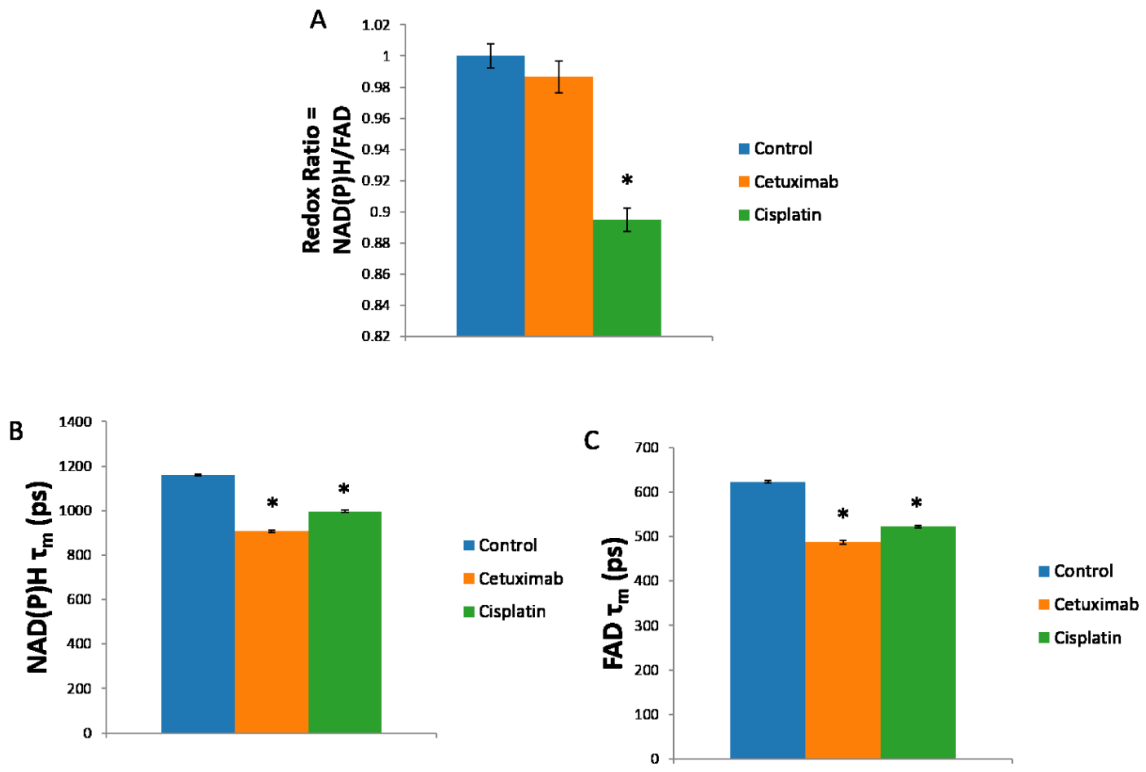

Figure 4.3. The optical redox ratio, NAD(P)H fluorescence lifetime, and FAD fluorescence lifetime quantified from *in vivo* NAD(P)H and FAD autofluorescence images 2 days after treatment. (A) The redox ratio decreases with cisplatin treatment. (B, C) The NAD(P)H and FAD fluorescence lifetimes decrease after cetuximab and cisplatin treatment. The shifts in NAD(P)H and FAD fluorescence lifetime measured 2 days after treatment are consistent with response measure by tumor growth curves and immunohistochemistry after 13 days of treatment. *$p<0.05$, compared with control

Single-cell images were represented as histograms of number of cells versus optical metabolic imaging parameters, and Gaussian fits were used to identify distinct cell sub-populations for each treatment group. Histograms plotting the sum of Gaussian fits for the redox ratio, NAD(P)H fluorescence lifetime, and FAD fluorescence lifetime highlight cellular

heterogeneity across treatment groups for each optical parameter (Figure 4.4a-c and Figure A.2). For the redox ratio, histograms of the treatment groups have some overlap with control. This trend is consistent with the NAD(P)H and FAD fluorescence lifetimes. The degree of overlap for the subpopulations of cells from each treatment group compared with control could reflect the degree of resistant cells compared with responsive cells.

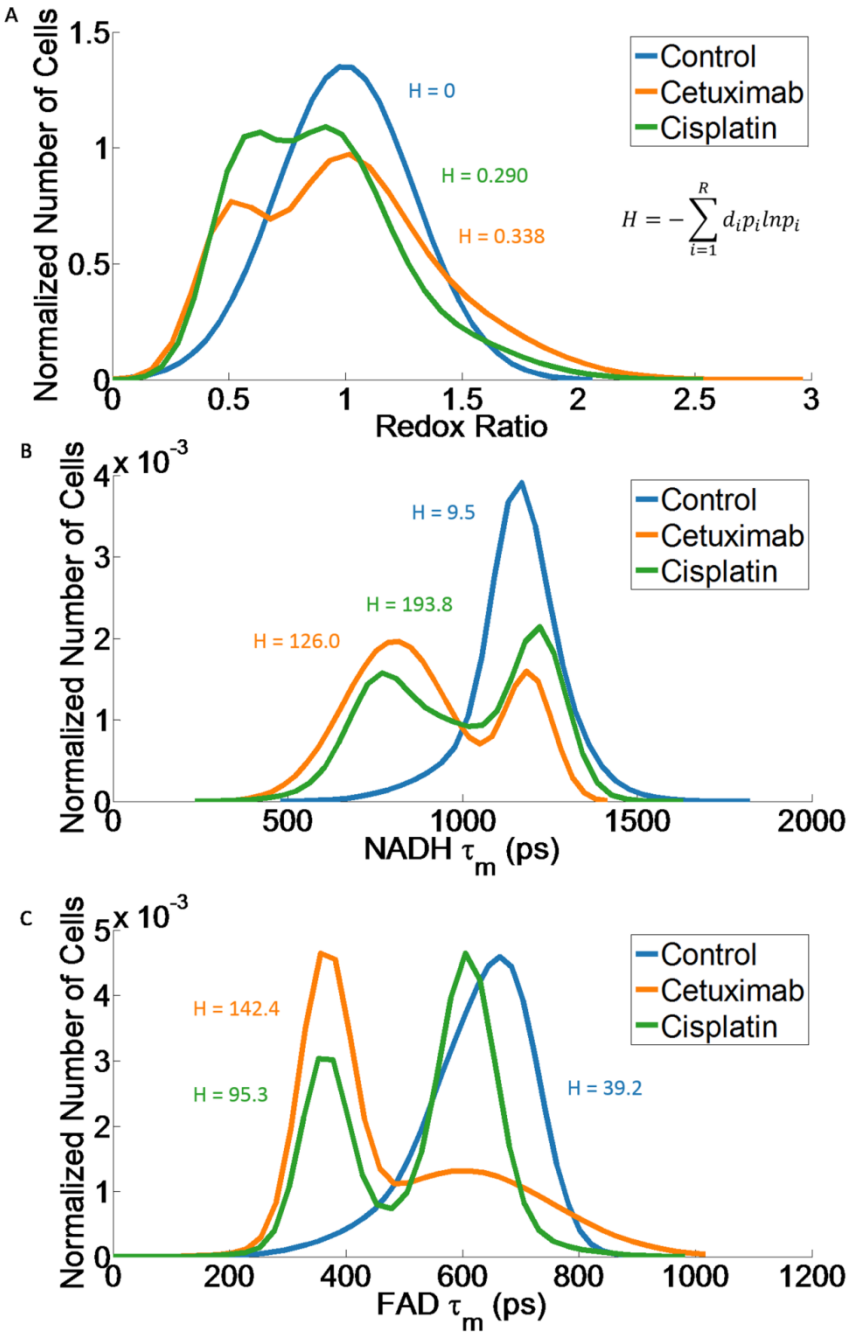

Figure 4.4. *In vivo* heterogeneity analysis after treatment. To quantify the level of cellular metabolic heterogeneity within a treatment group, each group is fit to one, two, or three Gaussian curves based on the Akaike Information Criterion. Each Gaussian curve represents one subpopulation, and the sum of the Gaussian curves is plotted for visualization. The heterogeneity index, H, is a weighted sum over each subpopulation within a treatment group that incorporates

d, the distance between the median of the subpopulation and the median of all data in the treatment group, and p, the weight of the subpopulation. This parameter is the Shannon diversity index modified to incorporate the relative location of each subpopulation. Increased heterogeneity index indicates increased number of subpopulations, increased equality in the weights of each subpopulation within a treatment group, and increased separation in the locations of the subpopulations. (A) The heterogeneity index for the redox ratio is lowest for the control group followed by the cisplatin and cetuximab treatment groups. (B) The heterogeneity index for the NAD(P)H fluorescence lifetime is lowest for the control group followed by the cetuximab and cisplatin treatment groups. (C) The heterogeneity index for the FAD fluorescence lifetime is lowest for the control group followed by the cisplatin and cetuximab treatment groups.

In order to compare cellular-level heterogeneity across treatment groups, a quantitative metric called the "heterogeneity index" was developed, validated *in vitro*, and then applied to *in vivo* histograms. The heterogeneity index is the Shannon diversity index weighted by a distance factor, where a larger value indicates more subpopulations, similar numbers of cells within each subpopulation, and/or more distance between subpopulations. The heterogeneity index was validated on co-cultures of MDA-MB-231 and SKBr3 breast cancer cell lines because they exhibit distinct optical redox ratios [52]. The heterogeneity index was calculated for the optical redox ratio of dishes including 100% MDA-MB-231 cells, 100% SKBr3 cells, and 50% MDA-MB-231 + 50% SKBr3 cells. The condition with two cell lines causes an increased heterogeneity index (0.285) compared with the MDA-MB-231 cell line (0.006) or the SKBr3 cell line (0.152) cultured alone (Table 4.1), indicating that the heterogeneity index behaves as expected. SKBr3 cells have been shown to exhibit intrinsic heterogeneity within the cell line based on HER2

expression, which could account for the relatively high heterogeneity index within that cell line [101]. For the *in vivo* studies, the heterogeneity index is increased for the treated groups compared with the control for the redox ratio (Figure 4.4a), NAD(P)H fluorescence lifetime (Figure 4.4b), and FAD fluorescence lifetime (Figure 4.4c). This trend in heterogeneity index is consistent for the redox ratio of FaDu cell monolayers treated with cetuximab and cisplatin *in vitro* (Figure A.4). Note that the heterogeneity index is not normalized, and therefore not comparable between variables.

Table 4.1: Validation of the heterogeneity index. The heterogeneity index is defined as $H = -\sum[d_i p_i \ln(p_i)]$, where i represents each subpopulation, d represents the distance between the median of the subpopulation and the median of all data within a group, and p represents the proportion of the subpopulation. The heterogeneity index was validated using redox ratio measurements of MDA-MB-231 and SKBr3 cell monolayer cultures plated at ratios of 0:100, 50:50, and 100:0, and exhibits an increased value for the 50:50 condition.

MDA-MB-231: SKBr3 Ratio	0:100	50:50	100:0
Heterogeneity Index	0.152	0.285	0.006

The heterogeneity index is helpful to analyze individual variables, but a dimensionality reduction technique is necessary to visualize tumor heterogeneity with respect to all optical variables combined. ViSNE reduces seven optical metabolic imaging parameters by preserving the similarities across cells and projecting these onto a two-dimensional axis (Figure 4.5). ViSNE analysis shows a distinct population of the control group, while the cetuximab and cisplatin treatment groups overlap with control and also exhibit a separate subpopulation of cells

(Figure 4.5a). This trend is consistent in FaDu cell monolayers *in vitro* (Figure A.4). ViSNE preserves similarities across cells in a nonlinear way by producing a visual two-dimensional scatter plot, but does not provide a quantitative relationship between the input parameters and the viSNE plot. Therefore, heat maps plotting the values for individual parameters over the two-dimensional viSNE axes can be helpful for understanding the contribution of each parameter to the viSNE plot (Figure 4.5b-c and Figure A.3). Gradients within a parameter that correspond with the grouping in the viSNE plot indicate that these parameters contribute significantly to the viSNE plot. In particular, gradients in NAD(P)H τ_1 and FAD τ_1 agree with grouping in the viSNE plot because points in the top group of the viSNE plot exhibit low values compared with points in the bottom group (Figure 4.5b-c).

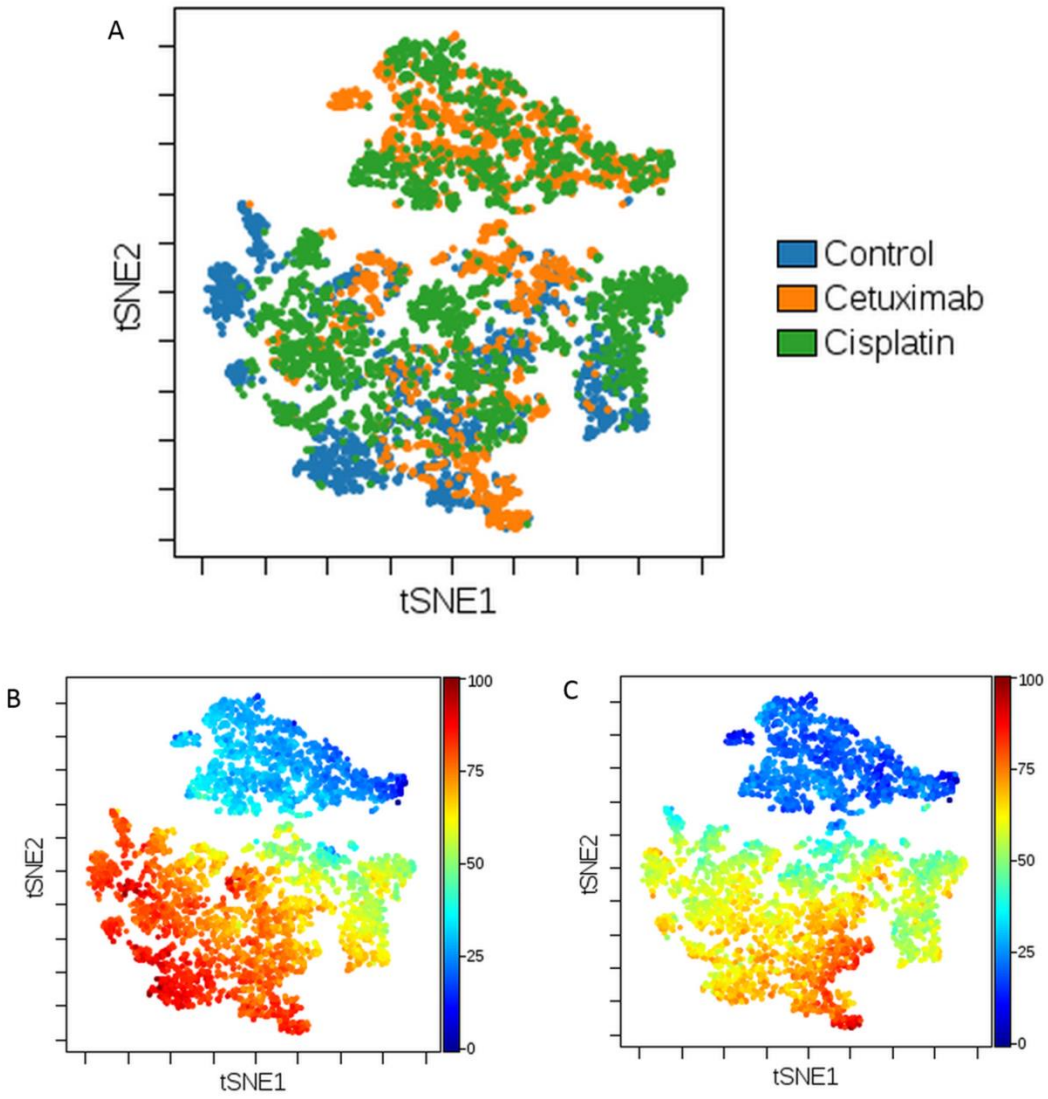

Figure 4.5. Single-cell analysis using the dimensionality-reduction technique viSNE reduces seven optical metabolic imaging parameters to two dimensions for visualization of heterogeneity across individual cells. To account for different scales between parameters, common linear transformation was applied within each parameter across all treatment groups so the transformed values range from 0 to 100. (A) ViSNE analysis shows a distinct population of cells for the control group. The cetuximab and cisplatin treatment groups overlap with the control group and also exhibit a separate subpopulation of cells. (B, C) Heat maps of the short fluorescence lifetime components for (B) NAD(P)H and (C) FAD show gradients over the 2-dimensional viSNE axes.

4.5 Discussion

Tumor heterogeneity poses a difficult challenge for improving treatment outcomes in cancer patients. The goal of this study is to apply autofluorescence imaging of the metabolic cofactors NAD(P)H and FAD to resolve anti-cancer treatment response on a cellular level, and characterize cellular heterogeneity. Mice with FaDu xenografts were treated with cetuximab or cisplatin, and 48 hours later the xenografts were imaged *in vivo* using two-photon microscopy and fluorescence lifetime imaging. Cellular-level imaging enabled per-cell analysis of the optical redox ratio and fluorescence lifetimes of NAD(P)H and FAD in response to treatment, and a heterogeneity index was devised to quantify cellular heterogeneity for each optical metabolic imaging variable. Furthermore, a dimensionality reduction technique was applied on a per-cell level to visualize heterogeneity on a two-dimensional axis based on combined information from all optical variables. Overall, the degree of heterogeneity is increased for the xenografts of mice treated with cetuximab or cisplatin compared with control. These nondestructive, quantitative methods to measure *in vivo* cellular heterogeneity could be used to develop improved treatments that account for tumor heterogeneity and target all tumor cell sub-populations for improved efficacy in cancer patients.

Tumor growth curves show that over two weeks of treatment the administration of cetuximab or cisplatin causes stable disease, exhibiting decreased tumor volume compared with control tumors that exhibit continued increase in tumor volume (Figure 4.1A). These results agree with clinical studies of patients administered cetuximab or cisplatin [102][103]. Additionally, cetuximab and cisplatin treatment cause decreased cell proliferation (Figure 4.1B), which agrees with previous *in vitro* studies [104][105]. Cisplatin treatment causes increased cell death (Figure 4.1C). Cisplatin has been shown to cause apoptosis [106], and cetuximab sensitizes

cells to chemotherapy by inhibiting DNA repair mechanisms [18]. Cetuximab has been shown to cause autophagy instead of apoptosis [104]. These immunohistochemistry measures verify *in vivo* drug efficacy.

The redox ratio of FaDu xenografts measured *in vivo* decreases 48 hours after cisplatin treatment, whereas cetuximab treatment causes no change in the redox ratio (Figure 4.3A). These results agree with *in vitro* optical redox ratio measurements in SCC25 and SCC61 head and neck cancer cell lines treated with cetuximab or cisplatin [96]. The lack of effect from cetuximab treatment could reflect its administration as a single agent, since cetuximab is maximally effective in combination with chemotherapy and radiation therapy. Additionally, cetuximab initiates antibody-dependent cell cytotoxicity (ADCC), but this process might be altered in the immunocompromised nude mice used in this study [76]. The NAD(P)H and FAD mean lifetimes decrease with cetuximab and cisplatin treatment (Figure 4.3B, C), which could reflect treatment-induced changes in preferred metabolic pathways involving NAD(P)H and FAD. These results also highlight the fact that the redox ratio and fluorescence lifetimes of NAD(P)H and FAD probe different features of cellular metabolism [52]. The redox ratio reflects relative amounts of electron donor (NAD(P)H) and acceptor (FAD), whereas the fluorescence lifetimes of NAD(P)H and FAD reflect enzyme activity, preferred protein-binding, and other microenvironmental factors (e.g. pH) of these co-factors [39]. Decreased NAD(P)H and FAD mean fluorescence lifetimes have also been measured in BT474 breast cancer xenografts treated with antibody therapy trastuzumab two days after treatment [52]. No previous literature has reported the effects of chemotherapy *in vivo* on the optical redox ratio and fluorescence lifetimes of NAD(P)H and FAD. These fluorescence lifetime changes two days after treatment agree with tumor volume

decreases in treated mice nine days after treatment onset, indicating that NAD(P)H and FAD fluorescence lifetime measurements could reflect early treatment-induced metabolic effects.

To visualize treatment-induced shifts in cellular heterogeneity, frequency histograms were plotted for the optical redox ratio and mean fluorescence lifetimes of NAD(P)H and FAD. Shifts in the histograms can be qualitatively visualized across control and treatment groups (Figure 4.4), and a metric to describe cellular heterogeneity is necessary for quantitative comparisons. However, there is no standard metric for quantifying tumor heterogeneity. We have modified the Shannon diversity index to incorporate the relative separation between subpopulations by including a coefficient of the distance between the median of each subpopulation to the median of the group. Since the scale and range of this coefficient depends on the parameter, the heterogeneity index is a relative value for each parameter. A heterogeneity index of 0 indicates one population of cells, and the index increases with increased number of subpopulations, evenness between subpopulations, and distance between subpopulations. The heterogeneity index increases for co-cultures of SKBr3 and MDA-MB-231 cells compared with either cell line alone (Table 4.1), indicating that an increased heterogeneity index reflects increased sample heterogeneity. The heterogeneity index was calculated for the redox ratio, NAD(P)H fluorescence lifetime, and FAD fluorescence lifetime (Figure 4.4), and is consistently lower for the control group compared with the cetuximab or cisplatin treatments. The higher heterogeneity index for the treatments indicates increased variability in cellular response to each treatment, and could indicate a balance between cellular response and resistance that leads to stable disease as seen in tumor growth curves (Figure 4.1A). Additionally, *in vitro* heterogeneity analysis of FaDu cell monolayers show similar response as *in vivo* results, indicating intrinsic heterogeneity in the FaDu cell response to cetuximab and cisplatin (Figure A.4). Other factors

could also contribute to *in vivo* drug response, including hypoxia, drug delivery, and glucose gradients. These factors could induce greater heterogeneity in the *in vivo* optical metabolic imaging measurements compared to *in vitro* measurements.

The heterogeneity index can be applied to individual optical metabolic imaging parameters. However, since the seven optical metabolic imaging parameters are complementary measures [52], incorporating all parameters into one heterogeneity analysis could provide additional insight for characterizing tumor heterogeneity. Dimensionality reduction techniques can preserve the similarity between cells across multiple variables, and project relative distances between cells onto a two-dimensional scatter plot. Common dimensionality reduction techniques include principal component analysis (PCA), but this method requires a linear transformation of the data [107]. The viSNE technique optimizes the separation between cells based on high-dimensional data sets without relying on a linear transformation of the data, so it can preserve non-linear relationships at single-cell resolution, identify rare subpopulations of cells, and provide a two-dimensional plot for visualization of cellular heterogeneity [91]. These advantages make viSNE an attractive tool for the analysis of optical metabolic imaging parameters. ViSNE analysis shows a distinct population of cells in the control group. In contrast, the cetuximab and cisplatin treatment groups overlap with control and also display a separate subpopulation of cells (Figure 4.5). This indicates increased heterogeneity in the treatments compared with the control, which agrees with the analysis of the heterogeneity index applied to individual optical metabolic imaging parameters (redox ratio, NAD(P)H and FAD fluorescence lifetimes). A gradient in the short lifetime components of NAD(P)H and FAD can be seen across the viSNE map (Figure 4.5B, C), which indicates that these optical parameters contribute more variability to the data set.

These results indicate that the combination of optical metabolic imaging and single-cell analyses (heterogeneity index, viSNE) are attractive for characterizing tumor heterogeneity.

Tumor heterogeneity poses a challenge for optimizing anti-cancer treatment strategies in cancer patients, and new tools are necessary to adequately quantify and interpret tumor heterogeneity *in vivo* in animal models at a cellular level. This study shows that optical metabolic imaging can resolve metabolic shifts induced by chemotherapy and targeted therapy *in vivo* at an early time point. Autofluorescence imaging on a cellular level is well-suited for analysis of heterogeneity across single cells. In particular, a heterogeneity index can quantify drug-induced shifts in heterogeneity across treatment groups for individual variables, and dimensionality reduction techniques can be advantageous for holistic interpretation of multivariate measures of cellular heterogeneity. These methods for assessing tumor heterogeneity could enable improved treatment regimens that account for tumor heterogeneity, leading to improved outcomes for cancer patients.

4.6 Acknowledgements

The Vanderbilt University Translational Pathology Shared Resource was used for immunohistochemistry staining. Funding sources include the NIH R01 CA185747 (M.C.S.), DoD W81XWH-13-1-0194 (M.C.S.), Mary Kay Foundation 067-14 (M.C.S.), NSF Graduate Research Fellowship DGE-0909667 (A.T.S.), NIH/NCI R25 CA136440-04 (K.E.D.), R00 CA143231-03 (J.M.I.), the Vanderbilt-Ingram Cancer Center (VICC, P30 CA68485), and VICC Ambassadors (J.M.I, M.C.S.).

CHAPTER 5

EX VIVO LABEL-FREE MICROSCOPY OF HEAD AND NECK CANCER PATIENT TISSUES

Shah AT, Skala MC, "*Ex Vivo* Label-Free Microscopy of Head and Neck Cancer Patient Tissues." SPIE Proceedings, 2015; 9329

5.1 Abstract

Standard methods to characterize patient tissue rely on histology. This technique provides only anatomical information, so complementary imaging methods could provide beneficial phenotypic information. Cancer cells exhibit altered metabolism, and metabolic imaging could be applied to better understand cancer tissue. This study applies redox ratio, fluorescence lifetime, and second harmonic generation (SHG) imaging to *ex vivo* tissue from head and neck cancer patients. This high-resolution imaging technique has unique advantages of utilizing intrinsic tissue contrast, which eliminates the need for sample processing or staining, and multiphoton microscopy, which provides depth sectioning in intact tissue. This study demonstrates feasibility of these measurements in patient tissue from multiple anatomical sites and carcinoma types of head and neck cancer.

5.2 Introduction

Head and neck cancer is a complex disease encompassing several anatomical sites including the oral cavity, pharynx, larynx, salivary glands, and thyroid[108]. Current methods to characterize malignant and benign patient tissue rely on histology, which requires tissue to be

fixed, sectioned, and stained for visualizing the anatomy of cells. Histology can be difficult to interpret because it lacks functional information to explain the causes of tissue morphology. Therefore, additional imaging methods could provide complementary phenotypic information for characterizing tissue samples. In particular, cancer cells exhibit altered metabolism, which can drive changes in cell morphology, cell proliferation, and cell death[7][109].

Cellular metabolism can be investigated using autofluorescence of nicotinamide adenine dinucleotide (NADH) and flavin adenine dinucleotide (FAD), which are involved in glycolysis and oxidative phosphorylation. The optical redox ratio is calculated by dividing the fluorescence intensity of NADH by that of FAD and provides a measure of global metabolism[46],[52],[51]. The fluorescence lifetime is the time a fluorophore is in the excited state before relaxing to the ground state and is influenced by fluorophore microenvironment, particularly protein-binding[39]. These techniques combined with multiphoton fluorescence microscopy provide micron-level resolution imaging. Additionally, this setup enables imaging of second harmonic generation (SHG), a nonlinear optical process produced by highly ordered proteins like collagen, which are important in tumor microenvironments[110]. These imaging methods utilize intrinsic tissue contrast, which eliminates cost and time for tissue processing that is required in histology. Furthermore, multiphoton microscopy enables depth sectioning in intact tissue and could allow three-dimensional reconstruction[42]. This microscopy technique combines redox ratio imaging, fluorescence lifetime imaging of NADH and FAD, and collagen SHG imaging to provide metabolic and structural information valuable for understanding samples of human tissue.

Previous studies have applied autofluorescence imaging to human head and neck cancer cells and tissue. In cultures of oral cavity cells *in vitro*, autofluorescence intensity and lifetime imaging of NADH and FAD have been shown to distinguish malignant from nonmalignant

human cell lines[96]. Studies in human tissue focus on fluorescence intensity imaging. In particular, patient samples from normal, malignant, and inflammatory tissue of the oral cavity have been characterized using confocal microscopy[111]. Additionally, *in vivo* autofluorescence imaging and spectroscopy for head and neck cancer have used fiber optic probes to diagnose malignant tissue[112],[113]. Complementing fluorescence intensity with fluorescence lifetime and SHG imaging could provide valuable contrast without requiring additional processing of the tissue sample.

The goal of this study is to apply redox ratio, fluorescence lifetime, and SHG imaging to acquire functional and structural images of *ex vivo* human tissue from head and neck cancer patients. Tissue samples were collected from multiple types of head and neck cancer, and images were acquired. These results establish feasibility of these measurements in human head and neck cancer tissue. Overall, this metabolic imaging technique could serve as a valuable method to acquire phenotypic information from intact tissue as a complementary method to histology.

5.3 Methods

Tissue Sample Collection

An institutional review board (IRB) exemption letter was obtained and de-identified human tissue samples were collected using the Cooperative Human Tissue Network (CHTN) at Vanderbilt University. After excision, tissue was placed in Dulbecco's Modified Eagle Medium (DMEM) cell culture media supplemented with 10% fetal bovine serum (FBS) and 0.4µg/mL hydrocortisone and kept on ice. Tissue was moved to a glass-bottomed petri dish (MatTek) for image acquisition.

Image Acquisition

An inverted multiphoton microscope and time correlated single photon counting (TCSPC) electronics were used to collect fluorescence intensity and lifetime images, as described previously[96]. Briefly, a titanium:sapphire laser was used for excitation and a photomultiplier tube was used for collection. NADH signal was isolated using an excitation wavelength of 750nm and a bandpass emission filter of 440/80nm. FAD signal was isolated using an excitation wavelength of 890nm and a bandpass emission filter of 550/100nm. SHG signal was isolated using an excitation wavelength of 890nm and a bandpass emission filter of 450/35nm. NADH autofluorescence, FAD autofluorescence, and SHG images were acquired from the same fields of view. Intensity images were averaged over 4 frames to improve signal to noise. Fluorescence lifetime images were acquired over 60 seconds.

Image Analysis

An NADH intensity image was divided by a FAD intensity image from the same field of view to calculate a redox ratio image (ImageJ). The fluorescence lifetime was calculated by deconvolving the instrument response function with the fluorescence lifetime decay and fitting to a two-component curve, as described previously[96]. The average fluorescence lifetime, τ_m, was calculated by $\tau_m=\alpha_1\tau_1 + \alpha_2\tau_2$, where α is the contribution from each component and τ is the lifetime of each component.

5.4 Results

Patient tissue of malignant tongue was collected and imaged (Figure 5.1). Hematoxylin and eosin (H&E) stain shows tightly packed cells and verifies malignant status of the tissue.

Representative redox ratio, NADH lifetime, and FAD lifetime images highlight morphology of tumor cells, particularly the cell cytoplasm that emanates NADH and FAD autofluorescence.

Squamous cell carcinoma (SCC) tissue of the tongue and matched normal tissue of the tongue were collected from the same patient and imaged (Figure 5.2). The SCC tissue shows cells with nuclei compared with the normal tissue that shows vesicles resembling adipocytes with higher redox ratios. Additionally, the SCC tissue exhibits lower NADH and FAD fluorescence lifetimes than the normal tissue. SHG from collagen is arranged in the extracellular matrix surrounding cells.

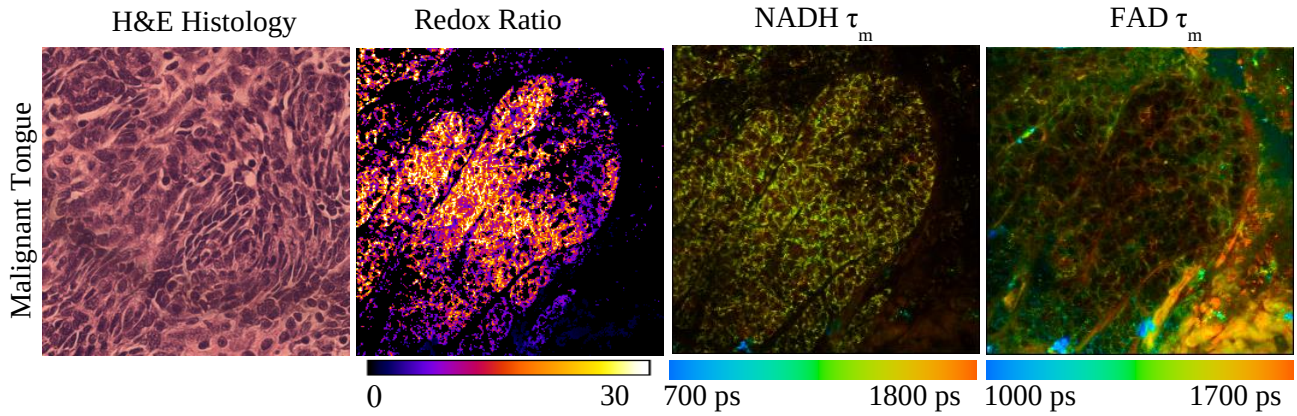

Figure 5.1. Representative hematoxylin and eosin (H&E) histology stain (60x60µm image size), redox ratio, NADH lifetime, and FAD lifetime images (170x170µm image size) from malignant tongue.

Samples were acquired from patients with adenocarcinoma of the parotid salivary gland and SCC of the parotid salivary gland (Figure 5.3). The adenocarcinoma tissue shows higher redox ratios and lower NADH and FAD fluorescence lifetimes than the SCC tissue. The adenocarcinoma sample shows more collagen than the SCC sample. One sample was acquired from a patient with laryngeal cancer (Figure 5.4), and microscopy images show larger cells compared with the other carcinoma samples.

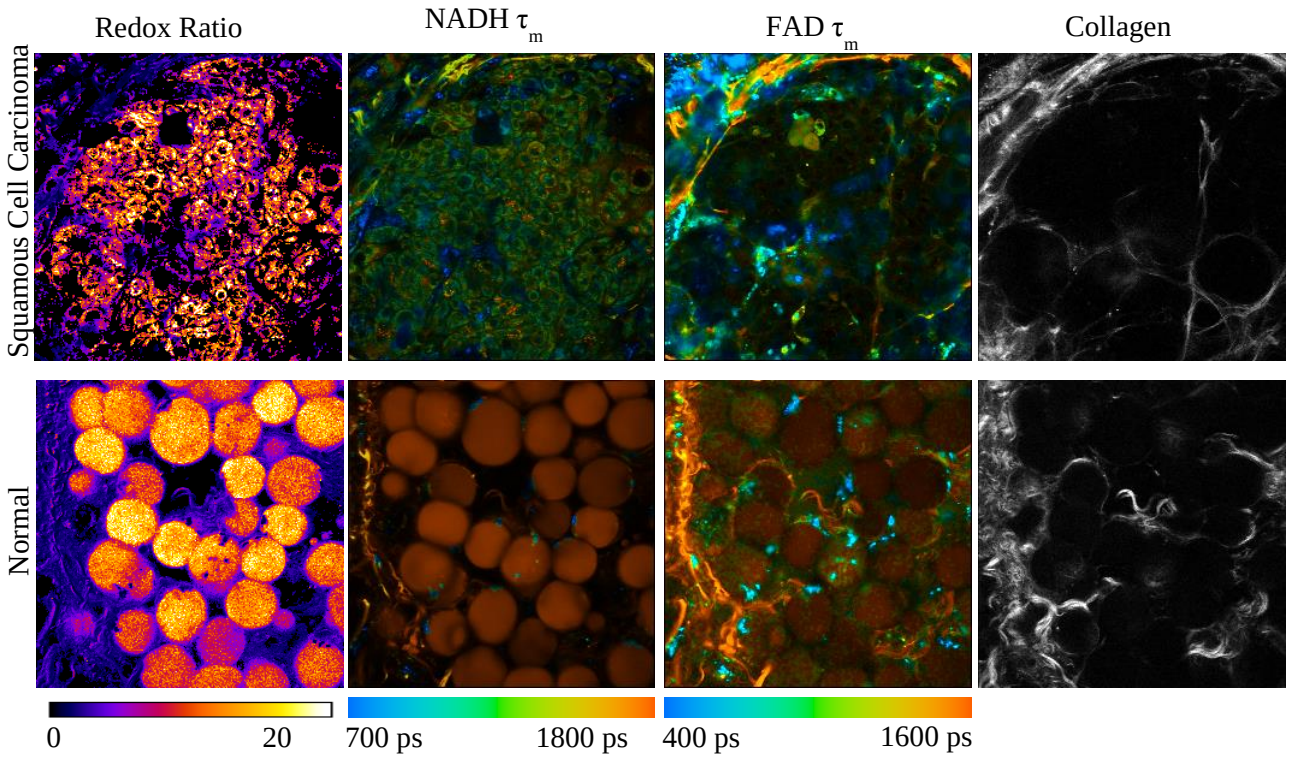

Figure 5.2. Representative images from squamous cell carcinoma of the tongue (top row) and normal tissue (bottom row) from the same patient. Images are 170x170µm.

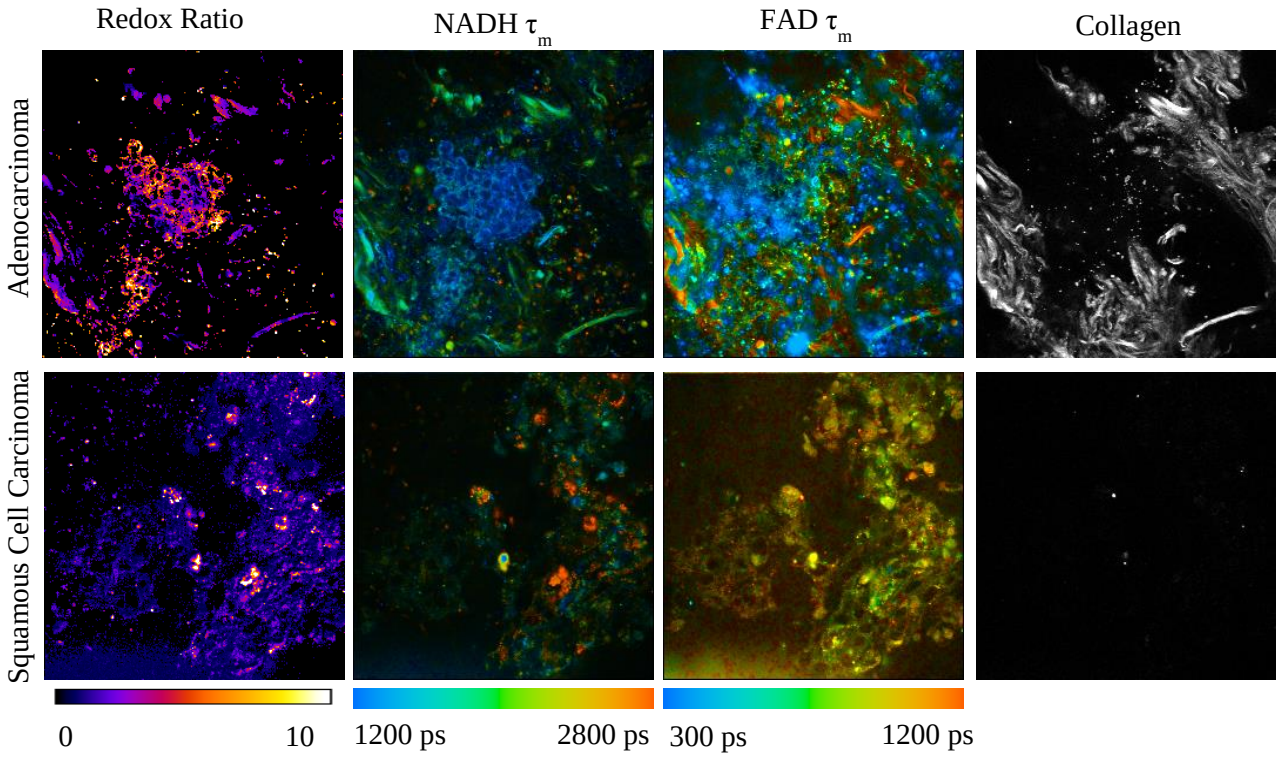

Figure 5.3. Representative images from adenocarcinoma (top row) and squamous cell carcinoma (bottom row) from the parotid salivary gland. Images are 170x170µm.

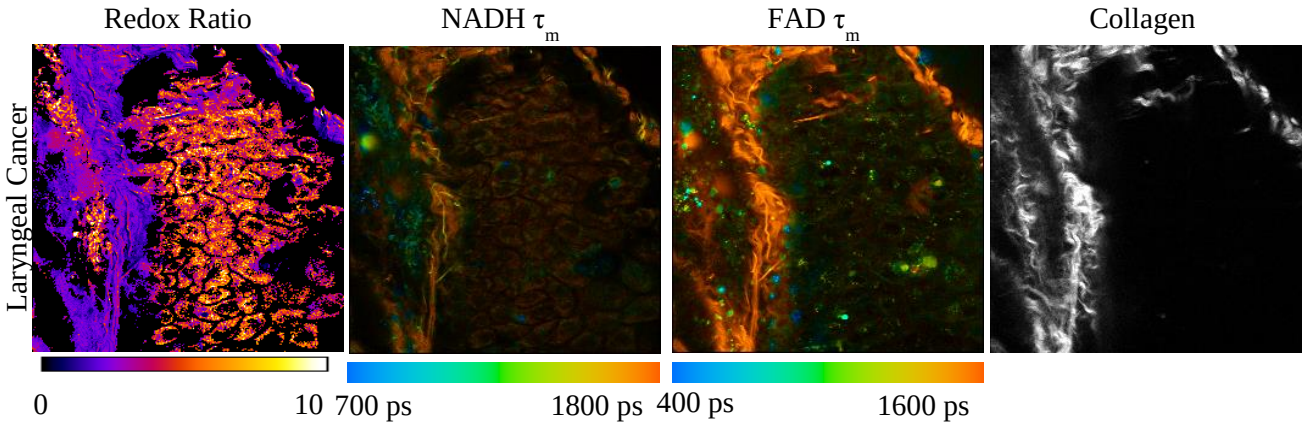

Figure 5.4. Representative images from patient tissue of laryngeal cancer. Images are 170x170µm.

5.5 Discussion

The goal of this study is to establish feasibility of applying redox ratio, fluorescence lifetime, and SHG imaging to human tissue samples of head and neck cancer. Patient tissues from multiple anatomical sites were imaged, including the tongue, parotid salivary gland, and larynx. Additionally, a matched normal sample from a patient with SCC of the tongue was obtained. Autofluorescence images from normal tissue and SCC tissue show cell morphology and different cell types, particularly fat vesicles in the normal tissue versus tumor cells in the SCC tissue. The normal and SCC tissue exhibit distinct fluorescence lifetimes of NADH and FAD, which reflects differences in protein-binding involving NADH and FAD for each sample (Figure 5.2). Head and neck cancer can also include multiple cell types of origin. For example, adenocarcinoma originates from glandular cells whereas SCC originates from squamous cells. Adenocarcinoma tissue of the parotid salivary gland shows higher optical redox ratios than SCC, reflecting higher rates of glycolysis compared with oxidative phosphorylation (Figure 5.3). Differences in NADH and FAD fluorescence lifetime between the adenocarcinoma and SCC reflect different metabolic pathways utilized for each tissue type. These functional measurements could help influence treatment strategies because anti-cancer treatment often impacts cellular metabolism. Since tumor cells exhibit increased NADH autofluorescence in the cytoplasm compared with the nuclei, NADH autofluorescence images can provide visualization of cellular and nuclear size. Autofluorescence imaging of laryngeal cancer shows increased cellular and nuclear size compared with SCC of the tongue, SCC of the parotid salivary gland, and adenocarcinoma of the parotid salivary gland. Overall, high-resolution functional imaging of human tissue could serve as a method to characterize tissue phenotype and provide a

complementary imaging method to histology that does not require processing and destruction of the tissue samples.

5.6 Acknowledgements

Funding sources include the NSF Graduate Research Fellowship DGE-0909667 and the NIH R01-CA185747.

CHAPTER 6

METABOLIC IMAGING OF HEAD AND NECK CANCER ORGANOIDS

6.1 Abstract

Head and neck cancer patients suffer from toxicities, morbidities, and mortalities, and these ailments could be minimized through improved therapies. Drug discovery is a long, expensive, and complex process, so optimized assays can improve the success rate of drug candidates. This study applies optical imaging of cell metabolism to three-dimensional *in vitro* cultures of head and neck cancer grown from primary tumor tissue (organoids). This technique is advantageous because it measures cell metabolism using intrinsic fluorescence from NAD(P)H and FAD on a single cell level for a physiologically-relevant *in vitro* model. Head and neck cancer organoids are characterized alone and after treatment with standard therapies, including an antibody therapy, a chemotherapy, and combination therapy. Additionally, organoid cellular heterogeneity is analyzed quantitatively and qualitatively. Gold standard measures of treatment response, including cell proliferation, cell death, and tumor volume, validate therapeutic efficacy in each treatment group. Results indicate that optical metabolic imaging is sensitive to therapeutic response in organoids after 1 day of treatment ($p<0.05$) and resolves cell subpopulations with distinct metabolic phenotypes. Ultimately, this platform could provide a sensitive and physiologically-relevant high-throughput assay to streamline the drug discovery process for head and neck cancer.

6.2 Introduction

Head and neck cancer describes malignant tumors in the mouth, nose, and throat. Current treatments include chemotherapy, surgery, radiation therapy, and targeted therapy. Despite advancements in therapies, the 5-year survival rate for head and neck cancer is between 40-50% [1]. Additionally, chemotherapy, surgery, and radiation therapy introduce major toxicities, including damage to tissue and organs in anatomical sites that are critical for breathing, eating, and talking [114]. Therefore, organ preservation is an important consideration to maintain normal function. Targeted treatments for head and neck cancer focus on inhibition of the epidermal growth factor receptor (EGFR), particularly with the anti-EGFR antibody cetuximab [4]. However, there is a lack of targeted therapies beyond EGFR inhibitors. Additionally, tumor heterogeneity can allow a minority population of cells to drive treatment resistance and tumor recurrence [54]. Optimized therapies could provide better treatment efficacy and reduced toxicities, leading to improved quality of life and longer survival, but drug development takes at least 10 years and more than $1 billion [115][116]. Therefore, more accurate rapid drug screens to identify the most promising drug candidates and combination treatments would increase the success rate during drug development and facilitate the commercialization of optimized drugs and combinations.

In vitro three-dimensional cultures grown from primary tumor tissue (organoids) are attractive for a high-throughput drug screen that enables testing of multiple drugs and drug combinations. Cellular level measurements can identify cell subpopulations that exhibit different sensitivities to treatments, and organoids combined with high-resolution imaging of cell metabolism provides a promising platform. Organoids are physiologically relevant because they grow in a three-dimensional organization, are generated from tumor tissue, and can therefore

capture distinct behaviors of individual tumors [117]. Additionally, multiphoton microscopy of cell metabolism has been shown to resolve therapeutic response in cancer [52][96], and the spatial scales of this imaging technique allow the full volume of the organoid to be imaged on a single-cell level. Autofluorescence measurements of the metabolic cofactors NAD(P)H and FAD characterize cell metabolism using their fluorescence intensities and lifetimes [46][39]. The fluorescence intensity measures relative amounts of each cofactor and the optical redox ratio, defined as the fluorescence intensity of NAD(P)H divided by that of FAD, reflects global cell metabolism. The fluorescence lifetime measures the amount of time a molecule is in the excited state, reflects protein-binding, and is sensitive to cellular signaling pathways that use NAD(P)H and FAD. Metabolic imaging based on cellular autofluorescence provides early, sensitive measurements of anti-cancer treatment response [52].

Organoids have been established and characterized for some types of cancers, including breast cancer and pancreatic cancer [118][119]. Different anatomical sites exhibit different cell types, cell structures, media and growth factor requirements, matrix stiffness requirements, and tissue digestion protocols, so characterization of each tumor type is necessary. Previous studies have focused on culturing spheroids from head and neck cancer cell lines [120], organoids from human salivary glands [121], and tumor pieces from head and neck cancer patients [122]. Therefore, characterization and analysis of head and neck cancer organoids grown from primary tumor tissue would be a new and beneficial contribution.

The lack of targeted treatments for head and neck cancer justify the need for a high-throughput drug screen. This study describes properties of tumor tissue that can be used for growing head and neck cancer organoids, establishes a protocol for generating the organoids, and applies metabolic microscopy for non-invasively characterizing organoids alone and in response

to drug treatments. Overall, this technique could be applied to streamline drug discovery and enable the development of optimized therapies with high efficacy and low toxicity.

6.3 Materials and Methods

Tissue Culture and Tumor Inoculation

FaDu cells were grown in Dulbecco's Modified Eagle Medium (DMEM) plus 10% fetal bovine serum (FBS) and 0.4 µg/mL hydrocortisone. Subcutaneous flank tumors were inoculated in nude mice with 10^7 FaDu cells. Tumors were grown for 1-2 weeks until reaching a volume of ~100mm^3. For *in vivo* imaging the mouse was anesthetized, the tumor was exposed, and the mouse was placed on the microscope. Organoid media consisted of DMEM plus 10% FBS, 0.4 µg/mL hydrocortisone, 1% penicillin: streptomycin, insulin-transferrin-selenium at a 1X concentration, 10ng/mL epidermal growth factor, and B27 at a 1X concentration. Treatment media for organoids included cetuximab (20nM) [104], cisplatin (33µM) [78], or their combination.

Organoid Generation

Mice were anesthetized and tumors were excised and immediately placed in chilled culture media. Tumors were washed 3 times with sterile phosphate buffered saline (PBS), transferred to 35mm petri dishes with 0.5mL culture media, and mechanically digested with scissors. Digestion into a cellular suspension was confirmed with brightfield microscopy. The cell suspension was mixed with matrigel at a volume ratio of 1 part cell suspension to 2 parts matrigel, and 100µL was plated on each 35mm glass-bottomed imaging dish (MatTek). The gels solidified at room

temperature for 30 minutes and then at 37C for 1 hour. Then 2mL organoid media was added to each dish and organoids were grown at 37C.

Tumor Growth Curves and Immunohistochemistry

Mice with FaDu tumors were treated 3 times a week for 2 weeks with cetuximab (33mg/kg) [92][93], cisplatin (6mg/kg) [94], or their combination via intraperitoneal injection (6 tumors per group). Tumor volumes were measured once a day using calipers, and tumor volumes were calculated by $(l*w^2)/2$, where l is the tumor length and w is the tumor width. Tumor volumes were normalized to the size on day 1. On day 11 for the combination treated mice or day 13 for the single agent treated mice, tumors were excised and fixed for immunohistochemistry, and the mice were euthanized. Weight loss in the combination treatment group required an end of the treatment course on day 11.

Fluorescence Microscopy

Instrumentation for fluorescence microscopy included an inverted multiphoton microscope (Bruker), a tunable titanium:sapphire laser (Coherent) for fluorescence excitation, and a Ga:AsP photomultiplier tube for collection. Time correlated single photon counting (TCSPC) electronics (SPC-150, Becker and Hickl) were used for fluorescence lifetime acquisition. NAD(P)H was imaged using an excitation wavelength of 750nm and a collection filter of 400-480nm. FAD was imaged using an excitation wavelength of 900nm and a collection filter of 500-600nm. NAD(P)H and FAD were imaged from the same fields of view. Microscopy was performed to collect images of 256x256 pixels using a 40X objective (1.3NA), 4.8 µsecond pixel dwell time, 60 second collection time, and ~10mW excitation power. Photon count rates were monitored to

ensure the absence of photobleaching. A Fluoresbrite YG microsphere (Polysciences Inc.) was measured at each imaging session, and provided a lifetime of 2.10 ± 0.02 ns (n=5), which agrees with previous reported values [32][95]. The instrument response function (IRF) was measured using second harmonic generation of urea crystals resulting in a full width at half max of 244ps. For organoid and tumor imaging, 4-6 fields of view were acquired per group.

Image Analysis

Images were analyzed using SPCImage (Becker and Hickl), as described previously [123]. Spatial binning included each pixel and the surrounding 8 pixels. The fluorescence decay curves were de-convolved with the IRF and fit to a 2-component exponential function, $F(t) = \alpha_1 e^{-t/\tau 1} + \alpha_2 e^{-t/\tau 2}$. Here, α represents the contribution from each component, τ represents the fluorescence lifetime of each component, and the 2 components reflect free and protein-bound forms of NAD(P)H and FAD [32]. For NAD(P)H the short lifetime reflects the freely diffusing conformation while the long lifetime reflects the bound conformation. Conversely, for FAD the short lifetime reflects the bound conformation while the long lifetime reflects the freely diffusing conformation [39]. The mean lifetime was calculated by $\tau_m = \alpha_1\tau_1 + \alpha_2\tau_2$. The optical redox ratio was calculated as the fluorescence intensity of NAD(P)H divided by the fluorescence intensity of FAD for each pixel. CellProfiler was applied to analyze images on a per-cell basis, as described previously [97]. Bar plots are consistent across 3 replicates.

Heterogeneity Analysis

Heterogeneity analysis was performed as described previously [123]. Briefly, per-cell data was plotted as frequency distributions and fit to 1, 2, or 3 Gaussian curves based on the Akaike

Information Criterion, where each Gaussian curve represented a cell subpopulation. Validation of this approach has shown accuracy within 10% *in vitro* [98]. The sum of the Gaussian curves was plotted. A heterogeneity index, based on a weighted Shannon diversity index, was applied to quantify cellular heterogeneity using the equation $\boldsymbol{H = -\sum d_i p_i ln p_i}$ [123]. Here, *i* represents each subpopulation, d represents the distance between the median of the subpopulation and the median of all data within a group, and p represents the proportion of the subpopulation. For spatial mapping of cell subpopulations, thresholds between each subpopulation were calculated as values equidistant from the Gaussian curve means. The nucleus of each cell was color-coded according to these threshold values. Spatial heterogeneity analysis is shown for 1 replicate.

Statistical Analysis

Bar graphs are shown as mean ± standard error. For microscopy images statistical significance was determined using a Student's t-test. For tumor growth curves and immunohistochemistry statistical significance was determined using a Wilcoxon rank sum test and Bonferroni correction. An α of 0.05 defined statistical significance.

6.4 Results

Tumor tissue used to generate organoids was characterized with immunohistochemistry, histology, and autofluorescence imaging (Figure 6.1). Cleaved caspase-3 staining shows minimal cell death and ki-67 staining shows high cell proliferation (Figure 6.1A, B). H&E staining indicates tissue composition of dense tumor cells (Figure 6.1C). Cytokeratin AE1/AE3 staining demonstrates the epithelial status of the majority of cells (Figure 6.1D). Autofluorescence images show packed tumor cells with high NAD(P)H intensity localized in the cell cytoplasm and FAD

intensity localized in mitochondria (Figure 6.1E, F). These observations were confirmed in consultation with a trained pathologist. Tumor tissue was mechanically digested to break up the structural component and generate a suspension of single cells or small groups of cells (Figure 6.1G), which enables organoids to grow as multi-cellular aggregates (Figure 6.1H).

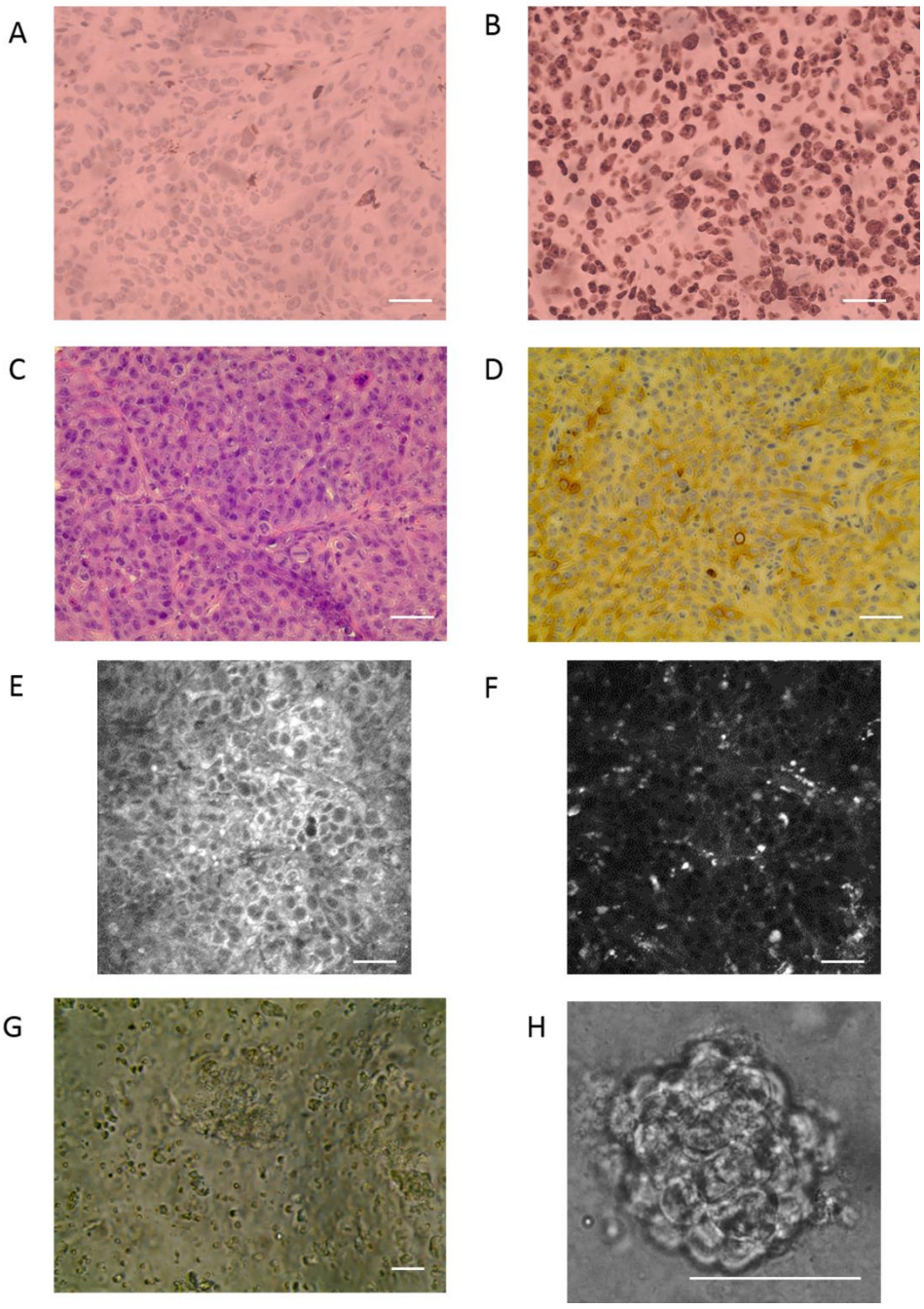

Figure 6.1. Representative immunohistochemistry, histology, and autofluorescence images of tumor tissue and brightfield microscopy for organoid generation. (A) Cleaved caspase-3 staining shows minimal apoptosis. (B) Ki-67 staining demonstrates high cell proliferation. (C) H&E staining indicates tissue composition of dense tumor cells. (D) Cytokeratin AE1/AE3 indicates positive staining of epithelial cells, which constitute the majority of the tumor. (E) NAD(P)H

autofluorescence shows NAD(P)H located in the cell cytoplasm. (F) FAD autofluorescence shows punctate fluorescence signal from mitochondrial FAD. (G) Tissue was mechanically digested to create a suspension of cells. (H) Cells grow as organoids after plating the cell suspension. Scale bar = 50um.

Fluorescence lifetime values are robust and self-referenced, enabling comparisons across data sets and between tumor tissue and organoids (Figure 6.2). Organoids exhibit higher mean lifetimes of NAD(P)H and FAD than *in vivo* tumors ($p<0.05$), which results from lower contributions of the short lifetime (α_1) and higher values of the short and long fluorescence lifetimes (τ_1 and τ_2) (Figure B.1). Frequency distribution modeling of the fluorescence lifetimes qualitatively illustrates shifts toward higher lifetimes for organoids compared with tumor tissue. Additionally, the heterogeneity index (H) quantifies cellular heterogeneity, where an increased heterogeneity index reflects increased number of cell subpopulations, increased equality in the weights of the subpopulations, or increased separation between the subpopulations [123]. Organoids exhibit similar cellular heterogeneity compared with the *in vivo* tumor based on the NAD(P)H fluorescence lifetime and increased cellular heterogeneity compared with the *in vivo* tumor based on the FAD fluorescence lifetime.

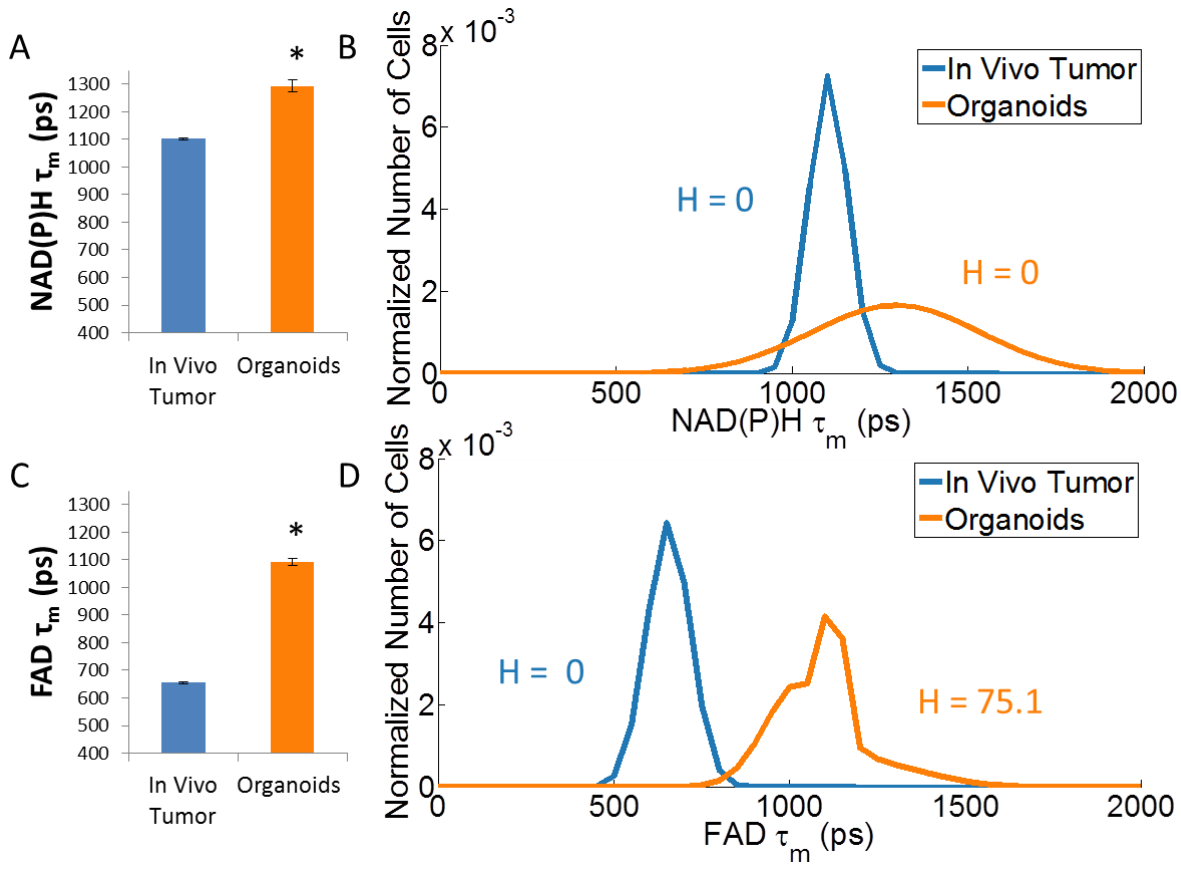

Figure 6.2. Untreated organoids and *in vivo* tumor tissue display distinct optical metabolic imaging properties. The weighted mean is calculated by $\tau_m = \alpha_1\tau_1 + \alpha_2\tau_2$, where τ represents the lifetime value and α represents the contribution from each component. (A, C) Organoids exhibit higher NAD(P)H and FAD fluorescence lifetimes (τ_m) compared with *in vivo* tumor tissue, which is explained by lower contributions of the short lifetime component (α_1), higher values of the short fluorescence lifetime (τ_1), and higher values of the long fluorescence lifetime (τ_2) (See Figure B.1). (B, D) Population distribution analysis plots cellular heterogeneity for *in vivo* tumor tissue compared with organoids. The heterogeneity index (H) is similar between organoids and *in vivo* tumor based on the NAD(P)H fluorescence lifetime and increases for organoids compared to *in vivo* tumor based on the FAD fluorescence lifetime. *p<0.05, t-test, n~100-300 cells per group

A representative autofluorescence image demonstrates the NAD(P)H fluorescence intensity in the organoids (Figure 6.3). In particular, organoids exhibit populations of cells with high NAD(P)H intensity as well as cells with low NAD(P)H intensity, and these populations exhibit distinct metabolic properties. Cells with low NAD(P)H exhibit a lower redox ratio and higher FAD fluorescence lifetime, explained by a lower contribution of the short lifetime (α_1) (Figure B.2), compared with cells with high NAD(P)H ($p<0.05$).

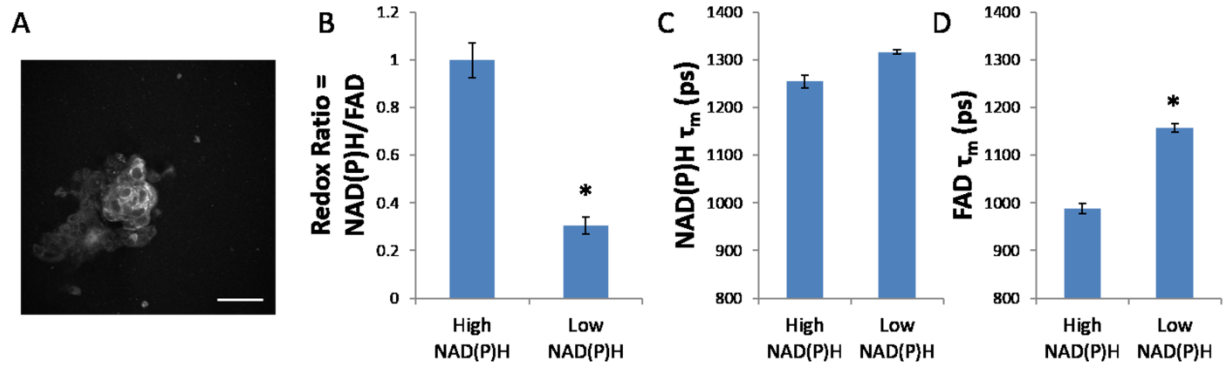

Figure 6.3. Untreated organoids contain cells with high levels of NAD(P)H intensity and cells with low levels of NAD(P)H intensity. (A) A representative image shows organoids with two levels of NAD(P)H intensity. (B) Low NAD(P)H cells exhibit a lower optical redox ratio than high NAD(P)H cells. (C) Low and High NAD(P)H cells exhibit similar NAD(P)H lifetimes. (D) Low NAD(P)H cells exhibit a higher FAD lifetime than high NAD(P)H cells. Scale bar = 50um. *$p<0.05$, t-test, n~50-100 cells per group

Gold standard techniques validate therapeutic efficacy and measure *in vivo* response to treatment. Immunohistochemistry characterizes short-term and long-term effects of treatment on cell proliferation measured by ki-67 and cell death measured by cleaved caspase 3 (Figure 6.4). Two days after *in vivo* treatment, cell proliferation is consistent across all treatment groups and

cell death increases with cisplatin treatment (Figure 6.4A, B). Two weeks after treatment cell proliferation decreases with cetuximab, cisplatin, and combination treatment and cell death increases with cisplatin and combination treatment (Figure 6.4C, D) ($p<0.05$). Tumor growth curves illustrate long-term *in vivo* response to treatment (Figure 6.4E). Control mice exhibit continual tumor growth, whereas mice treated with single agents of cetuximab or cisplatin exhibit stable tumor volume, and mice treated with the combination of cetuximab and cisplatin exhibit decreased tumor volume.

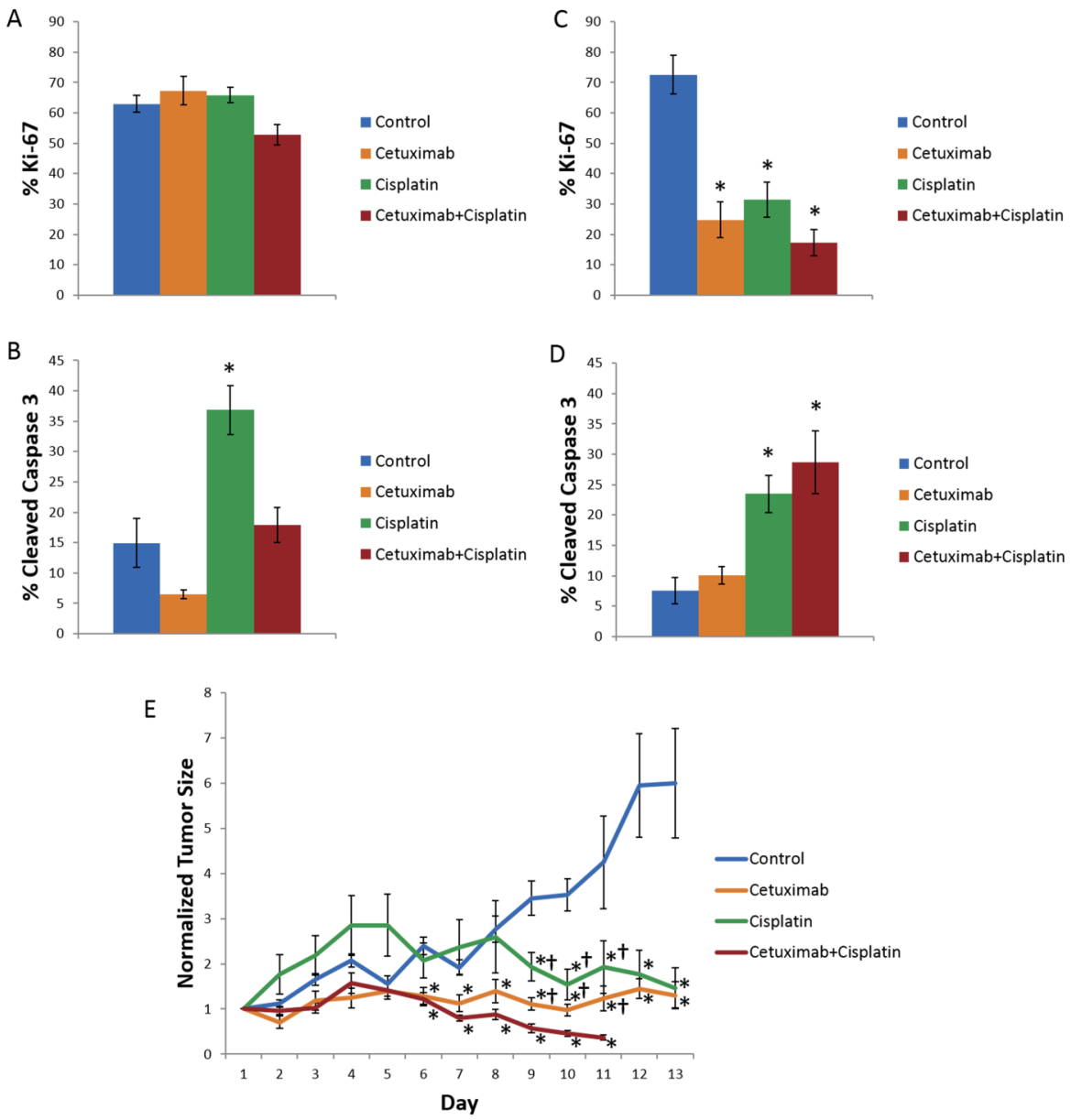

Figure 6.4. Cell proliferation and cell death were quantified using Ki-67 and Cleaved Caspase 3, respectively, in FaDu xenografts after mice were treated for 2 days or 2 weeks, and tumor growth curves show treatment effects over 2 weeks in mice with FaDu xenografts. (A) Cell proliferation is consistent across treatment groups in FaDu xenografts 2 days after treatment. (B) Cell death increases after 2 days of treatment with cisplatin. (C) Cell proliferation decreases after 2 weeks of treatment with cetuximab, cisplatin, and their combination. (D) Cell death increases after 2

weeks of treatment with cisplatin and the combination of cetuximab and cisplatin. (E) Treatment with cetuximab or cisplatin causes stable disease, whereas combination treatment causes response.*$p<0.05$ compared with control, rank sum test; †$p<0.05$, compared with combination treatment, n=6 tumors

Representative images show organoid and cell morphology as well as relative trends in the redox ratio, NAD(P)H lifetime, and FAD lifetime for each treatment group (Figure 6.5). Optical metabolic imaging quantifies drug effects 1 day after treatment in organoids (Figure 6.6). The redox ratio increases with cetuximab and decreases with cisplatin and combination treatment ($p<0.05$). The NAD(P)H fluorescence lifetime (τ_m) decreases with cetuximab, cisplatin, and combination treatment ($p<0.05$). The contribution from the short lifetime (α_1) increases with cetuximab treatment and decreases with cisplatin and combination treatment. The values of the short and long fluorescence lifetimes (τ_1 and τ_2) decrease with cetuximab, cisplatin, and combination treatment (Figure B.3). The FAD fluorescence lifetime (τ_m) increases with cetuximab, cisplatin, and combination treatment ($p<0.05$). The contribution from the short lifetime (α_1) decreases with cetuximab, cisplatin, and combination treatment. The values of the short and long fluorescence lifetimes (τ_1 and τ_2) increase with cetuximab, cisplatin, and combination treatment (Figure B.3).

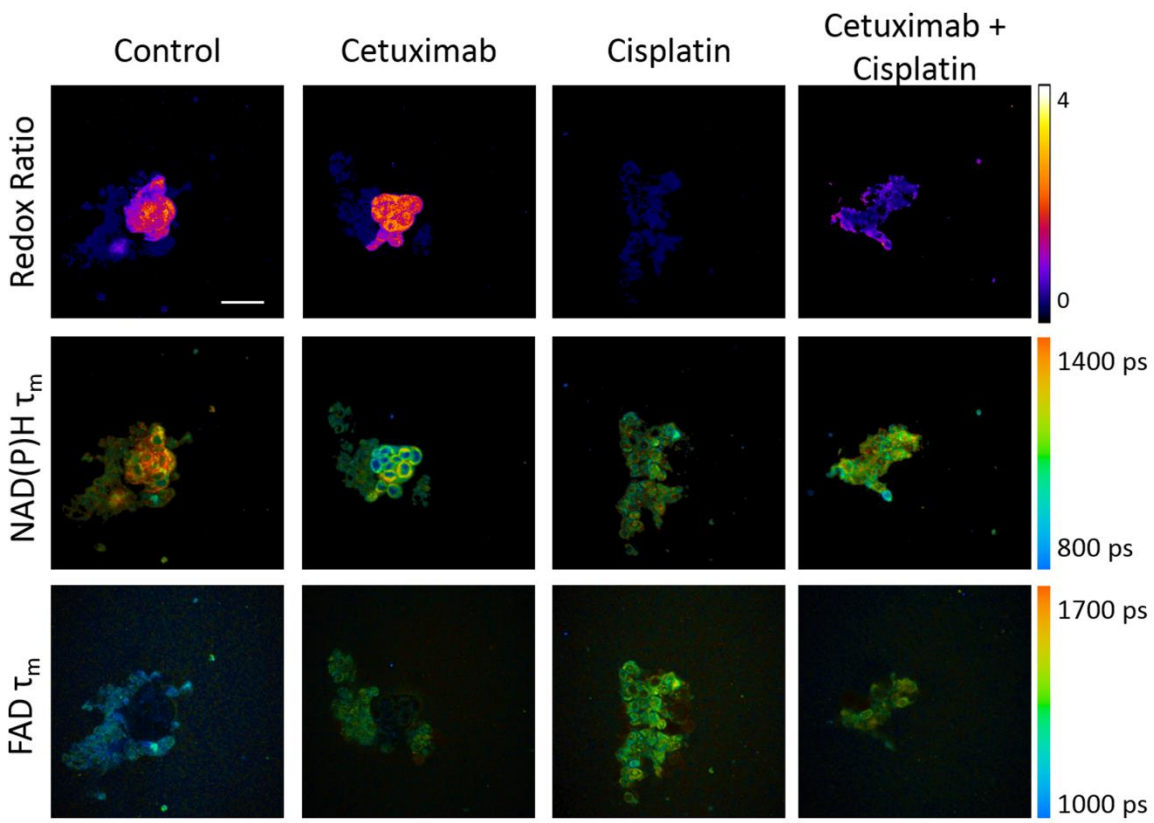

Figure 6.5. Autofluorescence images show the redox ratio and fluorescence lifetimes of NAD(P)H and FAD in head and neck cancer organoids treated for 1 day with cetuximab, cisplatin, or their combination. NAD(P)H and FAD autofluorescence images were acquired from the same fields of view, and the redox ratio (top row), NAD(P)H fluorescence lifetime (middle row), and FAD fluorescence lifetime (bottom row) were calculated. Scale bar = 50um.

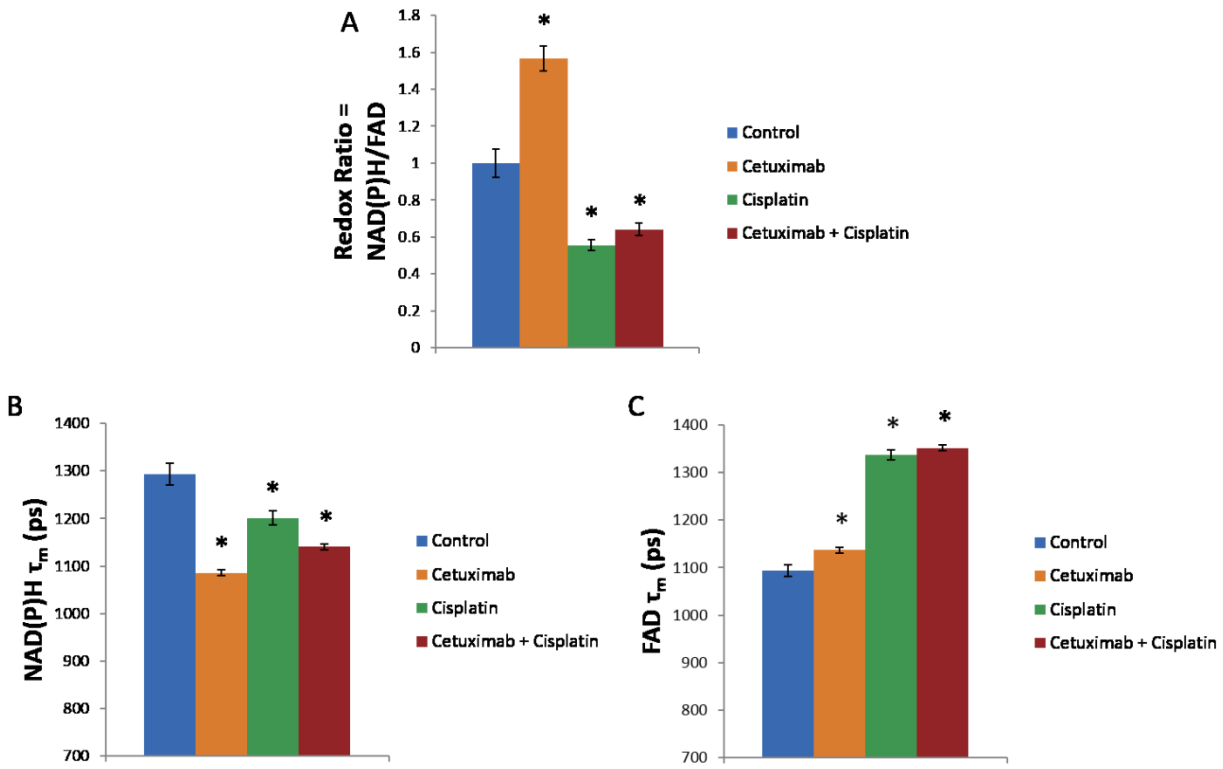

Figure 6.6. The redox ratio and fluorescence lifetimes of NAD(P)H and FAD were quantified in organoids treated for 1 day with cetuximab, cisplatin, or their combination. (A) The redox ratio increases with cetuximab treatment and decreases with cisplatin and the combination treatment. (B) The NAD(P)H lifetime decreases with cetuximab, cisplatin, and combination treatment. (C) The FAD lifetime increases with cetuximab, cisplatin, and combination treatment. *$p<0.05$, t-test; n~50-200 cells per group

Cell subpopulations describe heterogeneity within treatment groups. Heterogeneity analysis applies Gaussian fitting of per-cell data and plots the sum of the Gaussian curves, illustrating shifts toward lower NAD(P)H lifetimes after cetuximab, cisplatin, and combination treatment (Figure 6.7). The control and combination treatment groups exhibit one subpopulation, whereas the cetuximab and cisplatin groups exhibit two subpopulations. For each treatment

group the summed area under the Gaussian curves equals one. Control and combination treated organoids display a low heterogeneity index, whereas single agent treated organoids display a higher heterogeneity index. Additionally, spatial mapping shows localization of the cell subpopulations. Each organoid contains one or both of the subpopulations, and qualitative analysis indicates that cell subpopulations are scattered throughout the organoids.

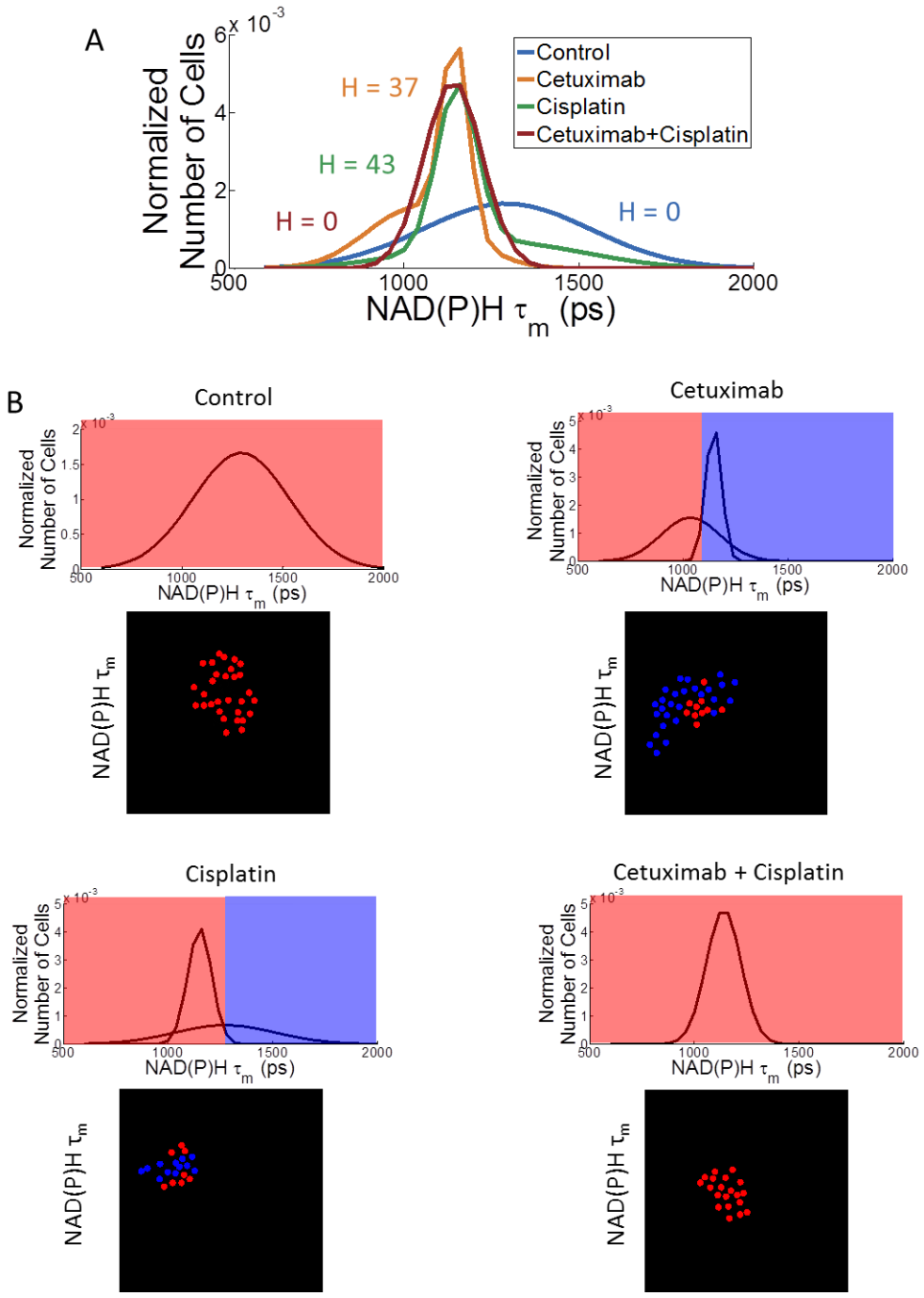

Figure 6.7. Cellular heterogeneity was analyzed based on NAD(P)H fluorescence lifetime in head and neck cancer organoids after 1 day of treatment with cetuximab, cisplatin, and their combination. (A) The sum of Gaussian curve fits provides qualitative visualization of cellular heterogeneity. A heterogeneity index (H) indicates low cellular heterogeneity for the control and combination treatment groups compared with higher heterogeneity for the single agent treatment

groups. (B) Individual Gaussian curves were plotted and thresholds between the means of the Gaussian curves were color coded to inform spatial mapping. The total area under the curves is equal across treatment groups. Spatial mapping provides relative locations of cell subpopulations.

6.5 Discussion

This study characterizes head and neck cancer organoids metabolically and in response to drugs. This approach is advantageous because it utilizes a physiologically-relevant model combined with sensitive metabolic measurements of treatment response. Organoids are generated from tumor tissue and grow in a three-dimensional matrix, which provides a more appropriate model than cell lines grown as monolayers on plastic [124]. Optical metabolic imaging measures early therapeutic effects and characterizes cellular heterogeneity, which is crucial for identifying resistant cells that cause patient failure. Overall, this technique can address a need for high-throughput screens of treatment efficacy for anti-cancer drugs to facilitate drug discovery.

High quality primary tissue facilitates organoid growth. In particular, generating organoids immediately after tissue excision preserves tissue viability. Successful organoids grow from tissue that consists of dense tumor cells with a high proliferation rate and low apoptosis rate (Figure 6.1). Histological analysis indicates that the primary tissue comprises ~97% tumor characterized by proliferative, epithelial cells and ~3% stroma characterized by fibroblasts, capillaries, immune cells, and collagen. Fibroblasts exhibit distinct elongated morphology that would be apparent in culture [125]. Endothelial cells and immune cells would be expected to have short life spans and expire under organoid conditions [126]. In particular, the growth of

endothelial cells is promoted by shear stress [127], which is largely absent in these cultures. This analysis suggests that the organoids comprise epithelial cells.

Protein-binding causes a conformational change in the molecular structure of NAD(P)H and FAD, which affects fluorescence quenching and the fluorescence lifetime [39]. The distinct fluorescence lifetime properties between *in vivo* tumor tissue and organoids reflect distinct protein-binding activity, including different rates that these molecules are being used in cell signaling pathways and binding to different proteins (Figure 6.2). These differences could result from discrete microenvironment conditions, including nutrient availability and oxygenation between *in vivo* tumors and *in vitro* cultures. This characterization highlights the utility of organoids as a complementary tool to *in vivo* imaging by enabling rapid comparisons of metabolic states between treated and control organoids generated from the same tissue.

Cell subpopulations with distinct metabolic phenotypes are present in the control organoids (Figure 6.3). Organoids contain cells with high levels of NAD(P)H intensity and cells with low levels of NAD(P)H intensity ($p<0.05$). Low-NAD(P)H cells exhibit a lower redox ratio than high-NAD(P)H cells ($p<0.05$), reflecting distinct metabolic characteristics. Previous studies have shown that a decrease in redox ratio corresponds to a decrease in cell proliferation [96], thus these two subpopulations of cells may have varied drug response. Additionally, these subpopulations exhibit different FAD fluorescence lifetimes and contributions from free FAD (Figure B.2, $p<0.05$), indicating different levels of protein-binding between these cell subpopulations. The lack of a tumor stroma in the organoids could enable these separate subpopulations of cells to grow [128].

Traditional measures of therapeutic response characterize each treatment group. Immunohistochemistry shows minimal treatment effects 2 days after treatment and measures

treatment response after 2 weeks of treatment (Figure 6.4). Cetuximab has been shown to induce autophagy instead of apoptosis [104]. Overall, these results indicate that the endpoints of cell proliferation and cell death require multiple courses of treatment to resolve treatment effects. Tumor growth curves show that control tumors exhibit disease progression, the single agent treatments both exhibit stable disease, and the combination treatment exhibits treatment response (Figure 6.4E). These results reflect the synergistic effect of cetuximab and cisplatin, because cetuximab enhances chemotherapy-induced cell death by inhibiting DNA repair mechanisms [18]. These results agree with clinical studies of patients administered cetuximab, cisplatin, or their combination [102][103][105].

Representative images show the morphology and arrangement of tumor cells in organoids after 1 day of treatment as well as qualitative differences in the redox ratio, NAD(P)H fluorescence lifetime, and FAD fluorescence lifetime across treatment groups (Figure 6.5). Additionally, optical metabolic imaging quantitatively demonstrates sensitivity to drug effects after 1 day of treatment (Figure 6.6), which is an earlier time point compared with cell death, cell proliferation, and tumor volume (Figure 6.4). Cetuximab treatment causes an increase in the redox ratio, which is consistent with decreased efficacy of cetuximab as a monotherapy [118][96]. Cisplatin treatment causes a decrease in the redox ratio, which is consistent with drug responsiveness in previous *in vitro* and *in vivo* studies [96][123]. Combination treatment causes a decrease in the redox ratio, which is previously unreported. Taken together these results suggest that a decrease in the redox ratio indicates treatment response compared with an increase or no change in redox ratio for less effective treatments.

The organoids NAD(P)H fluorescence lifetime (τ_m) decreases with cetuximab, cisplatin, and combination treatments (Figure 6.6B, $p<0.05$), which is consistent with previous *in vivo*

results [123]. The organoids FAD fluorescence lifetime (τ_m) increases with cetuximab, cisplatin, and combination treatments (Figure 6.6C, $p<0.05$). This shows the opposite trend from previous *in vivo* results and reflects the difference in microenvironments between *in vivo* and *in vitro* conditions, including access to oxygen and nutrients, vascularization, stromal structure, and drug delivery. Overall, these results indicate that organoids combined with optical metabolic imaging provides a unique *in vitro*, three-dimensional model that harnesses intrinsic contrast for measuring early, sensitive drug effects on a single-cell level.

Tumor heterogeneity describes multiple cell subpopulations that can respond to therapies with different sensitivities, and cells that are resistant to treatment can enable patient relapse. In particular, Gaussian fitting of cellular data can characterize cellular heterogeneity, and a heterogeneity index, H, can incorporate the number of subpopulations, evenness of subpopulations, and relative distance between subpopulations to quantify cellular heterogeneity [98][123]. Based on the heterogeneity index, organoids treated with the single agents demonstrate a higher degree of heterogeneity compared with organoids in the control and combination treatment groups (Figure 6.7A). As seen in the tumor growth curves (Figure 6.4E), combination treatment has an additive effect compared with single agent treatments and creates a uniform response in organoids based on the heterogeneity index (Figure 6.7A). Furthermore, spatial mapping provides insight into the relative locations of cell subpopulations, particularly for visualization of grouped versus scattered subpopulations. Representative images indicate that cell subpopulations are scattered across and within organoids. Ultimately, characterization of cellular heterogeneity provides a powerful tool for testing drugs and drug combinations.

Head and neck cancer patients suffer from severe toxicities, serious morbidities, and mortalities, and these challenges can be addressed through improved therapies. In particular,

streamlining the complex process of drug development could make a beneficial impact by efficiently identifying the most effective and least toxic drugs for development. This would reduce the time and resources spent on drugs that ultimately fail in patients and increase the success rate of clinical trials. A high-throughput drug screen based on cell metabolism and single cell analysis can address this need. Organoids combine the *in vitro* nature of cell monolayers with a more physiologically-relevant model, while optical metabolic imaging provides a platform for single-cell measurements of heterogeneous therapeutic response. This study establishes a protocol for growing head and neck cancer organoids, characterizes the organoids metabolically, and measures early response to antibody therapy, chemotherapy, and combination therapy. These results indicate that head and neck cancer organoids combined with optical metabolic imaging could provide a beneficial tool during drug discovery for head and neck cancer.

6.6 Acknowledgements

The Vanderbilt University Translational Pathology Shared Resource was used for immunohistochemistry staining. We acknowledge pathologist Dr. Kelli Boyd for help with interpreting these stains, and Joe Sharick for helpful discussions. Funding sources include the NSF Graduate Research Fellowship (DGE-0909667) and NIH/NCI (R01 CA185747).

CHAPTER 7

CONCLUSIONS AND FUTURE DIRECTIONS

6.1 Summary and Conclusions

The goal of this work is to develop optical metabolic imaging for measuring treatment response in head and neck cancer, which is a prominent cause of morbidities and mortalities. Current treatments cure only 50-60% of head and neck cancer patients [1]. Cancer drugs and drug combinations are continually being developed and approved, but there is a need for methods to match patients with the most beneficial drugs. Additionally, patients often experience initial response to treatment followed by relapse. Tumor heterogeneity can impact this treatment resistance [54][55], but current methods to measure treatment response focus on whole-body imaging. Single-cell measurements of treatment response would be beneficial to identify cell subpopulations that are responsible for patient relapse. Furthermore, cancer exhibits altered cellular metabolism [7], and metabolic measurements can resolve early treatment response. Overall, optical metabolic imaging could provide a tool that achieves single-cell metabolic measurements of anti-cancer treatment response using endogenous contrast. This technique could be applied to monitor early drug response, optimize personalized treatment regimens, and facilitate drug discovery for head and neck cancer.

Chapter 1 of this dissertation provides the motivation for this work. Chapter 2 provides background material for these studies. This chapter describes relevant information about the anatomy and physiology of the head and neck region, as well as the prevalence, diagnosis, and treatment methods for head and neck cancer. Additionally, optical techniques for head and neck cancer are described, and two-photon microscopy and fluorescence lifetime imaging are

introduced. Background information about cellular metabolism and tumor heterogeneity is also included.

Chapter 3 characterizes optical metabolic imaging in human cell lines for early assessment of treatment efficacy. The head and neck cancer cell lines SCC25 and SCC61 were treated with targeted therapies (cetuximab and BGT226) and chemotherapy (cisplatin) for 24 hours, and the optical redox ratio and fluorescence lifetimes of NAD(P)H and FAD were quantified. These molecular-level measurements that reflect cellular metabolism have potential to resolve anti-cancer treatment effects sooner than current imaging modalities, including CT, MRI, and PET. This early measurement of treatment efficacy could accelerate drug screening and identify optimal treatment regimens for individual patients, thereby improving patient outcomes.

Chapter 4 characterizes optical metabolic imaging for measuring response to head and neck cancer treatment *in vivo*. Feasibility of these measurements was demonstrated in a mouse model with head and neck cancer xenografts, and tumor heterogeneity was characterized. The mice were treated with chemotherapy, a targeted drug, or their combination and the fluorescence intensities and lifetimes of NAD(P)H and FAD were measured *in vivo* 48 hours after treatment. These studies provide support for clinical translation of optical metabolic imaging measurements in patients. In particular, a portion of head and neck cancer patients initially respond to treatment and then relapse over time. *In vivo* monitoring at early time-points could reduce unnecessary toxicities from ineffective treatments and improve the quality of life for head and neck cancer patients.

Chapter 5 translates optical metabolic imaging to human head and neck cancer tissue. Metabolic and structural measurements were acquired using the fluorescence lifetimes of

NAD(P)H and FAD as well as second harmonic generation (SHG) imaging. These methods probe the cancer cells and extracellular matrix, which are both components involved in treatment response. These measurements were characterized in patient tissue across multiple anatomical sites and cell types. This study indicates that optical metabolic imaging could provide a complementary microscopy method to conventional histology and influence treatment strategies for head and neck cancer patients.

Chapter 6 applies optical metabolic imaging to an organoid model of head and neck cancer. The optical redox ratio and fluorescence lifetimes of NAD(P)H and FAD were applied to characterize head and neck cancer organoids alone and after treatment with a chemotherapy, an antibody therapy, or their combination. Additionally, cellular heterogeneity of the organoids was analyzed. The organoid model serves as a more physiologically relevant *in vitro* platform compared with cell monolayers. Organoids more closely mimic *in vivo* conditions because they grow within a three-dimensional microenvironment that includes tumor-like gradients of oxygen, glucose, and pH [129]. Since a portion of HNSCC patients do not respond to treatments, prediction of effective treatments on an individual level could enable improved treatment outcomes. Patient tissue could be grown in organoids, incubated with several drugs and drug combinations, and measured with optical metabolic imaging to predict optimal treatment regimens. Additionally, optical metabolic imaging applied to organoids could be developed into a high-throughput screen to streamline drug discovery for head and neck cancer.

Improved measurement of treatment response in head and neck cancer has potential to optimize treatment regimens, reduce unnecessary morbidities and toxicities, and improve patient outcomes. Optical metabolic imaging harnesses intrinsic contrast to resolve early, single-cell response to anti-cancer treatment. In this dissertation, optical metabolic imaging has been applied

to head and neck cancer for *in vitro* cell lines, *in vivo* preclinical measurements, *ex vivo* human tissue, and three-dimensional organoids. Ultimately, this technique could optimize treatment planning and drug discovery for head and neck cancer.

6.2 Future Directions

Design a clinical system for head and neck cancer patients

Optical metabolic imaging is well-suited to head and neck cancer because of easy access to the site with endoscopes and fiber-optic probes. Chapter 4 demonstrates *in vivo* preclinical measurements in head and neck cancer xenografts for resolving early, cellular-level treatment response to therapy. Since treatment-induced changes in cellular metabolism are affected sooner than tumor volume, optical metabolic imaging can provide an earlier readout of response compared with current methods, like CT, MRI, and PET. Measuring the autofluorescence intensities and lifetimes of NAD(P)H and FAD in patients could resolve response at early time-points after treatment onset, enabling the reduction of unnecessary toxicities and costs from ineffective treatments.

Measure treatment-induced metabolic changes in head and neck cancer over a timecourse

Optical metabolic imaging is well-suited for measurements over time because it is non-destructive and can be applied for intact live samples. Chapter 4 applies optical metabolic imaging to head and neck cancer *in vivo* 48 hours after treatment with a chemotherapy, an antibody therapy, and their combination. Chapter 6 applies optical metabolic imaging in head and neck cancer organoids 24 hours after treatment with a chemotherapy, an antibody therapy,

and their combination. Timecourse measurements could provide insight about dynamic drug response, treatment-inducted shifts in cellular heterogeneity, and resistance to therapy.

Characterize head and neck cancer patient tissue *ex vivo*

Chapter 5 provides a preliminary study applying optical metabolic imaging and second harmonic generation (SHG) imaging to *ex vivo* human patient tissues. These tissues represent a variety of anatomical sites and cell types across several patients. Expanding this study by increasing the sample size for each anatomical site could provide additional insight into the variability that would be expected during clinical application of this technique. Additionally, this type of study would enable the characterization of NAD(P)H and FAD autofluorescence lifetime and SHG signals in primary human head and neck cancer tissue.

Characterize cellular subpopulations based on optical metabolic imaging

Cellular heterogeneity impacts treatment response in cancer patients because resistant cells can drive relapse. Optical metabolic imaging can be applied to identify cell subpopulations present intrinsically and after drug treatment. Chapter 4 characterizes cellular heterogeneity in head and neck cancer *in vivo*, and Chapter 6 characterizes cellular heterogeneity in head and neck cancer organoids. A better biological understanding of these subpopulations could be valuable for targeting treatment-resistant cells. Studies could be applied to correlate optical metabolic imaging parameters for cell subpopulations with complementary metabolic or protein expression measurements. Additionally, Appendix C introduces flow cytometry based on cell autofluorescence for sorting a heterogeneous solution of cells. This approach could be applied for cells from primary tumors. The sorted subpopulations of cells could be used during the

testing of potential drugs or for planning effective treatment regimens for individual cancer patients.

Optimize an organoid drug screen for patient-derived head and neck cancer tissue

Optical metabolic imaging in organoids can provide a predictive screen of potential drugs for informed, individualized treatment planning. Chapter 6 demonstrates optical metabolic imaging for head and neck cancer organoids grown from xenografts. Optimizing organoid generation methods and culture conditions could enable organoid growth from primary human tissue. This type of platform could enable patient-derived organoids to be tested with several drugs and drug combinations to predict treatment response before therapy is administered to the patient, which could improve patient outcomes.

Develop automated image acquisition for high-throughput studies

Drug development takes at least 10 years and more than $1 billion [115][116]. An organoid drug screen combined with optical metabolic imaging could provide a platform for rapid testing during drug discovery and identifying promising drug candidates. Chapter 6 applies optical metabolic imaging for head and neck cancer organoids after 24 hours of treatment with a chemotherapy, antibody therapy, and their combination. However, methods for acquiring and analyzing optical metabolic imaging data could be improved. In particular, automated image acquisition and data analysis could enable high-throughput screens to test an array of experimental drugs and their combinations. Additionally, three-dimensional image stacks could sample the entire organoid volume. Overall, this method could streamline drug discovery for head and neck cancer.

Develop the biological understanding of NAD(P)H and FAD fluorescence lifetime

The fluorescence lifetimes of NAD(P)H and FAD are still considered investigational measurements. A change in lifetime is usually interpreted as a change in microenvironment, particularly protein-binding. Chapter 3 correlates the fluorescence lifetimes of NAD(P)H and FAD with rates of cell proliferation and lactate production normalized by glucose consumption in head and neck cancer cell lines after treatment. Additional studies can explore the biological understanding of these fluorescence lifetime measurements, including how they change based on metabolic pathway preferences.

6.3 Contribution to the Field and Broader Impact

Contribution to Biophotonics

This work demonstrates novel characterizations of NAD(P)H and FAD autofluorescence intensities and lifetimes in head and neck cancer. Cyanide perturbation in the nonmalignant oral cavity cell line OKF6 verifies NAD(P)H and FAD autofluorescence by the optical redox ratio and NAD(P)H and FAD fluorescence lifetimes. These shifts match published results in the nonmalignant MCF10A cell line from the breast [52], but these results are previously unreported in cells from the oral cavity. Additionally, these studies represent the first reports of the effect of cetuximab on the optical redox ratio. No other literature has reported the effects of chemotherapy *in vivo* on the optical redox ratio and fluorescence lifetimes of NAD(P)H and FAD. Applying the viSNE dimensionality reduction technique to optical metabolic imaging is a novel approach to visualize cellular heterogeneity based on these parameters. These studies work toward interpreting the fluorescence lifetimes of NAD(P)H and FAD by comparing these measurements with gold standard measures of treatment response, including cell death and cell proliferation,

and glucose metabolism. This work also compares optical metabolic imaging parameters across head and neck cancer models, particularly between *in vivo* xenografts and organoids. Overall, this work strengthens the foundation of applying optical metabolic imaging to resolve treatment response in head and neck cancer.

Contribution to Head and Neck Cancer

This work presents the first reports of measurements of endogenous fluorescence in response to treatment in head and neck cancer. Single-cell measurements of cell metabolism are applied to resolve response to drug treatment, and these studies apply novel methods for characterizing tumor heterogeneity. A quantitative heterogeneity index is developed and applied to head and neck cancer tumors and organoids. This index is advantageous because there is no standard metric for quantifying tumor heterogeneity. Organoids combined with optical metabolic imaging, as presented in this work, could provide a novel assay for high-throughput metabolic measurements during drug discovery for head and neck cancer therapies.

Potential Impact

About half a million new cases of head and neck cancer are diagnosed each year. Only 50-60% of those patients will be cured by therapy [3], while the rest will show inherent resistance to therapy or develop resistance to therapy. Optical metabolic imaging harnesses intrinsic contrast of autofluorecence from cofactors that are sensitive to metabolic changes due to treatment. These studies characterize the optical metabolic imaging parameters in response to head and neck cancer treatment in human cell lines compared with gold standard measures of cellular metabolism and therapeutic response. Additionally *in vivo* studies demonstrate feasibility

for resolving response earlier than current methods based on tumor volume, and this approach can provide a basis for clinical translation of this technique for early monitoring of drug response *in vivo*. The sub-cellular resolution achieved by this technique could enable the identification of cellular sub-populations in response to treatment. Furthermore, translation of optical metabolic imaging to human patient tissues characterizes heterogeneity across tissue and cell types. In parallel, *in vitro* organoid studies develop a platform for testing drugs and drug combinations, an approach that could enable prediction of optimal therapy for individual patients before treatment is administered. Overall, optical metabolic imaging of head and neck cancer shows potential to impact personalized medicine and drug discovery for head and neck cancer. In particular, a sensitive measure of early treatment response could allow intervention during ineffective treatments. Clinical translation of an optical system to measure endogenous fluorescence is feasible because head and neck cancer sites are accessible with fiber optic probes. Additionally, high-throughput, physiologically-relevant platforms combined with optical metabolic imaging could facilitate drug discovery and predict optimal therapies to improve patient outcomes, minimize unnecessary toxicities, and reduce costs from ineffective therapies for head and neck cancer patients.

APPENDIX A

SUPPLEMENTARY MATERIAL FOR CHAPTER 4

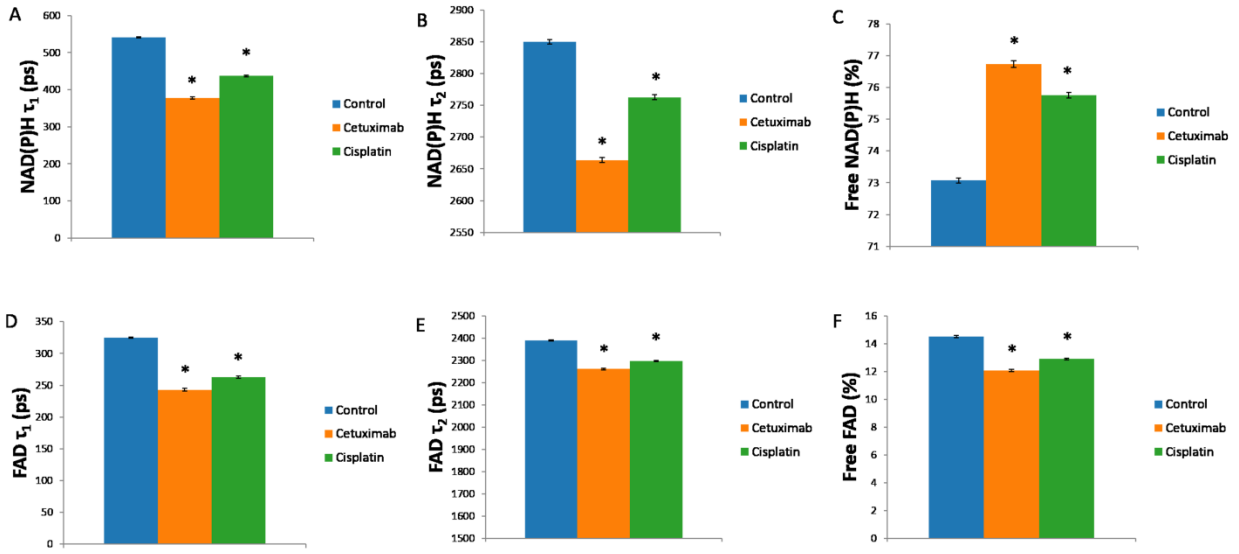

Figure A.1. The short fluorescence lifetime (τ_1), long fluorescence lifetime (τ_2), and contribution of free conformations of NAD(P)H and FAD 2 days after treatment. (A, B, D, E) The short and long lifetime components of NAD(P)H and FAD decrease with cetuximab and cisplatin treatment. (C, F) The contribution of free NAD(P)H increases and the contribution of free FAD decreases with cetuximab and cisplatin treatment. *$p<0.05$, compared with control

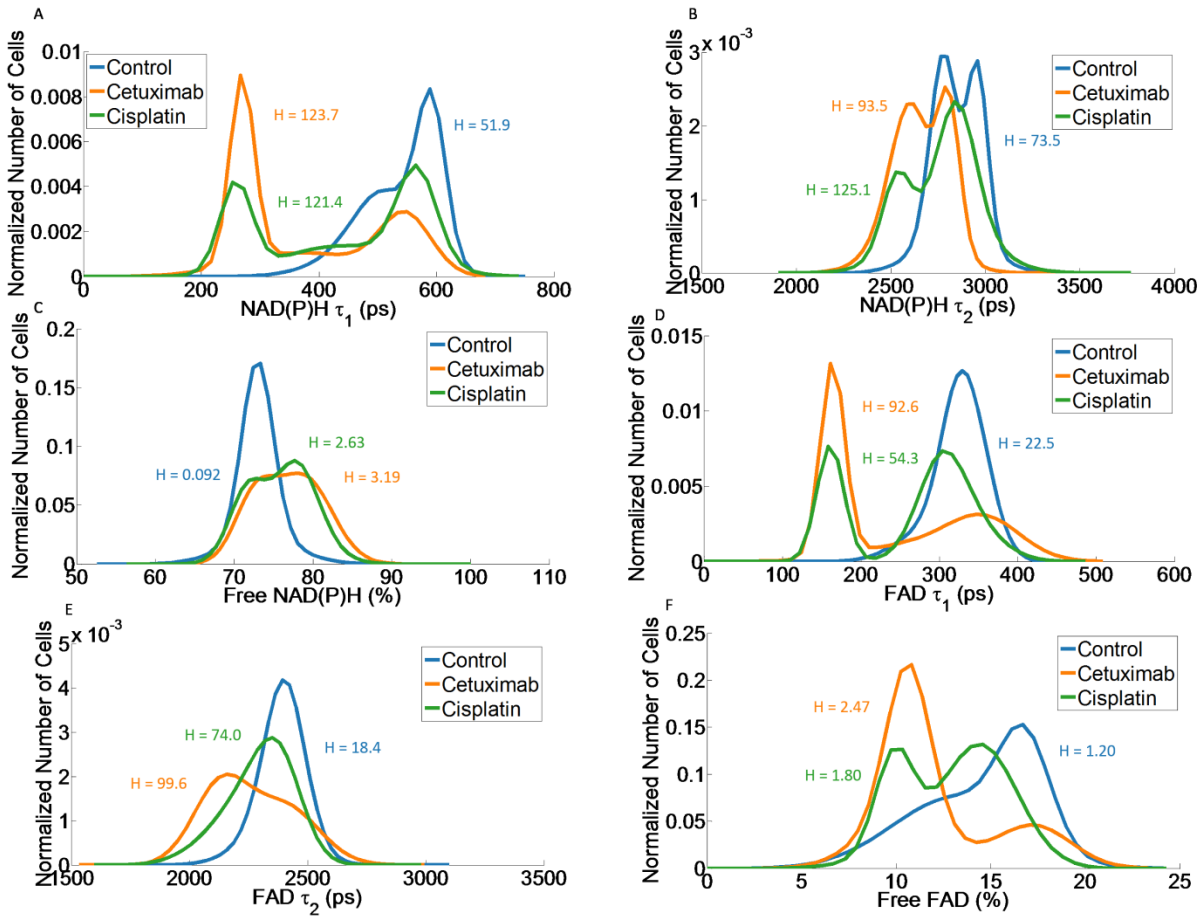

Figure A.2. The heterogeneity index was calculated for the short fluorescence lifetime (τ_1), long fluorescence lifetime (τ_2), and contribution of free conformations of NAD(P)H and FAD. For NAD(P)H τ_1, NAD(P)H τ_2, % free NAD(P)H, FAD τ_1, FAD τ_2, and % free FAD the control group exhibits decreased heterogeneity indices compared with the cetuximab and cisplatin treatment groups.

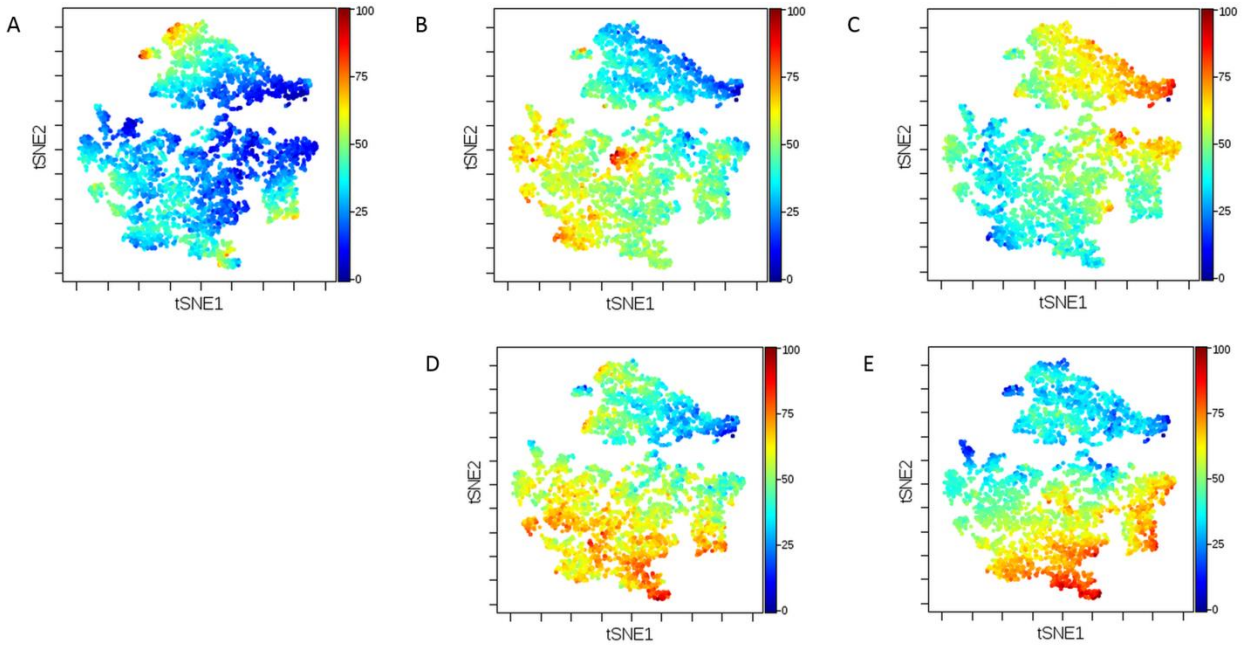

Figure A.3. ViSNE heat maps. Heat maps of (A) the redox ratio, (B) the long fluorescence lifetime component of NAD(P)H, (C) the contribution of free conformation of NAD(P)H , (D) the long fluorescence lifetime component of NAD(P)H, and (E) the contribution of free conformation of FAD over the 2-dimensional viSNE axes.

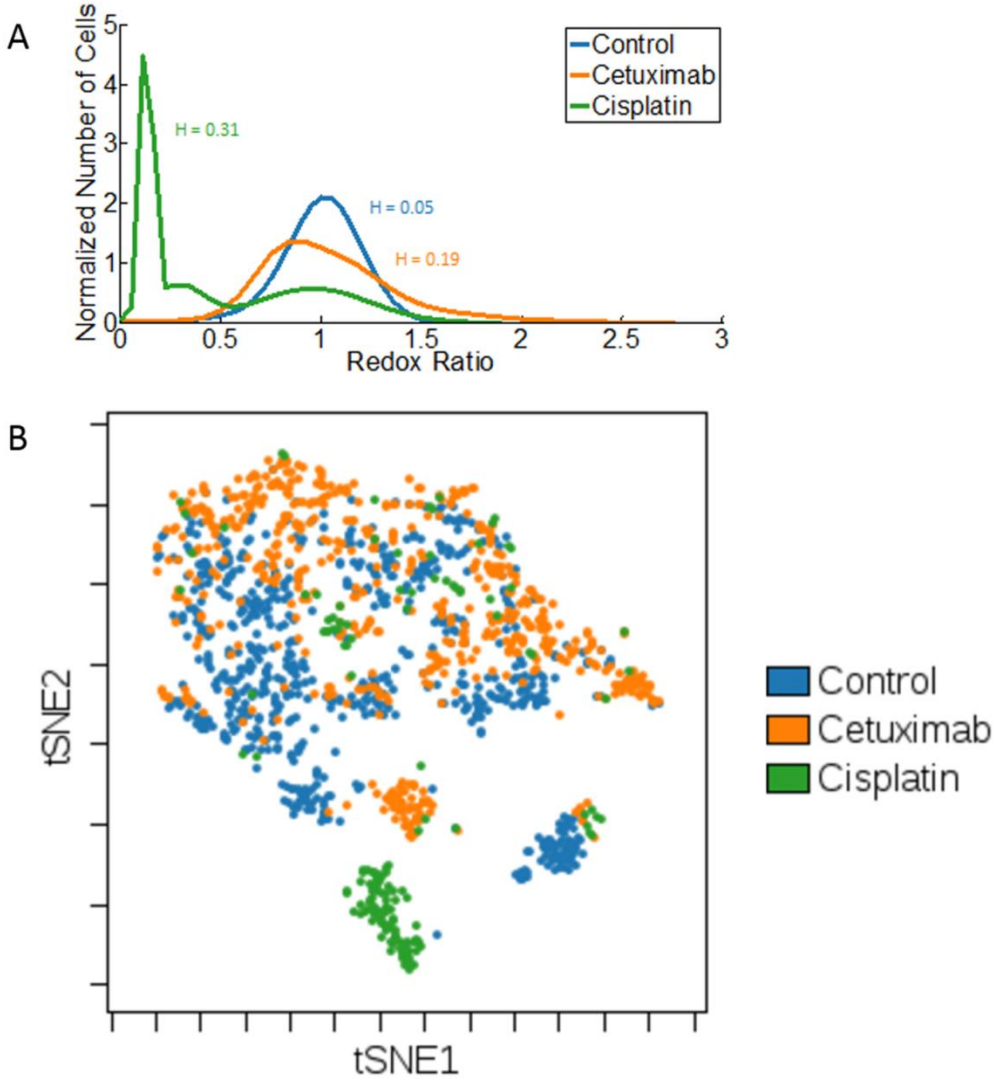

Figure A.4. Heterogeneity analysis for FaDu cell monolayers *in vitro* for cetuximab and cisplatin treatments compared with control. (A) The heterogeneity index based on the redox ratio is increased for cetuximab and cisplatin treatments compared with control. (B) ViSNE analysis shows overlap for control, cetuximab, and cisplatin groups as well as non-overlapping subpopulations for the cetuximab and cisplatin groups.

APPENDIX B

SUPPLEMENTARY MATERIAL FOR CHAPTER 6

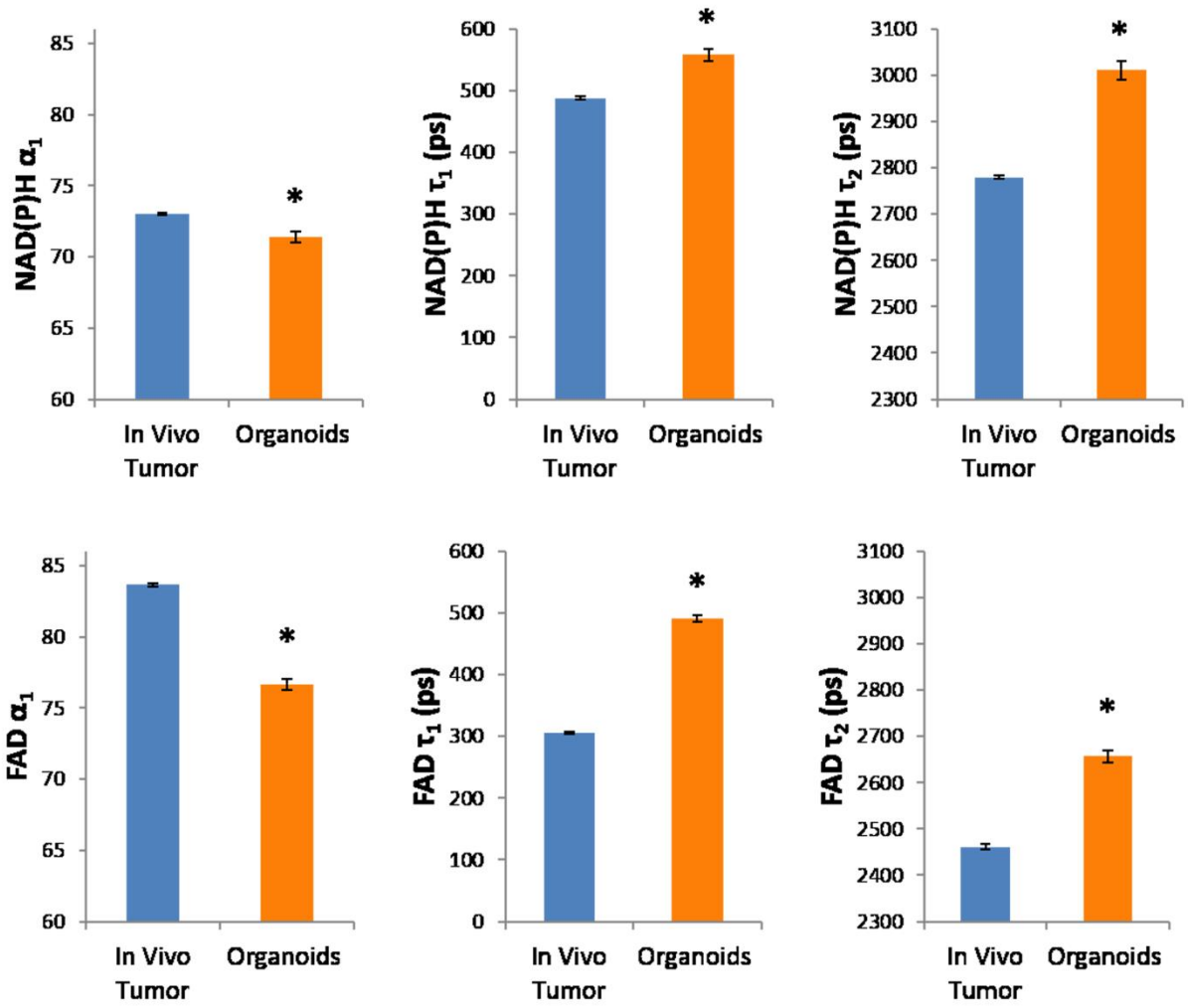

Figure B.1. Untreated organoids and *in vivo* tumor tissue exhibit distinct NAD(P)H and FAD fluorescence lifetime components. Organoids have lower contributions of the short lifetime component (α_1), higher values of the short fluorescence lifetime (τ_1), and higher values of the long fluorescence lifetime (τ_2). *$p<0.05$, t-test, n~100-300 cells per group

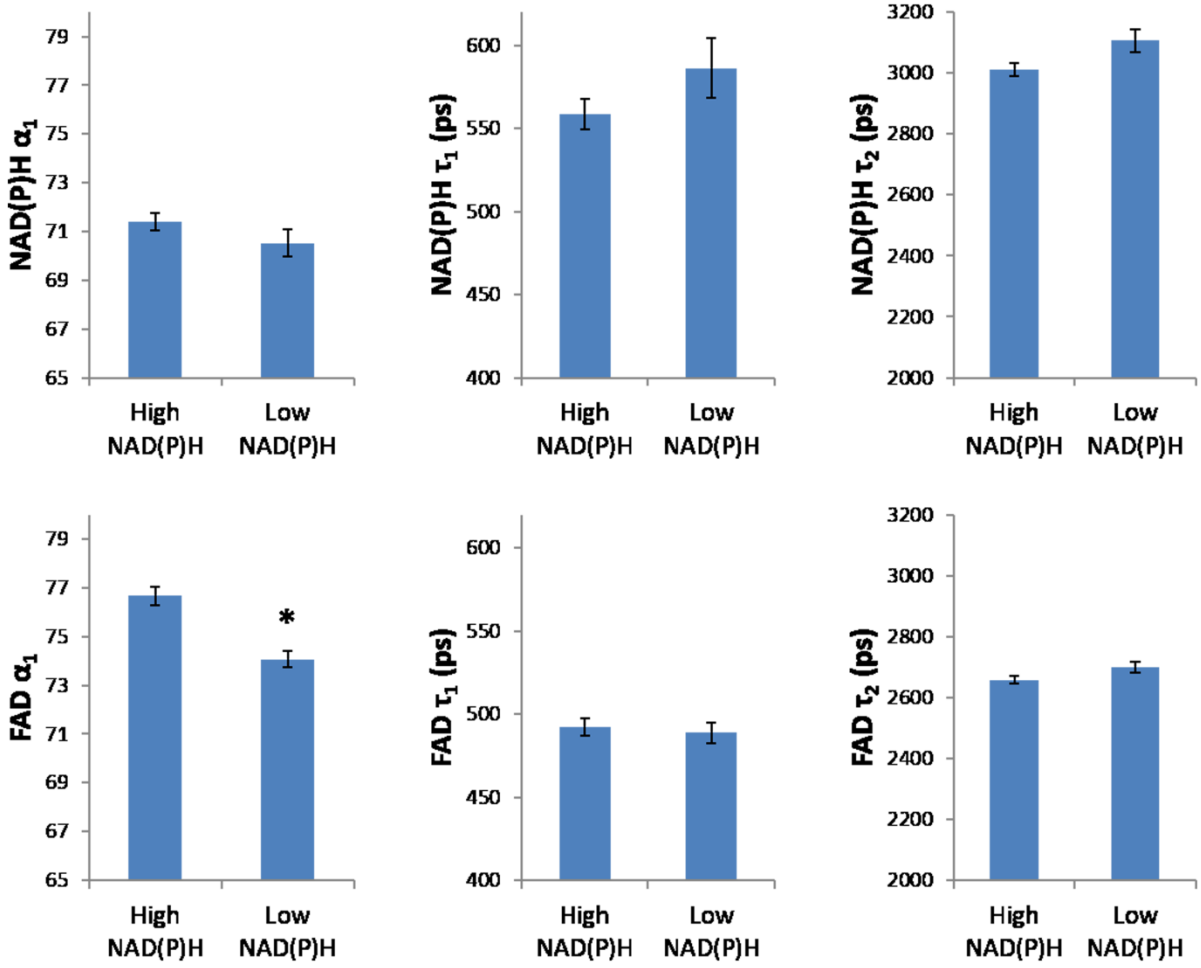

Figure B.2. NAD(P)H and FAD fluorescence lifetime components characterize cells in untreated organoids with low levels of NAD(P)H fluorescence compared with cells with high levels of NAD(P)H intensity. NAD(P)H fluorescence lifetime components are similar, whereas low NAD(P)H cells have lower contribution of FAD short lifetime component (α_1).

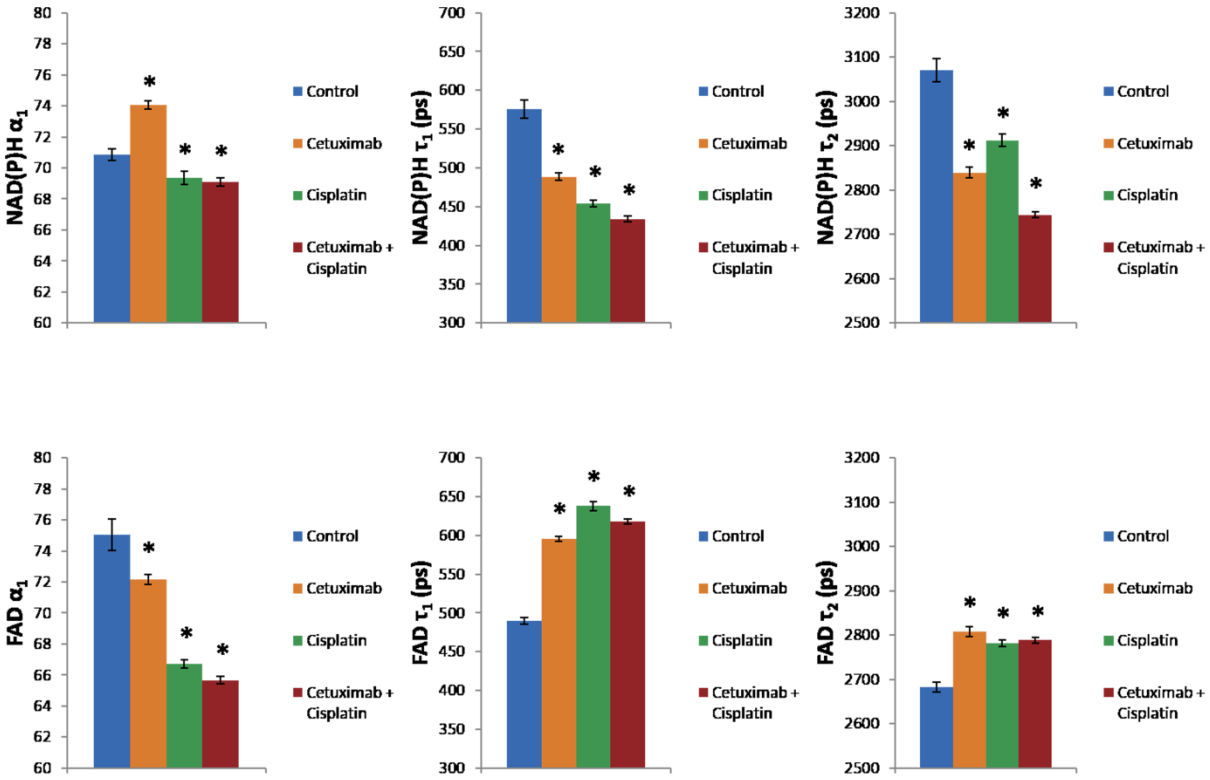

Figure B.3. NAD(P)H and FAD fluorescence lifetime components were quantified in organoids after 1 day of treatment. For NAD(P)H, cetuximab treatment causes an increase in the short lifetime component (α_1), whereas cisplatin and combination treatment cause a decrease in the short lifetime component. Cetuximab, cisplatin, and combination treatments cause a decrease in the short (τ_1) and long (τ_2) fluorescence lifetimes. For FAD, cetuximab, cisplatin, and combination treatments cause a decrease in the contribution of the short lifetime (α_1) and an increase in the short (τ_1) and long (τ_2) fluorescence lifetimes.

APPENDIX C

AUTOFLUORESCENCE FLOW SORTING OF BREAST CANCER CELL METABOLISM

C.1 Abstract

Clinical cancer treatment aims to target all cell subpopulations within a tumor. Autofluorescence microscopy of the metabolic cofactors NAD(P)H and FAD has shown sensitivity to anti-cancer treatment response. Alternatively, flow cytometry is attractive for high throughput analysis and flow sorting. This study characterizes cellular autofluorescence in three flow cytometry channels and applies cellular autofluorescence to sort a heterogeneous mixture of breast cancer cells into subpopulations enriched for each phenotype. Sorted cells were grown in culture and sorting was validated by morphology, autofluorescence microscopy, and receptor expression. Ultimately, this method could be applied to improve drug development and personalized treatment planning.

C.2 Introduction

Tumor heterogeneity can impact treatment response for cancer patients. Tumors can contain multiple subpopulations of cells with distinct phenotypes and sensitivities to drugs, and cells that are resistant to treatment can cause patient relapse [54]. The goal in clinical cancer treatment is to administer drugs that target all cell subpopulations within a tumor, leading to progression-free survival. Therefore, single-cell analysis techniques have become powerful tools for characterizing tumor heterogeneity and developing strategies to eliminate all treatment-resistant cells in a tumor.

Subpopulations of tumor cells can be defined by responsiveness or resistance to anti-cancer treatment. Responsive cells undergo cell death or senescence after treatment, whereas resistant cells continue to proliferate after treatment. Since cancer cells often exhibit altered cellular metabolism, particularly increased aerobic glycolysis (Warburg effect), and many drugs target metabolic pathways, cellular metabolism can be a marker for drug sensitivity [130]. Metabolic signaling pathways involve the cofactors NAD(P)H and FAD, and these molecules naturally exhibit autofluorescence. Previous studies have shown that breast cancer cells that are responsive to treatment exhibit a decreased ratio of NAD(P)H fluorescence to FAD fluorescence, termed the optical redox ratio, compared with cells that are resistant to treatment [52]. The redox ratio has also been used to distinguish subtypes of breast cancer cells with different receptor statuses, including human epidermal growth factor receptor 2 (HER2)-positive, estrogen receptor (ER)-positive, and triple negative cells. Specifically, the triple negative breast cancer cell line MDA-MB-231 has been shown to exhibit a lower optical redox ratio than the HER2-positive breast cancer cell line SKBr3 [52]. To mimic cellular heterogeneity, SKBr3 cells and MDA-MB-231 cells have been mixed in culture, and distinct subpopulations of each cell line have been identified using autofluorescence microscopy of NAD(P)H and FAD [98]. Therefore, single cell measurement techniques of cellular autofluorescence are beneficial to characterize heterogeneity across breast cancer subtypes.

Single cell techniques to measure fluorescence include microscopy and flow cytometry, and each of these has unique advantages. Microscopy provides higher resolution (sub-cellular) and requires a longer dwell time (ms), whereas flow cytometry provides lower resolution (cellular) and requires a shorter dwell time (μs). Microscopy measures smaller sample sizes (hundreds of cells) compared with flow cytometry (thousands of cells). Additionally, microscopy

measures adherent cells and can provide information about spatial relationships between cells, whereas flow cytometry measures cells in suspension and can sort cells to enrich cell subpopulations based on a target fluorophore. Overall, microscopy provides high signal to noise whereas flow cytometry provides high throughput and cell sorting. Flow cytometry is well-suited for characterizing cellular heterogeneity because sorting cancer cells by metabolic fluorophores could isolate subpopulations that could then be grown *in vitro* and used for further analysis. In particular, cell subpopulations could be tested for sensitivity to anti-cancer therapies to determine personalized treatment strategies as well as to develop new therapies for isolated resistant subpopulations.

Current methods for flow sorting tumor cell subpopulations are based on fluorescent staining for specific molecular markers, and some studies have identified markers for treatment resistance. In particular, CD44+ cells have been shown to be tumorigenic and resistant to chemotherapy in breast cancer, head and neck cancer, and pancreatic cancer [131][132][133][134]. CD24 has also been shown to be a marker for tumorigenic potential in breast cancer and pancreatic cancer. Additionally, CD133+ cells have been shown to be tumorigenic and resistant to chemotherapy in pancreatic cancer [135]. However, there are drawbacks to fluorophore staining for flow cytometry. In particular, labeling efficiency can affect the signal intensity from fluorophore staining, thus confounding the interpretation of "positive" and "negative" stained cells. Therefore, autofluorescence measurements can be beneficial by eliminating the need for dyes or stains. Additionally, staining for specific markers could miss cells that maintain treatment resistance yet circumvent the labeled pathway. Therefore, autofluorescence of NAD(P)H might be an advantageous marker to sort cells based on overall cell metabolism.

Previous studies have also applied flow cytometry based on intrinsic contrast. In addition to measuring cell fluorescence, flow cytometry measures scattering properties of the cells, including forward scattering measurements (FSC), which reflect cell size. These scattering properties have been used to distinguish cells of different sizes and types, including isolating neutrophils from leukocytes [136]. Additionally, NAD(P)H and FAD autofluorescence flow cytometry has been shown to measure response to increasing concentrations of glucose in rat b-cells, INS-1 cells, and rat islet cells [137][138]. Since flow cytometry measures fluorescence intensities per cell, cell size could affect autofluorescence measurements. For example, cells from the bottom ten percent of the autofluorescence intensity distribution have been shown to have decreased size compared with cells from the top ten percent [139]. Therefore, it is important to compare autofluorescence intensities from cells with similar sizes and FSC values.

This study applies flow cytometry for autofluorescence measurements of cell metabolism in breast cancer. Three flow cytometry channels were characterized for cellular autofluorescence in a nonmalignant breast cancer cell line after electron transport chain inhibition as well as between two breast cancer cell lines that exhibit either overexpression of HER2 or triple negative status. Additionally, a heterogeneous sample of these two cell lines was sorted based on cell autofluorescence, and the sorted subpopulations, which were enriched for each cell line, were grown in culture. Flow sorting was validated by cell morphology, autofluorescence microscopy, and staining for HER2 receptor expression. These results indicate that flow sorting by cell autofluorescence can separate phenotypic subpopulations of cells. Ultimately, this achievement could be applied to cells from patient tissue to enable more specific testing of tumor heterogeneity in cell subpopulations sorted by treatment response, ultimately driving improved treatment regimens for cancer patients.

C.3 Methods

Cell Culture

MCF10A cells were grown in Mammary Epithelial Cell Growth Medium (MEBM) supplemented with 1µg/ml insulin, 10ng/ml epidermal growth factor (EGF), and 1µg/ml hydrocortisone. MDA-MB-231 and SKBr3 cells were grown in Dulbecco's Modified Eagle Medium (DMEM) supplemented with 10% fetal bovine serum (FBS) and 1% penicillin:streptomycin. For flow cytometry experiments, cells were trypsinized and prepared as 10^6 cells in 1ml phosphate buffered saline (PBS) with 5% FBS. For the cyanide experiment, cyanide (4mM NaCN, Sigma) was added to the cell solution for 5 minutes. For flow sorting experiments, cells were prepared as $7*10^6$ cells in 1ml PBS with 5% FBS. Cells recovered from flow sorting were plated and grown on 35-mm glass-bottomed dishes (MatTek Corp.) for 1 week.

Flow Cytometry and Flow Sorting

The BD LSRII instrument was used for flow cytometry analysis experiments, and 3 fluorescence channels were analyzed. The DAPI channel used an excitation wavelength of 350nm and an emission filter of 450/50nm. The Alexa Fluor 405 channel used an excitation wavelength of 405nm and an emission filter of 450/50nm. The Alexa Fluor 488 channel used an excitation wavelength of 488nm and an emission filter of 505nm longpass. 10,000 cells were analyzed for each group. The BD FACSAria III instrument was used for flow sorting experiments, and 1 fluorescence channel was analyzed. The Alexa Fluor 405 channel used an excitation wavelength of 405nm and an emission filter of 450/50nm. Initial analysis was done on separate samples of MDA-MB-231 and SKBr3. Then the two cell lines were mixed at a ratio of 50% each, and the

heterogeneous solution was analyzed and sorted. For each cell line 3-5*10^5 cells were recovered after sorting. Cells were also analyzed post-sort. Graphs were made in Cytobank (www.cytobank.org). Experiments were repeated in triplicate on separate days, and results were consistent across experiments.

Microscopy Validation

Sorted cells were grown in culture for 1 week and imaged with brightfield and fluorescence microscopy. For brightfield microscopy, images were acquired using an inverted microscope (EVOS, Fisher Scientific) and 4X objective. For fluorescence microscopy, images were acquired using an inverted two-photon microscope (Bruker, and TiE, Nikon) and 40X oil-immersion objective (1.3 NA). Incident light was provided with a titanium:sapphire laser (Coherent, Inc.). A GaAsP photomultiplier tube (H7422P-40, Hamamatsu) was used to collect fluorescent photons. NAD(P)H was measured using an excitation wavelength of 750nm and an emission filter of 440/80nm. FAD was measured using an excitation wavelength of 890nm and an emission filter of 550/100nm. NAD(P)H and FAD were measured from the same fields of view. Each image averaged 4 frames, and 9 fields of view were imaged per group. Microscopy images were analyzed on a per-cell basis using a CellProfiler routine described previously [97]. Briefly, the optical redox ratio was calculated by dividing the image of NAD(P)H by the image of FAD for the same field of view. NAD(P)H images were thresholded to identify cell cytoplasms. NAD(P)H, FAD, and redox ratio images were quantified per cell.

HER2 Expression Validation

A fluorescently labeled anti-HER2 antibody, HER2Sense (5μM, PerkinElmer), was used to validate flow sorting. HER2Sense exhibits optimal excitation at 643nm and emission at 661nm. This fluorescence was measured with the Alexa 647 channel, which has an excitation wavelength at 633nm and a collection filter of 660/20nm. Cells were stained with HER2Sense for 30 minutes and washed with PBS. MDA-MB-231 and SKBr3 cells were characterized separately, mixed to form a heterogeneous solution, and sorted based on autofluorescence in the Alexa Fluor 405 channel. Next, sorted cells were characterized for autofluorescence in the Alexa Fluor 405 channel and for HER2 expression in the Alexa 647 channel. Sorted cells were grown for 1 week in culture, stained with HER2Sense for 30 minutes, washed with PBS, and imaged with an inverted confocal microscope (Meta, Zeiss) and 40X oil-immersion objective using the cy5 channel (maximal excitation and emission wavelengths of 647nm and 665nm). Pure, unstained MDA-MB-231 and SKBr3 cells served as negative controls for flow cytometry and confocal microscopy experiments.

Statistical Analysis

Bar graphs are shown as mean ± standard error. Statistical testing was performed using two-tailed t-tests with an α of 0.05 indicating statistical significance.

C.4 Results

Autofluorescence signals were measured in nonmalignant MCF10A cells after treatment with cyanide, which is an established metabolic perturbation (Figure C.1A). Cyanide inhibits the electron transport chain and prevents the conversion of NADH to NAD+, thereby causing an

accumulation of NADH [71]. NAD(P)H has an excitation maximum at 351nm and an emission maximum at 440nm [40]. These spectral properties align with the DAPI flow cytometry channel, which excites at 350nm and collects emission between 450/50nm. The Alexa Fluor 405 flow cytometry channel, which excites at 405nm and collects emission between 450/50nm, has also been used to measure NAD(P)H [140]. FAD has an excitation maximum at 450nm and an emission maximum at 535nm [40]. These spectral properties align with the Alexa Fluor 488 flow cytometry channel, which excites at 488nm and collects emission longer than 505nm. Flow cytometry data shows a slight increase in the DAPI channel. This is a small change and is consistent across three separate replicate experiments on different days. The Alexa Fluor 405 channel shows no change, indicating that this channel is less optimized for NAD(P)H measurements. The Alexa Fluor 488 channel shows a slight decrease. Additionally, the FSC measurements indicate that cell size is not affected by the cyanide treatment (Figure C.1B).

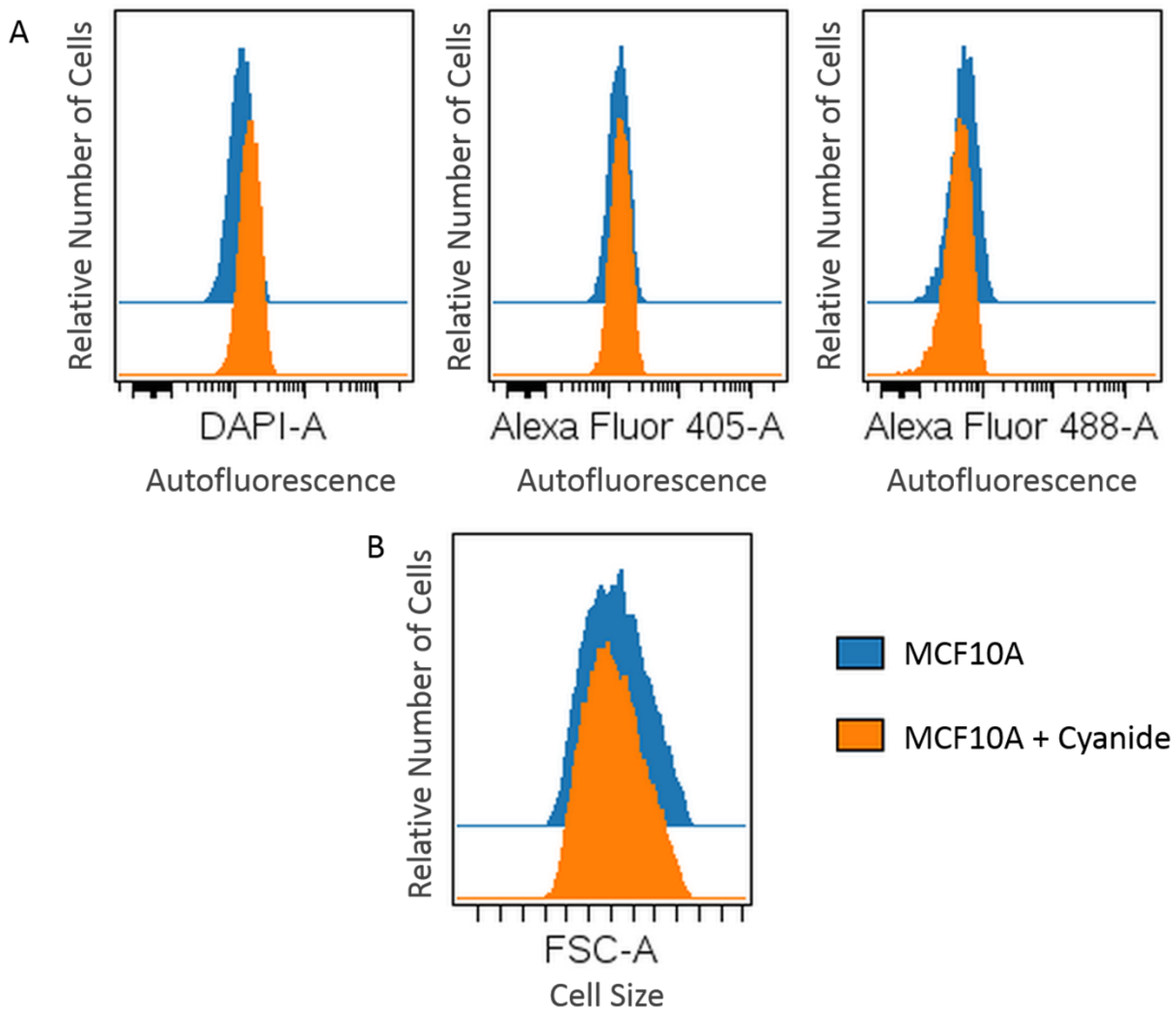

Figure C.1. Cyanide characterization. (A) Treatment with cyanide causes an increase in the DAPI channel, no change in the Alexa Fluor 405 channel, and a decrease in the Alexa Fluor 488 channel. (B) Treatment with cyanide has no effect on FSC measurements, which reflect cell size.

The triple negative breast cancer cell line MDA-MB-231 and the HER2-positive breast cancer cell line SKBr3 were characterized in the DAPI, Alexa Fluor 405, and Alexa Fluor 488 channels (Figure C.2A). The SKBr3 cells exhibit an increased fluorescence signal in the DAPI and Alexa Fluor 405 channels, which correspond to NAD(P)H, compared with MDA-MB-231

cells. SKBr3 cells show a slight increase in the Alexa Fluor 488 channel compared with MDA-MB-231 cells. The FSC measurements show similar cell sizes between the cell lines (Figure C.2B).

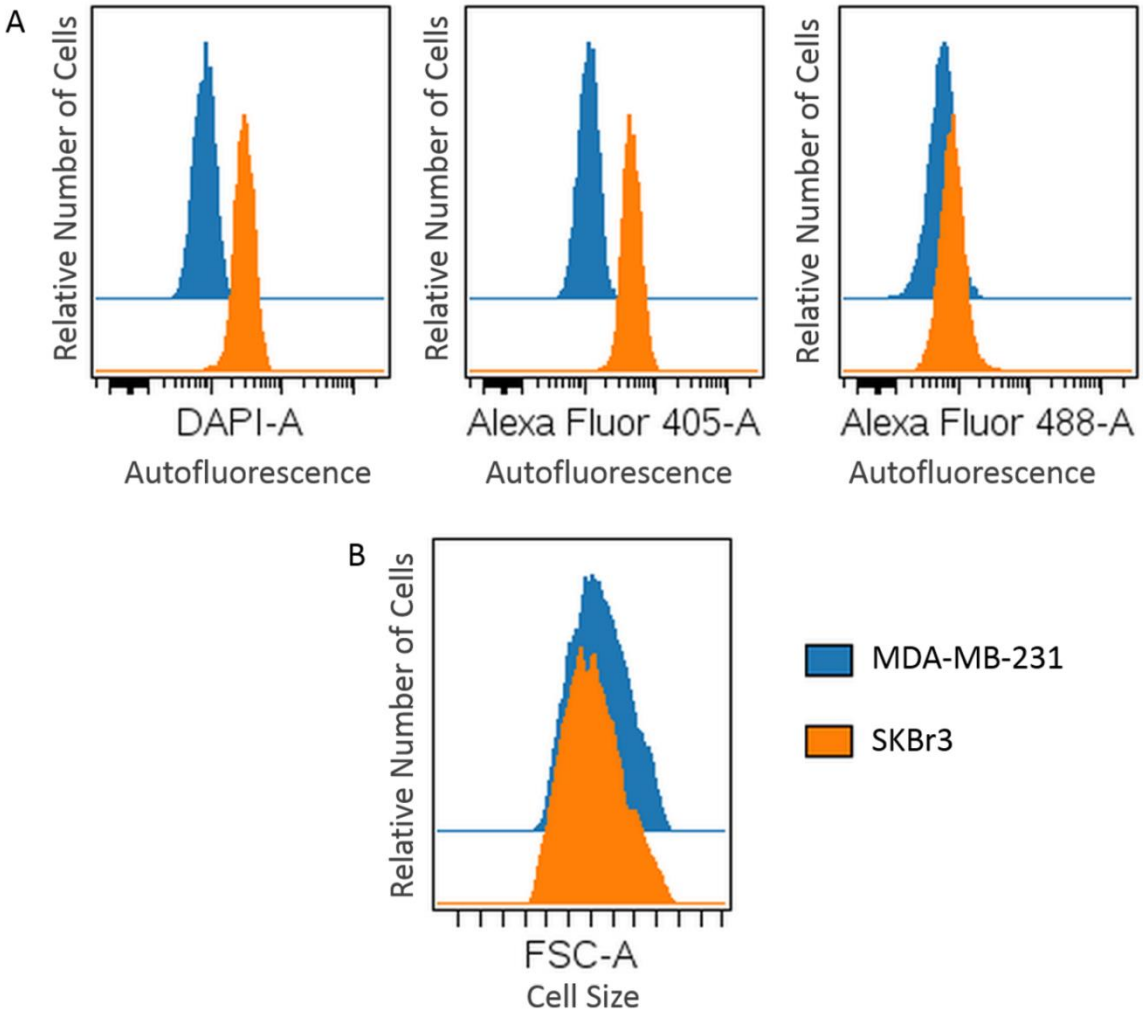

Figure C.2. Cell line characterization. (A) MDA-MB-231 cells exhibit lower fluorescence intensity in the DAPI, Alexa Fluor 405, and Alexa Fluor 488 channels compared with SKBr3 cells. (B) MDA-MB-231 and SKBr3 cells exhibit similar FSC measurements, which reflect cell size.

The distinct fluorescence intensities of MDA-MB-231 and SKBr3 cells in the Alexa Fluor 405 channel justifies applying this channel for sorting a heterogeneous sample of these two cell lines. Pure samples of MDA-MB-231 and SKBr3 cells show separate peaks for each cell line (Figure C.3A, blue, orange). The cell lines were mixed to create a heterogeneous sample, and this sample exhibits two distinct peaks that align with the peaks of each pure cell line (Figure C.3A, green). The sample was sorted based on fluorescence intensity in the Alexa Fluor 405 channel. Similarly, the sorted cell subpopulations exhibit peaks that align with the peaks of each pure cell line (Figure C.3A, red, purple). Error in the sorting was less than five percent based on post-sort analysis. FSC measurements indicate similar cell sizes between the MDA-MB-231 cells, SKBr3 cells, mixture of the two cell lines, and sorted SKBr3 cells (Figure C.3B). The sorted MDA-MB-231 cells exhibit slightly lower FSC values.

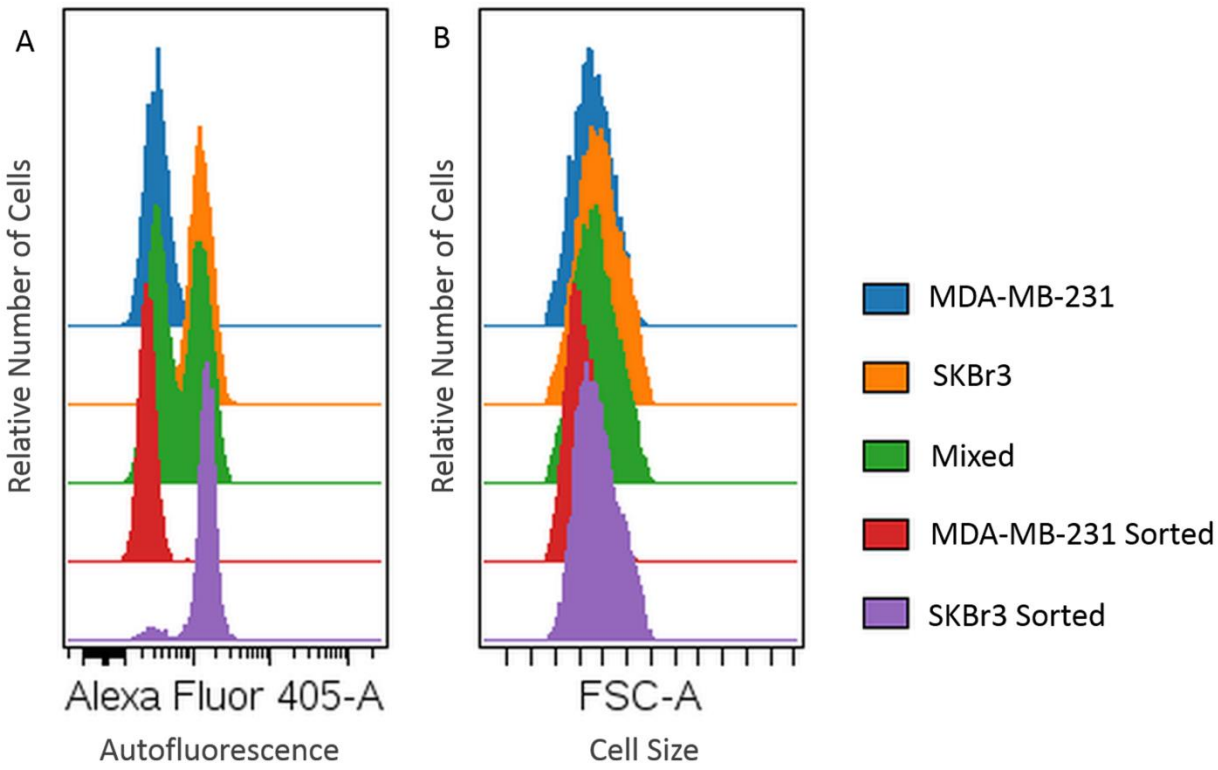

Figure C.3. Flow sorting. (A) MDA-MB-231 cells and SKBr3 cells measured separately exhibit distinct fluorescence intensities in the Alexa Fluor 405 channel. A mixture of MDA-MB-231 and SKBr3 cells exhibit two peaks, representing each cell type. Flow sorting the mixture separates the two populations of cell types. (B) FSC measurements show that MDA-MB-231, SKBr3, the mixture, and the sorted SKBr3 cells exhibit similar cell sizes. Sorted MDA-MB-231 cells exhibit a slightly decreased FSC measurement.

The sorted cell subpopulations were grown in culture for one week and validated with brightfield microscopy to visualize cell morphology (Figure C.4). Images show pure MDA-MB-231 cells exhibit an elongated morphology, whereas pure SKBr3 cells show a round and grouped morphology. Furthermore, the sorted cells from each subpopulation exhibit morphologies that align with the pure cell subpopulations.

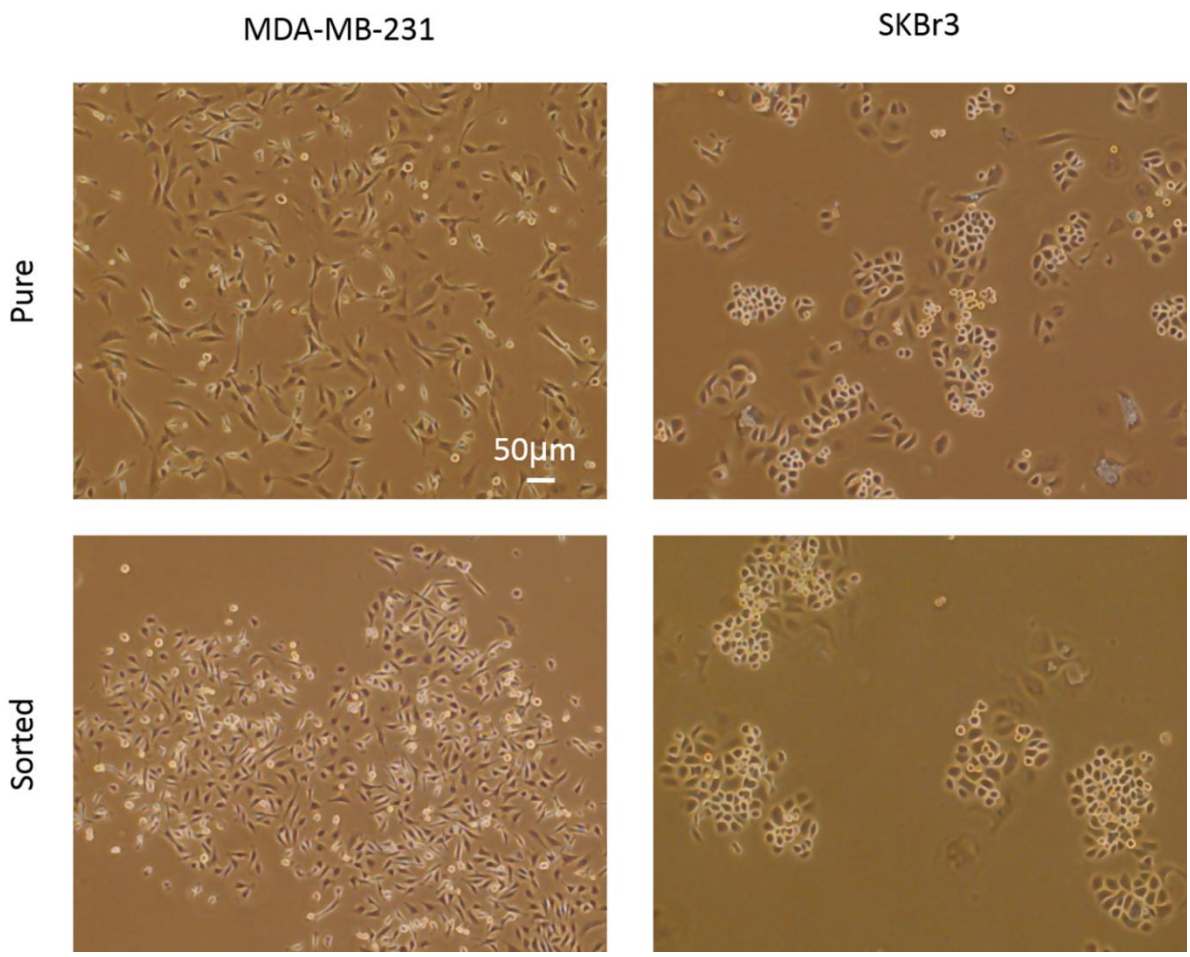

Figure C.4. Brightfield microscopy validates cell sorting. Images illustrate an agreement in morphology between pure and sorted MDA-MB-231 and SKBr3 cell lines.

Additionally, fluorescence microscopy was applied to validate cell sorting (Figure C.5). Sorted cells were grown in culture for a week and autofluorescence images of NAD(P)H and FAD were acquired. Representative images show the expected cell morphology for each cell line (Figure C.5A). The microscopy images were quantified on a cellular level to compare fluorescence intensities between the sorted cell subpopulations. The sorted SKBr3 cells exhibit higher NAD(P)H intensity (Figure C.5B), FAD intensity (Figure C.5C), and redox ratio (Figure C.5D) compared with MDA-MB-231 cells ($p<0.05$).

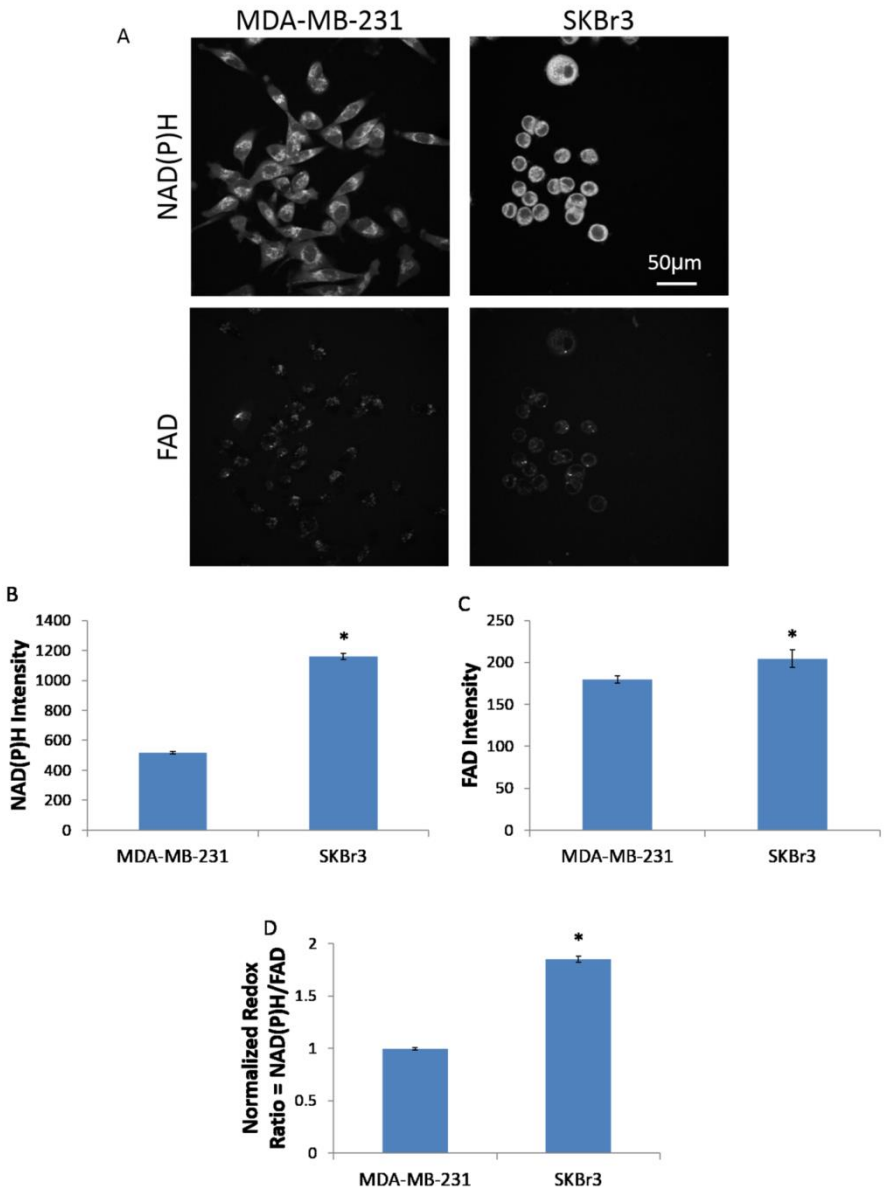

Figure C.5. Fluorescence microscopy validation of flow sorting a mixture of MDA-MB-231 and SKBr3 cells. (A) Representative images of NAD(P)H and FAD autofluorescence show the expected morphology from MDA-MB-231 and SKBr3 cells grown in culture for 1 week after flow sorting. (B, C) SKBr3 cells exhibit increased NAD(P)H and FAD intensities compared with MDA-MB-231 cells. (D) SKBr3 cells exhibit increased optical redox ratio (NAD(P)H/FAD) compared with MDA-MB-231 cells. n~170-200 cells. *$p<0.05$, t-test. mean+/- SEM

Fluorescence staining of HER2 expression was applied for a final validation of flow sorting (Figure C.6). HER2Sense labels HER2-positive cells, and excites and emits at wavelengths longer than NAD(P)H and FAD so it can be spectrally separated in the Alexa 647 channel. Flow sorting based on autofluorescence in the Alexa Fluor 405 channel was repeated with cells stained for HER2Sense (Figure C.6A). Unstained controls exhibit minimal fluorescence in the Alexa 647 channel (Figure C.6B, brown, pink). Stained SKBr3 cells exhibit increased fluorescence signal in the Alexa 647 channel compared with stained MDA-MB-231 cells (Figure C.6B, blue, orange). The cell lines were mixed, and the fluorescence profile of the mixture (Figure C.6B, green) matches the sum of the initial populations. The mixture was sorted based on autofluorescence in the Alexa Fluor 405 channel (Figure C.6A). After sorting, the Alexa 647 fluorescence for each subpopulation (Figure C.6B red, purple) matches the peaks for each pure cell line. FSC measurements (Figure C.6C) are similar across the samples, indicating similar cell sizes across the groups. Additionally, sorted cells were grown in culture for a week and fluorescence microscopy of HER2Sense was performed (Figure C.6D). Unstained controls show low background signal. As a positive control, stained SKBr3 cells show the localization of HER2 in the cell membrane, whereas stained MDA-MB-231 cells exhibit low signal. Similarly, sorted subpopulations of SKBr3 cells show the localization of HER2 in the cell membrane, whereas MDA-MB-231 cells exhibit low signal.

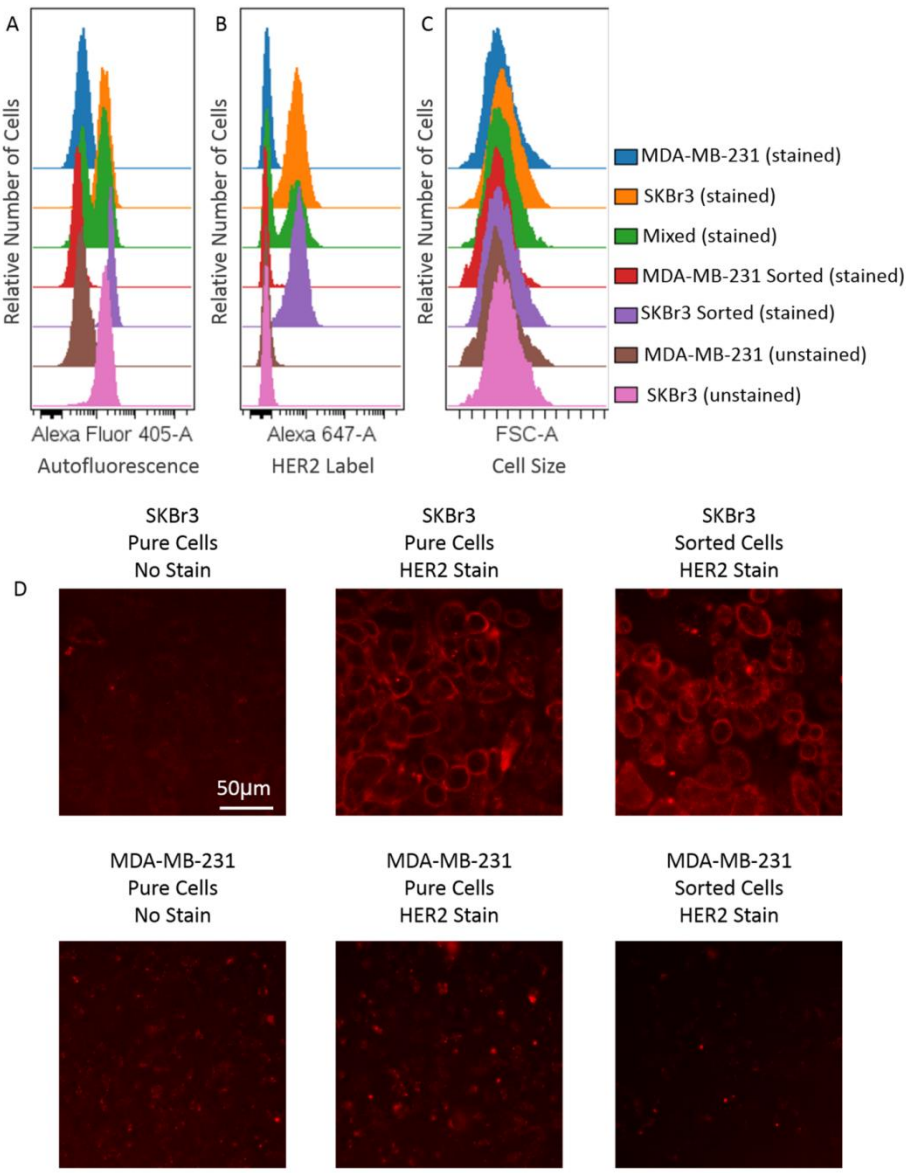

Figure C.6. HER2 staining validates flow sorting. (A) Autofluorescence in the Alexa Fluor 405 channel sorts a mixture of MDA-MB-231 and SKBr3 cells. (B) Staining with a fluorescent anti-HER2 antibody (HER2Sense) validates flow sorting. (C) FSC measurements indicate similar cell sizes across control and sorted groups. (D) Microscopy of sorted cells grown for 1 week shows the presence of HER2 in SKBr3 cell membranes compared with low, non-specific signal in MDA-MB-231 cells. "Stained" indicates cells were labeled with HER2Sense, whereas "unstained" indicates that cells were not labeled with HER2Sense.

C.5 Discussion

Tumor heterogeneity describes multiple subpopulations of cells within a tumor. Subpopulations of cells that are resistant to treatment can cause patient relapse. Therefore, sorting these subpopulations could enable improved treatment regimens that target all cell phenotypes. The goal of this study is to apply flow cytometry and flow sorting to breast cancer cell metabolism based on autofluorescence. This study characterizes the effect of the metabolic inhibitor cyanide on three autofluorescence channels. Additionally, the autofluorescence profiles of MDA-MB-231 triple negative breast cancer cells and SKBr3 HER2-positive breast cancer cells were measured using these flow cytometry channels. A heterogeneous mixture of these two cell lines was sorted into subpopulations enriched for each cell line based on autofluorescence flow cytometry. Sorting was validated with flow cytometry, brightfield microscopy, autofluorescence microscopy, and HER2 staining. Overall, this technique could be applied to tumor cells from patient tissue by separating subpopulations of cells, testing sensitivities to anti-cancer treatments, and planning optimal treatment schemes for individual patients.

Autofluorescence measurements using flow cytometry channels were characterized using a cyanide perturbation in MCF10A cells (Figure C.1). Previous studies using confocal microscopy have shown that electron transport chain inhibition with cyanide causes an increase in NAD(P)H intensity and a decrease in FAD intensity [53], and flow cytometry results show similar trends. Flow cytometry resolves a slight, consistent increase in the DAPI channel, which aligns with NAD(P)H fluorescence, and decrease in the Alexa Fluor 488 channel, which aligns with FAD fluorescence. However, flow cytometry exhibits a smaller magnitude of change compared with confocal microscopy results. These trends in the autofluorescence flow cytometry channels were also consistent after treatment with 5x and 10x higher doses of cyanide (data not

shown). This reflects a decrease in signal to noise for flow cytometry compared with high-resolution microscopy, due to shorter dwell times and lower spatial resolutions. As an additional consideration, flow cytometers are designed for use with bright fluorescent dyes and exhibit decreased sensitivity for the low fluorescence intensity of cellular autofluorescence. Furthermore, MCF10A cells are naturally adherent and could react differently to cyanide in suspension compared with in monolayer. Previous studies have applied the Alexa Fluor 405 channel to measure cell autofluorescence [139]. However, cyanide treatment causes no change in the Alexa Fluor 405 channel. These results indicate that the DAPI channel is more optimized for NAD(P)H measurements compared with the Alexa Fluor 405 channel. FSC measurements show no change after cyanide treatment, reflecting similar cell sizes and indicating that the changes in fluorescence intensities are not confounded with changes in cell size. These results characterize the three flow cytometry channels for cell autofluorescence measurements.

Flow cytometry measures distinct autofluorescence intensities between the triple negative MDA-MB-231 cell line and the HER2-positive SKBr3 cell line (Figure C.2). The DAPI and Alexa Fluor 405 channels exhibit increased fluorescence intensity in SKBr3 cells compared to MDA-MB-231 cells. This reflects increased NAD(P)H intensity and matches published redox ratio results from these cell lines using confocal microscopy [52]. Although the DAPI channel best aligns with the spectra properties of NAD(P)H, the 350nm laser is rare in flow cytometers and flow sorters, whereas the 405nm laser used in the Alexa Fluor 405 channel is common. The FSC measurements show no difference in cell size between the cell lines, which confirms that changes in NAD(P)H fluorescence intensity are not an artifact of cell size. Overall, the separation between MDA-MB-231 and SKBr3 cells in the Alexa Fluor 405 channel indicate that this channel could be used to sort these cell lines.

Flow sorting based on the Alexa Fluor 405 channel separates a heterogeneous mixture of breast cancer cells into subpopulations of HER2-positive SKBr3 cells and triple negative MDA-MB-231 cells (Figure C.3). The FSC measurements indicate a slightly smaller cell size for the sorted MDA-MB-231 cells. This could reflect the effect of cell size on autofluorescence intensity and highlights the importance of comparing autofluorescence intensity across cells with similar sizes. These results lay the foundation for future applications to dissociate cells from tumor tissue and sort subpopulations with different metabolic phenotypes, receptor statuses, and treatment sensitivities. Furthermore, the isolation of treatment-resistant cells could enable additional characterization of these cell subpopulations to identify targets for drug development as well as tests for sensitivity to drugs and drug combinations that aim to eliminate these resistant cells.

Brightfield microscopy, fluorescence microscopy, and HER2 staining provide additional validations for cell sorting. Cell morphologies of sorted cells grown for one week in culture align with morphologies of each pure cell line (Figure C.4) and are consistent with previous morphological studies of these cell lines grown on glass [141]. Autofluorescence characterization, particularly NAD(P)H fluorescence intensity, FAD fluorescence intensity, and redox ratio, of sorted subpopulations enriched for each cell type agrees with published confocal microscopy results from SKBr3 and MDA-MB-231 cell lines (Figure C.5) [52]. HER2 staining further validates the sorting of a heterogeneous mixture into subpopulations of each cell line (Figure C.6). Previous studies have shown that SKBr3 cells stained for HER2 expression exhibit positive membrane signal, whereas MDA-MB-231 cells exhibit minimal signal [142]. Flow cytometry and confocal microscopy of HER2Sense confirm increased HER2 expression in pure and sorted SKBr3 cells compared with pure and sorted MDA-MB-231 cells. Overall, these

microscopy and staining techniques confirm the separation of a heterogeneous mixture of breast cancer cell lines with distinct phenotypes into subpopulations enriched for each cell type based on autofluorescence flow sorting.

Tumors can contain cells with different receptor statuses, metabolic profiles, and responses to treatments. Cancer patients often exhibit relapse after treatment, which could be attributed to subpopulations of cells that are resistant to treatment. Single-cell measurements that reflect treatment response would allow improved treatment regimens for cancer patients. This study applies flow cytometry and flow sorting to nonmalignant breast cells, triple negative breast cancer cells, and HER2-positive breast cancer cells. These results characterize three flow cytometry channels for cell autofluorescence and indicate that flow cytometry based on cellular autofluorescence distinguishes two breast cancer cell lines with different receptor expressions. Furthermore, flow sorting based on cell autofluorescence separates a heterogeneous mixture into subpopulations enriched for each cell line. Ultimately, this technique could analyze cell heterogeneity from tumor tissue by sorting cell subpopulations based on metabolic profile. This method could be applied to preclinical studies for drug discovery, testing experimental drugs, and optimizing drug combinations. Furthermore, this method could be applied clinically to tissue from cancer patients to develop individualized treatment strategies and improve patient outcomes.

C.6 Acknowledgements

Flow cytometry experiments were performed in the Vanderbilt Medical Center (VMC) Flow Cytometry Shared Resource. The VMC Flow Cytometry Shared Resource is supported by the Vanderbilt Ingram Cancer Center (P30 CA68485) and Vanderbilt Digestive Disease Research

Center (DK058404). Confocal microscopy experiments were performed in the Cell Imaging Shared Research at Vanderbilt. Funding sources include the NSF Graduate Research Fellowship (DGE-0909667), Mary Kay Foundation (067-14), NIH/NCI (R01 CA185747), DoD (W81XWH-13-1-0194), and Vanderbilt University, as well as NCI GI Special Programs of Research Excellence P50 95103 and R01 CA163563 to RJC.

REFERENCES

[1] a Rousseau and C. Badoual, “Head and Neck: Squamous cell carcinoma: an overview,” *Atlas of Genetics and Cytogenetics in Oncology and Haematology*, no. 2. Mar-2012.

[2] N. C. I. at the N. I. of Health, “Head and Neck Cancers,” 2012. [Online]. Available: http://www.cancer.gov/cancertopics/factsheet/Sites-Types/head-and-neck.

[3] N. Zhang, K. Erjala, J. Kulmala, X. Qiu, M. Sundvall, K. Elenius, and R. Grénman, “Concurrent cetuximab, cisplatin, and radiation for squamous cell carcinoma of the head and neck in vitro.,” *Radiother. Oncol.*, vol. 92, no. 3, pp. 388–92, Sep. 2009.

[4] C. Fung and J. Grandis, “Emerging drugs to treat squamous cell carcinomas of the head and neck,” *Expert Opin Emerg Drugs*, vol. 15, no. 3, pp. 355–373, 2010.

[5] S. K. Kundu and M. Nestor, “Targeted therapy in head and neck cancer.,” *Tumour Biol.*, vol. 33, no. 3, pp. 707–21, Jun. 2012.

[6] L. B. Saltz, N. J. Meropol, P. J. Loehrer, M. N. Needle, J. Kopit, and R. J. Mayer, “Phase II trial of cetuximab in patients with refractory colorectal cancer that expresses the epidermal growth factor receptor.,” *J. Clin. Oncol.*, vol. 22, no. 7, pp. 1201–8, Apr. 2004.

[7] O. Warburg, “On the origin of cancer cells,” *Science (80-.).*, vol. 123, pp. 309–314, 1956.

[8] N. C. I. at the N. I. of Health, “Oropharyngeal Cancer Treatment,” 2012. [Online]. Available: http://www.cancer.gov/cancertopics/pdq/treatment/oropharyngeal/Patient/page1.

[9] R. Weinberg, *The Biology of Cancer*. Taylor & Francis, 2006.

[10] J. P. Shah and W. Lydiatt, “Treatment of cancer of the head and neck.,” *CA. Cancer J. Clin.*, vol. 45, no. 6, pp. 352–68.

[11] M. J. Hayat, N. Howlader, M. E. Reichman, and B. K. Edwards, “Cancer statistics, trends,

and multiple primary cancer analyses from the Surveillance, Epidemiology, and End Results (SEER) Program.," *Oncologist*, vol. 12, no. 1, pp. 20–37, Jan. 2007.

[12] J. Massano, F. S. Regateiro, G. Januário, and A. Ferreira, "Oral squamous cell carcinoma: review of prognostic and predictive factors.," *Oral Surg. Oral Med. Oral Pathol. Oral Radiol. Endod.*, vol. 102, no. 1, pp. 67–76, Jul. 2006.

[13] M. Gillison, "Human papillomavirus-associated head and neck cancer is a distinct epidemiologic, clinical, and molecular entity," *Semin Oncol*, vol. 31, no. 6, pp. 744–754, 2004.

[14] W. PC, A. KE, B. AT, and M. TR, "Carcinoma of the hypopahrynx: analysis of incidence and survival in Sweden over a 30-year period.," *Head Neck*, vol. 20, no. 8, pp. 714–719, 1998.

[15] J. Suen and S. Stern, "Cancer of the head and neck," *Cancer Head Neck*, vol. 462–484, 1996.

[16] S. Marur and A. a Forastiere, "Head and neck cancer: changing epidemiology, diagnosis, and treatment.," *Mayo Clin. Proc.*, vol. 83, no. 4, pp. 489–501, Apr. 2008.

[17] D. S. Salomon, R. Brandta, F. Ciardiellob, and N. Normannoc, "Epidermal growth factor-related peptides and their receptors in human malignancies," *Crit. Rev. Oncol. Hematol.*, vol. 19, no. 94, 1995.

[18] J. Bernier, S. M. Bentzen, and J. B. Vermorken, "Molecular therapy in head and neck oncology.," *Nat. Rev. Clin. Oncol.*, vol. 6, no. 5, pp. 266–77, May 2009.

[19] P. Harari, D. Wheeler, and J. Grandis, "Molecular Target Approaches in Head and Neck Cancer: EGFR and Beyond," *Semin Radiat Oncol*, vol. 19, no. 1, pp. 63–68, 2009.

[20] J. Egloff, Ann Grandis, "Targeting EGFR and Src Pathways in Head and Neck Cancer,"

Semin. Oncol., vol. 35, no. 3, pp. 286–297, 2008.

[21] C. Leemans, R. Tiwari, J. Nauta, I. van der Wall, and G. Snow, "Recurrence at the primary site in head and neck cancer and the significance of neck lymph node metastases as a prognostic factor," *Cancer*, vol. 73, no. 1, pp. 187–190, 1994.

[22] a Psyrri, M. Kwong, S. DiStasio, L. Lekakis, M. Kassar, C. Sasaki, L. D. Wilson, B. G. Haffty, Y. H. Son, D. a Ross, P. M. Weinberger, G. G. Chung, D. Zelterman, B. a Burtness, and D. L. Cooper, "Cisplatin, fluorouracil, and leucovorin induction chemotherapy followed by concurrent cisplatin chemoradiotherapy for organ preservation and cure in patients with advanced head and neck cancer: long-term follow-up.," *J. Clin. Oncol.*, vol. 22, no. 15, pp. 3061–9, Aug. 2004.

[23] P. M. Vila, C. W. Park, M. C. Pierce, G. H. Goldstein, L. Levy, V. V Gurudutt, A. D. Polydorides, J. H. Godbold, M. S. Teng, E. M. Genden, B. a Miles, S. Anandasabapathy, A. M. Gillenwater, R. Richards-Kortum, and A. G. Sikora, "Discrimination of Benign and Neoplastic Mucosa with a High-Resolution Microendoscope (HRME) in Head and Neck Cancer.," *Ann. Surg. Oncol.*, Apr. 2012.

[24] K. C. Maitland, A. M. Gillenwater, M. D. Williams, A. K. El-Naggar, M. R. Descour, and R. R. Richards-Kortum, "In vivo imaging of oral neoplasia using a miniaturized fiber optic confocal reflectance microscope.," *Oral Oncol.*, vol. 44, no. 11, pp. 1059–66, Nov. 2008.

[25] K. Sokolov, R. Drezek, K. Gossage, and R. Richards-Kortum, "Reflectance spectroscopy with polarized light: is it sensitive to cellular and nuclear morphology.," *Opt. Express*, vol. 5, no. 13, pp. 302–17, Dec. 1999.

[26] D. Heintzelman, U. Utzinger, and H. Fuchs, "Optimal excitation wavelengths for in vivo

detection of oral neoplasia using fluorescence spectroscopy," *Photochem Photobiol*, vol. 72, pp. 103–113, 2000.

[27] M. G. Müller, T. a Valdez, I. Georgakoudi, V. Backman, C. Fuentes, S. Kabani, N. Laver, Z. Wang, C. W. Boone, R. R. Dasari, S. M. Shapshay, and M. S. Feld, "Spectroscopic detection and evaluation of morphologic and biochemical changes in early human oral carcinoma.," *Cancer*, vol. 97, no. 7, pp. 1681–92, Apr. 2003.

[28] M. Huber, S. Bsoul, and G. Terezhalmy, "Acetic acid wash and chemiluminescent illumination as an adjunct to conventional oral soft tissue examination for the detection of dysplasia: pilot study," *Quntessence Int*, vol. 35, pp. 378–384, 2004.

[29] I. Pavlova, M. Williams, A. El-Naggar, R. Richards-Kortum, and A. Gillenwater, "Understanding the biological basis of autofluorescence imaging for oral cancer detection: high-resolution fluorescence microscopy in viable tissue.," *Clin. Cancer Res.*, vol. 14, no. 8, pp. 2396–404, Apr. 2008.

[30] Y. Sun, J. Phipps, D. S. Elson, H. Stoy, S. Tinling, J. Meier, B. Poirier, F. S. Chuang, D. G. Farwell, and L. Marcu, "Fluorescence lifetime imaging microscopy: in vivo application to diagnosis of oral carcinoma.," *Opt. Lett.*, vol. 34, no. 13, pp. 2081–3, Jul. 2009.

[31] M. C. Skala, K. M. Riching, D. K. Bird, A. Gendron-fitzpatrick, J. Eickhoff, K. W. Eliceiri, P. J. Keely, and N. Ramanujam, "In vivo Multiphoton Fluorescence Lfetime Imaging of Protein-bound and Free NADH in Normal and Pre-cancerous Epithelia," *JBO*, vol. 12, no. 2, pp. 1–19, 2007.

[32] M. C. Skala, K. M. Riching, A. Gendron-Fitzpatrick, J. Eickhoff, K. W. Eliceiri, J. G. White, and N. Ramanujam, "In vivo multiphoton microscopy of NADH and FAD redox states, fluorescence lifetimes, and cellular morphology in precancerous epithelia.," *Proc.*

Natl. Acad. Sci. U. S. A., vol. 104, no. 49, pp. 19494–9, Dec. 2007.

[33] J. M. Jabbour, S. Cheng, B. H. Malik, R. Cuenca, J. a Jo, J. Wright, Y.-S. L. Cheng, and K. C. Maitland, "Fluorescence lifetime imaging and reflectance confocal microscopy for multiscale imaging of oral precancer.," *J. Biomed. Opt.*, vol. 18, no. 4, p. 046012, Apr. 2013.

[34] J. Park, J. a Jo, S. Shrestha, P. Pande, Q. Wan, and B. E. Applegate, "A dual-modality optical coherence tomography and fluorescence lifetime imaging microscopy system for simultaneous morphological and biochemical tissue characterization.," *Biomed. Opt. Express*, vol. 1, no. 1, pp. 186–200, Jan. 2010.

[35] M. C. Skala, J. M. Squirrell, K. M. Vrotsos, C. Squamous, J. C. Eickhoff, A. Gendron-fitzpatrick, K. W. Eliceiri, and N. Ramanujam, "Multiphoton Microscopy of Endogenous Fluorescence Differentiates Normal , Precancerous , and Cancerous Squamous Epithelial Tissues Multiphoton Microscopy of Endogenous Fluorescence Differentiates Epithelial Tissues," pp. 1180–1186, 2005.

[36] J. Sun, T. Shilagard, B. Bell, M. Motamedi, and G. Vargas, "In vivo multimodal nonlinear optical imaging of mucosal tissue," *Opt. Express*, vol. 12, no. 11, pp. 2478–2486, 2004.

[37] E. E. Helman, J. R. Newman, N. R. Dean, W. Zhang, K. R. Zinn, and E. L. Rosenthal, "Optical imaging predicts tumor response to anti-EGFR therapy," *Cancer Biol. Ther.*, vol. 10, no. 2, pp. 166–171, Jul. 2010.

[38] J. P. Gleysteen, R. D. Duncan, J. S. Magnuson, J. B. Skipper, K. Zinn, and E. L. Rosenthal, "Fluorescently labeled cetuximab to evaluate head and neck cancer response to treatment.," *Cancer Biol. Ther.*, vol. 6, no. 8, pp. 1181–5, Aug. 2007.

[39] J. Lakowicz, *Principles of fluorescence spectroscopy*. New York: Plenum Publishers,

1999.

[40] N. Ramanujam, “Fluorescence spectroscopy of neoplastic and non-neoplastic tissues.,” *Neoplasia*, vol. 2, no. 1–2, pp. 89–117, 2000.

[41] W. Denk, J. Strickler, and W. Webb, “Two-photon laser scanning fluorescence microscopy,” *Science (80-.).*, vol. 248, pp. 73–76, 1990.

[42] F. Helmchen and W. Denk, “Deep tissue two-photon microscopy,” *Nat. Methods*, vol. 2, no. 12, pp. 932–940, 2005.

[43] Z. Benediktyová and L. Nedbal, “Imaging of multi-color fluorescence emission from leaf tissues.,” *Photosynth. Res.*, vol. 102, no. 2–3, pp. 169–75, 2009.

[44] LOCI and U. of Wisconsin-Madison, “Multiple-photon Excitation Fluorescence Microscopy,” 2013. [Online]. Available: http://loci.wisc.edu/optical-sectioning/multiple-photon-excitation-fluorescence-microscopy.

[45] J. R. Lakowicz, H. Szmacinski, K. Nowaczyk, and M. L. Johnson, “Fluorescence lifetime imaging of free and protein-bound NADH.,” *Proc. Natl. Acad. Sci. U. S. A.*, vol. 89, no. 4, pp. 1271–5, Feb. 1992.

[46] F. I. B Chance, B Schoener, R Oshino, “Oxidation-reduction ratio studies of mitochondria in freeze-trapped samples. NADH and flavoprotein fluorescence signals.,” *J. Biol. Chem.*, vol. 254, pp. 4764–4771, 1979.

[47] L. K. Klaidman, A. C. Leung, and J. D. Adams Jr., “High-performance liquid chromatography analysis of oxidized and reduced pyridine dinucleotides in specific brain regions,” *Anal. Biochem.*, vol. 228, pp. 312–317, 1995.

[48] Y. Avi-Dor, J. M. Olson, M. D. Doherty, and N. O. Kaplan, “Fluorescence of Pyridine Nucleotides in Mitochondria,” *J. Biol. Chem.*, vol. 237, no. 7, pp. 2756–2759, 1962.

[49] B. Chance, J. Williamson, D. Jamieson, and B. Schoener, “Properties and kinetics of reduced pyridine nucleotide fluorescence of the isolated and in vivo rat heart,” *Biochemistry*, vol. 341, pp. 357–377, 1965.

[50] I. Georgakoudi and K. P. Quinn, “Optical imaging using endogenous contrast to assess metabolic state.,” *Annu. Rev. Biomed. Eng.*, vol. 14, pp. 351–67, Jan. 2012.

[51] J. H. Ostrander, C. M. McMahon, S. Lem, S. R. Millon, J. Q. Brown, V. L. Seewaldt, and N. Ramanujam, “Optical redox ratio differentiates breast cancer cell lines based on estrogen receptor status.,” *Cancer Res.*, vol. 70, no. 11, pp. 4759–66, Jun. 2010.

[52] A. J. Walsh, R. S. Cook, H. C. Manning, D. J. Hicks, A. Lafontant, C. L. Arteaga, and M. C. Skala, “Optical metabolic imaging identifies glycolytic levels, subtypes, and early-treatment response in breast cancer.,” *Cancer Res.*, vol. 73, no. 20, pp. 6164–74, Oct. 2013.

[53] A. Walsh, R. S. Cook, B. Rexer, C. L. Arteaga, and M. C. Skala, “Optical imaging of metabolism in HER2 overexpressing breast cancer cells.,” *Biomed. Opt. Express*, vol. 3, no. 1, pp. 75–85, Jan. 2012.

[54] H. T. Khong and N. P. Restifo, “Natural selection of tumor variants in the generation of ‘tumor escape’ phenotypes.,” *Nat. Immunol.*, vol. 3, no. 11, pp. 999–1005, Nov. 2002.

[55] P. Puig, M. Guilly, A. Bouchot, N. Droin, D. Cathelin, F. Bouyer, L. Favier, F. Ghiringhelli, G. Kroemer, E. Solary, F. Martin, and B. Chauffert, “Tumor cells can escape DNA-damaging cisplatin through DNA endoreduplication and reversible polyploidy,” *Cell Biol. Int.*, vol. 32, no. 9, pp. 1031–1043, 2008.

[56] M. E. Prince, R. Sivanandan, a Kaczorowski, G. T. Wolf, M. J. Kaplan, P. Dalerba, I. L. Weissman, M. F. Clarke, and L. E. Ailles, “Identification of a subpopulation of cells with

cancer stem cell properties in head and neck squamous cell carcinoma.," *Proc. Natl. Acad. Sci. U. S. A.*, vol. 104, no. 3, pp. 973–978, 2007.

[57] B. Zhao, M. T. Hemann, and D. a Lauffenburger, "Intratumor heterogeneity alters most effective drugs in designed combinations.," *Proc. Natl. Acad. Sci. U. S. A.*, vol. 111, no. 29, pp. 10773–8, Jul. 2014.

[58] M. Machtay, J. Moughan, A. Trotti, A. S. Garden, R. S. Weber, J. S. Cooper, A. Forastiere, and K. K. Ang, "Factors associated with severe late toxicity after concurrent chemoradiation for locally advanced head and neck cancer: an RTOG analysis.," *J. Clin. Oncol.*, vol. 26, no. 21, pp. 3582–9, Jul. 2008.

[59] B. T. G. Wendt, G. G. Grabenbauer, C. M. Rbdel, H. Thiel, H. Aydin, R. Rohloff, T. P. U. Wustrow, H. Ira, C. Popella, and A. Schalhorn, "Alone in Advanced Head and Neck Cancer :," vol. 16, no. 4, pp. 1318–1324, 2013.

[60] J. M. G. Pedrero, D. G. Carracedo, C. M. Pinto, A. H. Zapatero, J. P. Rodrigo, C. S. Nieto, and M. V. Gonzalez, "Frequent genetic and biochemical alterations of the PI 3-K/AKT/PTEN pathway in head and neck squamous cell carcinoma.," *Int. J. Cancer*, vol. 114, no. 2, pp. 242–8, Mar. 2005.

[61] K.-Y. Chang, S.-Y. Tsai, C.-M. Wu, C.-J. Yen, B.-F. Chuang, and J.-Y. Chang, "Novel phosphoinositide 3-kinase/mTOR dual inhibitor, NVP-BGT226, displays potent growth-inhibitory activity against human head and neck cancer cells in vitro and in vivo.," *Clin. Cancer Res.*, vol. 17, no. 22, pp. 7116–26, Nov. 2011.

[62] B. T. Hennessy, D. L. Smith, P. T. Ram, Y. Lu, and G. B. Mills, "Exploiting the PI3K/AKT pathway for cancer drug discovery.," *Nat. Rev. Drug Discov.*, vol. 4, no. 12, pp. 988–1004, Dec. 2005.

[63] M. a Dickson, W. C. Hahn, Y. Ino, V. Ronfard, J. Y. Wu, R. a Weinberg, D. N. Louis, F. P. Li, and J. G. Rheinwald, "Human keratinocytes that express hTERT and also bypass a p16(INK4a)-enforced mechanism that limits life span become immortal yet retain normal growth and differentiation characteristics.," *Mol. Cell. Biol.*, vol. 20, no. 4, pp. 1436–47, Feb. 2000.

[64] J. G. Rheinwald and M. A. Beckett, "Tumorigenic Keratinocyte Lines Requiring Anchorage and Fibroblast Support Cultured from Human Squamous Cell Carcinomas Tumorigenic Keratinocyte Lines Requiring Anchorage and Fibroblast," pp. 1657–1663, 1981.

[65] K. H. Kim, F. Schwartz, and E. Fuchs, "Differences in keratin synthesis between normal epithelial cells and squamous cell carcinomas are mediated by vitamin A.," *Proc. Natl. Acad. Sci. U. S. A.*, vol. 81, no. 14, pp. 4280–4, Jul. 1984.

[66] R. Weichselbaum, W. Dahlberg, J. B. Little, T. J. Ervin, D. Miller, S. Hellman, and J. G. Rheinwald, "Cellular X-ray repair parameters of early passage squamous cell carcinoma lines derived from patients with known responses to radiotherapy.," *Br. J. Cancer*, vol. 49, no. 5, pp. 595–601, May 1984.

[67] L. Hu, D. Crowe, J. Rheinwald, P. Chambon, and L. Gudas, "Abnormal expression of retinoic acid receptors and keratin 19 by human oral and epidermal squamous cell carcinoma cell lines," *Cancer Res.*, vol. 51, pp. 3972–3981, 1991.

[68] R. B. Erlich, Z. Kherrouche, D. Rickwood, L. Endo-Munoz, S. Cameron, a Dahler, M. Hazar-Rethinam, L. M. de Long, K. Wooley, a Guminski, and N. a Saunders, "Preclinical evaluation of dual PI3K-mTOR inhibitors and histone deacetylase inhibitors in head and neck squamous cell carcinoma.," *Br. J. Cancer*, vol. 106, no. 1, pp. 107–15, Jan. 2012.

[69] T. Y. Seiwert, R. Jagadeeswaran, L. Faoro, V. Janamanchi, V. Nallasura, M. El Dinali, S. Yala, R. Kanteti, E. E. W. Cohen, M. W. Lingen, L. Martin, S. Krishnaswamy, A. Klein-Szanto, J. G. Christensen, E. E. Vokes, and R. Salgia, "The MET receptor tyrosine kinase is a potential novel therapeutic target for head and neck squamous cell carcinoma.," *Cancer Res.*, vol. 69, no. 7, pp. 3021–31, Apr. 2009.

[70] D. K. Bird, L. Yan, K. M. Vrotsos, K. W. Eliceiri, E. M. Vaughan, P. J. Keely, J. G. White, and N. Ramanujam, "Metabolic mapping of MCF10A human breast cells via multiphoton fluorescence lifetime imaging of the coenzyme NADH.," *Cancer Res.*, vol. 65, no. 19, pp. 8766–73, Oct. 2005.

[71] J. Eng, R. M. Lynch, and R. S. Balaban, "Nicotinamide adenine dinucleotide fluorescence spectroscopy and imaging of isolated cardiac myocytes Spectroscopy," vol. 55, no. April, 1989.

[72] W. G. Yarbrough, A. Whigham, B. Brown, M. Roach, and R. Slebos, "Phosphoinositide kinase-3 status associated with presence or absence of human papillomavirus in head and neck squamous cell carcinomas.," *Int. J. Radiat. Oncol. Biol. Phys.*, vol. 69, no. 2 Suppl, pp. S98–101, Jan. 2007.

[73] S. Huang, A. a Heikal, and W. W. Webb, "Two-photon fluorescence spectroscopy and microscopy of NAD(P)H and flavoprotein.," *Biophys. J.*, vol. 82, no. 5, pp. 2811–25, May 2002.

[74] R. Drezek, C. Brookner, I. Pavlova, I. Boiko, A. Malpica, R. Lotan, and R. Richards-kortum, "Auto fl uorescence Microscopy of Fresh Cervical-Tissue Sections Reveals Alterations in Tissue Biochemistry with Dysplasia ¶," vol. 73, no. 6, pp. 636–641, 2001.

[75] S. Banerjee and D. K. Bhatt, "Histochemical studies on the distribution of certain

dehydrogenases in squamous cell carcinoma of cheek," *Indian J. Cancer*, vol. 26, pp. 21–30, 1989.

[76] H. Kimura, K. Sakai, T. Arao, T. Shimoyama, T. Tamura, and K. Nishio, "Antibody-dependent cellular cytotoxicity of cetuximab against tumor cells with wild-type or mutant epidermal growth factor receptor.," *Cancer Sci.*, vol. 98, no. 8, pp. 1275–80, Aug. 2007.

[77] A. Eastman, "The mechanism of action of cisplatin: from adducts to apoptosis," in *Cisplatin. Chemistry and biochemistry of a leading anticancer drug*, 1999, pp. 111–134.

[78] J. M. Levitt, A. Baldwin, A. Papadakis, S. Puri, J. Xylas, K. Münger, and I. Georgakoudi, "Intrinsic fluorescence and redox changes associated with apoptosis of primary human epithelial cells.," *J. Biomed. Opt.*, vol. 11, no. 6, p. 064012, 2006.

[79] M. Nestor, "Effect of cetuximab treatment in squamous cell carcinomas.," *Tumour Biol.*, vol. 31, no. 2, pp. 141–7, Apr. 2010.

[80] M. Board, S. Humm, and E. a Newsholme, "Maximum activities of key enzymes of glycolysis, glutaminolysis, pentose phosphate pathway and tricarboxylic acid cycle in normal, neoplastic and suppressed cells.," *Biochem. J.*, vol. 265, no. 2, pp. 503–9, Jan. 1990.

[81] A. Marusyk and K. Polyak, "Tumor heterogeneity: causes and consequences.," *Biochim. Biophys. Acta*, vol. 1805, no. 1, pp. 105–17, Jan. 2010.

[82] D. Hanahan and R. a Weinberg, "Hallmarks of cancer: the next generation.," *Cell*, vol. 144, no. 5, pp. 646–74, Mar. 2011.

[83] N. Nakashima, K. Yoshihara, F. Tanaka, and K. Yagi, "Picosecond Fluorescence Lifetime of the Coenzyme of D-Amino Acid Oxidase"," *J Biol Chem*, vol. 255, no. 11, pp. 5261–5263, 1980.

[84] P. T. C. So, C. Y. Dong, B. R. Masters, and K. M. Berland, “Two-photon excitation fluorescence microscopy,” *Annu. rev. biomed. eng.*, pp. 399–429, 2000.

[85] C. Shannon, “A mathematical theory of communication,” *Bell Syst. Tech. J.*, vol. 27, pp. 379–423, 1948.

[86] A. Magurran, *Measuring biological diversity*. Malden:Blackwell, 2004.

[87] A. Marusyk, D. P. Tabassum, P. M. Altrock, V. Almendro, F. Michor, and K. Polyak, “Non-cell-autonomous driving of tumour growth supports sub-clonal heterogeneity,” *Nature*, vol. 514, no. 7520, pp. 54–58, Jul. 2014.

[88] V. Almendro, H. J. Kim, Y.-K. Cheng, M. Gönen, S. Itzkovitz, P. Argani, A. van Oudenaarden, S. Sukumar, F. Michor, and K. Polyak, “Genetic and phenotypic diversity in breast tumor metastases.,” *Cancer Res.*, vol. 74, no. 5, pp. 1338–48, Mar. 2014.

[89] M. D. Slack, E. D. Martinez, L. F. Wu, and S. J. Altschuler, “Characterizing heterogeneous cellular responses to perturbations.,” *Proc. Natl. Acad. Sci. U. S. A.*, vol. 105, no. 49, pp. 19306–11, Dec. 2008.

[90] S. C. Bendall, E. F. Simonds, P. Qiu, E. D. Amir, P. O. Krutzik, R. Finck, R. V Bruggner, R. Melamed, A. Trejo, O. I. Ornatsky, R. S. Balderas, S. K. Plevritis, K. Sachs, D. Pe, S. D. Tanner, and G. P. Nolan, “Single-Cell Mass Cytometry of Differential,” vol. 332, no. May, pp. 687–697, 2011.

[91] E. D. Amir, K. L. Davis, M. D. Tadmor, E. F. Simonds, J. H. Levine, S. C. Bendall, D. K. Shenfeld, S. Krishnaswamy, G. P. Nolan, and D. Pe’er, “viSNE enables visualization of high dimensional single-cell data and reveals phenotypic heterogeneity of leukemia.,” *Nat. Biotechnol.*, vol. 31, no. 6, pp. 545–52, Jun. 2013.

[92] I. Skvortsova, S. Skvortsov, U. Raju, T. Stasyk, O. Riesterer, E.-M. Schottdorf, B.-A.

Popper, B. Schiestl, P. Eichberger, P. Debbage, A. Neher, G. K. Bonn, L. a Huber, L. Milas, and P. Lukas, “Epithelial-to-mesenchymal transition and c-myc expression are the determinants of cetuximab-induced enhancement of squamous cell carcinoma radioresponse.,” *Radiother. Oncol.*, vol. 96, no. 1, pp. 108–15, Jul. 2010.

[93] B. M. Tijink, D. Neri, C. R. Leemans, M. Budde, L. M. Dinkelborg, M. Stigter-van Walsum, L. Zardi, and G. a M. S. van Dongen, “Radioimmunotherapy of head and neck cancer xenografts using 131I-labeled antibody L19-SIP for selective targeting of tumor vasculature.,” *J. Nucl. Med.*, vol. 47, no. 7, pp. 1127–35, Jul. 2006.

[94] M. a Joschko, L. K. Webster, J. F. Bishop, J. Groves, K. Yuen, I. N. Olver, K. N. Narayan, and D. L. Ball, “Radioenhancement by cisplatin with accelerated fractionated radiotherapy in a human tumour xenograft.,” *Cancer Chemother. Pharmacol.*, vol. 40, no. 6, pp. 534–9, Jan. 1997.

[95] D. K. Bird, L. Yan, K. M. Vrotsos, K. W. Eliceiri, E. M. Vaughan, P. J. Keely, J. G. White, and N. Ramanujam, “Metabolic mapping of MCF10A human breast cells via multiphoton fluorescence lifetime imaging of the coenzyme NADH.,” *Cancer Res.*, vol. 65, no. 19, pp. 8766–73, Oct. 2005.

[96] A. T. Shah, M. Demory Beckler, A. J. Walsh, W. P. Jones, P. R. Pohlmann, and M. C. Skala, “Optical metabolic imaging of treatment response in human head and neck squamous cell carcinoma.,” *PLoS One*, vol. 9, no. 3, p. e90746, Mar. 2014.

[97] A. J. Walsh and M. C. Skala, “An automated image processing routine for segmentation of cell cytoplasms in high-resolution autofluorescence images,” *SPIE Proc.*, p. 89481M, Feb. 2014.

[98] A. J. Walsh and M. C. Skala, “Optical metabolic imaging quantifies heterogeneous cell

populations," *Biomed. Opt. Express*, vol. 6, no. 2, p. 559, Jan. 2015.

[99] K. E. Diggins, P. B. Ferrell, and J. M. Irish, "Methods for discovery and characterization of cell subsets in high dimensional mass cytometry data," *Methods*, vol. 82, pp. 55–63, 2015.

[100] N. Kotecha, P. O. Krutzik, and J. M. Irish, "Web-based analysis and publication of flow cytometry experiments," in *Current Protocols in Cytometry*, J. P. Robinson, Ed. 2010.

[101] J. Szollosi, M. Balazs, B. Feuerstein, C. Benz, and F. Waldman, "ERBB-2 (HER2Ineu) Gene Copy Number, p185HER2 Overexpression, and Intratumor Heterogeneity in Human Breast Cancer '," *Cancer Res.*, vol. 55, pp. 5400–5407, 1995.

[102] B. J. Baselga, D. Pfister, M. R. Cooper, R. Cohen, B. Burtness, M. Bos, G. D. Andrea, A. Seidman, L. Norton, K. Gunnett, J. Falcey, V. Anderson, H. Waksal, and J. Mendelsohn, "Phase I Studies of Anti – Epidermal Growth Factor Receptor Chimeric Antibody C225 Alone and in Combination With Cisplatin," vol. 18, no. 4, pp. 904–914, 2000.

[103] B. Burtness, M. a Goldwasser, W. Flood, B. Mattar, and A. a Forastiere, "Phase III randomized trial of cisplatin plus placebo compared with cisplatin plus cetuximab in metastatic/recurrent head and neck cancer: an Eastern Cooperative Oncology Group study.," *J. Clin. Oncol.*, vol. 23, no. 34, pp. 8646–54, Dec. 2005.

[104] X. Li and Z. Fan, "The epidermal growth factor receptor antibody cetuximab induces autophagy in cancer cells by downregulating HIF-1alpha and Bcl-2 and activating the beclin 1/hVps34 complex.," *Cancer Res.*, vol. 70, no. 14, pp. 5942–52, Jul. 2010.

[105] M. Berndtsson, M. Hägg, T. Panaretakis, A. M. Havelka, M. C. Shoshan, and S. Linder, "Acute apoptosis by cisplatin requires induction of reactive oxygen species but is not associated with damage to nuclear DNA.," *Int. J. Cancer*, vol. 120, no. 1, pp. 175–80, Jan.

2007.

[106] E. Asselin, G. B. Mills, and B. K. Tsang, “XIAP Regulates Akt Activity and Caspase-3-dependent Cleavage during Cisplatin-induced Apoptosis in Human Ovarian Epithelial Cancer Cells 1,” pp. 1862–1868, 2001.

[107] I. K. Fodor, “A Survey of Dimension Reduction Techniques,” *US Dep. Energy*, 2002.

[108] L. Döbrossy, “Epidemiology of head and neck cancer: magnitude of the problem.,” *Cancer Metastasis Rev.*, vol. 24, no. 1, pp. 9–17, Jan. 2005.

[109] P. P. Hsu and D. M. Sabatini, “Cancer cell metabolism: Warburg and beyond.,” *Cell*, vol. 134, no. 5, pp. 703–7, Sep. 2008.

[110] I. Freund, M. Deutsch, and A. Sprecher, “Optical Second-harmonic Microscopy , Crossed-beam Summation , and Small-angle Scattering in Rat-tail Tendon,” *Biophys. J.*, vol. 50, pp. 693–712, 1986.

[111] I. Pavlova, M. Williams, A. El-Naggar, R. Richards-Kortum, and A. Gillenwater, “Understanding the biological basis of autofluorescence imaging for oral cancer detection: high-resolution fluorescence microscopy in viable tissue.,” *Clin. Cancer Res.*, vol. 14, no. 8, pp. 2396–404, Apr. 2008.

[112] D. C. G. De Veld, M. J. H. Witjes, H. J. C. M. Sterenborg, and J. L. N. Roodenburg, “The status of in vivo autofluorescence spectroscopy and imaging for oral oncology.,” *Oral Oncol.*, vol. 41, no. 2, pp. 117–31, Feb. 2005.

[113] T. Meyer, O. Guntinas-lichius, and F. Von Eggeling, “Multimodal nonlinear microscopic investigations on head and neck squamous cell carcinoma : Toward intraoperative imaging,” *Head Neck*, no. September, 2013.

[114] A. Trotti, “Toxicity in head and neck cancer: a review of trends and issues,” *Int. J. Radiat.*

Oncol. Biol. Phys., vol. 47, no. 1, pp. 1–12, 2000.

[115] J. P. Hughes, S. S. Rees, S. B. Kalindjian, and K. L. Philpott, "Principles of early drug discovery," *Br. J. Pharmacol.*, vol. 162, no. 6, pp. 1239–1249, 2011.

[116] S. M. Paul, D. S. Mytelka, C. T. Dunwiddie, C. C. Persinger, B. H. Munos, S. R. Lindborg, and A. L. Schacht, "How to improve R&D productivity: the pharmaceutical industry's grand challenge.," *Nat. Rev. Drug Discov.*, vol. 9, no. 3, pp. 203–214, 2010.

[117] N. Sachs and H. Clevers, "Organoid cultures for the analysis of cancer phenotypes," *Curr. Opin. Genet. Dev.*, vol. 24, no. 1, pp. 68–73, 2014.

[118] A. J. Walsh, R. S. Cook, M. E. Sanders, L. Aurisicchio, G. Ciliberto, C. L. Arteaga, and M. C. Skala, "Quantitative optical imaging of primary tumor organoid metabolism predicts drug response in breast cancer.," *Cancer Res.*, 2014.

[119] A. J. Walsh, J. A. Castellanos, N. S. Nagathihalli, N. B. Merchant, and M. C. Skala, "Optical Imaging of Drug-Induced Metabolism Changes in Murine and Human Pancreatic Cancer Organoids Reveals Heterogeneous Drug Response," *Pancreas*, vol. 00, no. 00, pp. 1–7, 2015.

[120] P. G. Sacks, "Cell , tissue and organ culture as in vitro models to study the biology of squamous cell carcinomas of the head and neck Normal UADT EpithelialCell Leukoplakia Ervthroalakia Carcinoma," pp. 27–51, 1996.

[121] M. Bucheler, C. Wirz, A. Schutz, and F. Bootz, "Tissue engineering of human salivary gland organoids," *Acta Otolaryngol*, vol. 122, no. 5, pp. 541–5, 2002.

[122] K. T. Robbins, N. M. Varki, A. M. Storniolo, H. Hoffman, and R. M. Hoffman, "Drug response of head and neck tumors in native-state histoculture," *Arch.Otolaryngol.Head Neck Surg.*, vol. 117, no. 0886–4470 (Print) LA - eng PT - Journal Article RN - 15663–

27–1 (Cisplatin) RN - 51–21–8 (Fluorouracil) SB - AIM SB - IM, pp. 83–86, 1991.

[123] A. T. Shah, K. E. Diggins, A. J. Walsh, J. M. Irish, and M. C. Skala, “In Vivo Autofluorescence Imaging of Tumor Heterogeneity in Response to Treatment,” *Neoplasia*, vol. 17, no. 12, pp. 862–870, 2015.

[124] F. Pampaloni, E. G. Reynaud, and E. H. K. Stelzer, “The third dimension bridges the gap between cell culture and live tissue.,” *Nat. Rev. Mol. Cell Biol.*, vol. 8, no. 10, pp. 839–845, 2007.

[125] K. Bayreuther, H. P. Rodemann, R. Hommel, K. Dittmann, M. Albiez, and P. I. Francz, “Human skin fibroblasts in vitro differentiate along a terminal cell lineage.,” *Proc. Natl. Acad. Sci. U. S. A.*, vol. 85, no. 14, pp. 5112–6, 1988.

[126] W. Lin and M. Karin, “A cytokine-mediated link between innate immunity , inflammation , and cancer,” *J. Clin. Investig.*, vol. 117, no. 5, pp. 1175–1183, 2007.

[127] P. F. Davies, A. Remuzzitt, E. J. Gordon, C. F. Dewey, and M. A. Gimbrone, “Turbulent fluid shear stress induces vascular endothelial cell turnover in vitro,” *Proc. Natl. Acad. Sci. U. S. A.*, vol. 83, no. April, pp. 2114–2117, 1986.

[128] L. C. Kimlin, G. Casagrande, and V. M. Virador, “In vitro three-dimensional (3D) models in cancer research: An update,” *Mol. Carcinog.*, vol. 52, no. 3, pp. 167–182, 2013.

[129] R. M. Sutherland, “Cell and environment interactions in tumor microregions: the multicell spheroid model.,” *Science*, vol. 240, no. 4849, pp. 177–84, Apr. 1988.

[130] Y. Zhao, E. B. Butler, and M. Tan, “Targeting cellular metabolism to improve cancer therapeutics,” *Cell Death Dis.*, vol. 4, no. 3, p. e532, 2013.

[131] X. Li, M. T. Lewis, J. Huang, C. Gutierrez, C. K. Osborne, M. F. Wu, S. G. Hilsenbeck, A. Pavlick, X. Zhang, G. C. Chamness, H. Wong, J. Rosen, and J. C. Chang, “Intrinsic

resistance of tumorigenic breast cancer cells to chemotherapy," *J. Natl. Cancer Inst.*, vol. 100, no. 9, pp. 672–679, 2008.

[132] M. Al-Hajj, M. Wicha, A. Benito-Hernandez, S. Morrison, and M. Clarke, "Prospective identification of tumorigenic breast cancer cells," *Proc. Natl. Acad. Sci. U. S. A.*, vol. 100, no. 7, 2003.

[133] M. E. Prince, R. S. A. Kaczorowski, G. T. Wolf, M. J. Kaplan, P. Dalerba, I. L. Weissman, M. F. Clarke, and L. E. Ailles, "Identification of a subpopulation of cells with cancer stem cell properties in head and neck squamous cell carcinoma," vol. 104, no. 3, 2007.

[134] C. J. Creighton, X. Li, M. Landis, J. M. Dixon, V. M. Neumeister, A. Sjolund, D. L. Rimm, H. Wong, A. Rodriguez, J. I. Herschkowitz, C. Fan, X. Zhang, X. He, A. Pavlick, M. C. Gutierrez, L. Renshaw, A. a Larionov, D. Faratian, S. G. Hilsenbeck, C. M. Perou, M. T. Lewis, J. M. Rosen, and J. C. Chang, "Residual breast cancers after conventional therapy display mesenchymal as well as tumor-initiating features.," *Proc. Natl. Acad. Sci. U. S. A.*, vol. 106, no. 33, pp. 13820–13825, 2009.

[135] P. C. Hermann, S. L. Huber, T. Herrler, A. Aicher, J. W. Ellwart, M. Guba, C. J. Bruns, and C. Heeschen, "Distinct Populations of Cancer Stem Cells Determine Tumor Growth and Metastatic Activity in Human Pancreatic Cancer," *Cell Stem Cell*, vol. 1, no. 3, pp. 313–323, 2007.

[136] D. a Dorward, C. D. Lucas, A. L. Alessandri, J. a Marwick, F. Rossi, I. Dransfield, C. Haslett, K. Dhaliwal, and A. G. Rossi, "Technical Advance: Autofluorescence-based sorting: rapid and nonperturbing isolation of ultrapure neutrophils to determine cytokine production.," *J. Leukoc. Biol.*, vol. 94, no. July, pp. 1–10, 2013.

[137] M. Van de Winkel and D. Pipeleers, “Autofluorescence-activated cell sorting of pancreatic islet cells: purification of insulin-containing B-cells according to glucose-induced changes in cellular redox state,” *Biochem. Biophys. Res. Commun.*, vol. 114, no. 2, 1983.

[138] M. S. Hanson, A. Steffen, J. S. Danobeitia, B. Ludwig, and L. a. Fernandez, “Flow cytometric quantification of glucose-stimulated B-cell metabolic flux can reveal impaired islet functional potency,” *Cell Transplant.*, vol. 17, no. 12, pp. 1337–1347, 2008.

[139] A. Tzur, J. K. Moore, P. Jorgensen, H. M. Shapiro, and M. W. Kirschner, “Optimizing optical flow cytometry for cell volume-based sorting and analysis,” *PLoS One*, vol. 6, no. 1, pp. 1–9, 2011.

[140] Y. Wu and J. Y. Qu, “Autofluorescence spectroscopy of epithelial tissues.,” *J. Biomed. Opt.*, vol. 11, no. 5, p. 054023, 2006.

[141] C. L. Sommers, S. W. Byers, E. W. Thompson, J. A. Torri, and E. P. Gelmann, “Differentiation state and invasiveness of human breast cancer cell lines,” *Breast Cancer Res Treat*, vol. 31, no. 2–3, pp. 325–335, 1994.

[142] J. Liu, J. Li, T. J. Rosol, X. Pan, and J. L. Voorhees, “Biodegradable nanoparticles for targeted ultrasound imaging of breast cancer cells in vitro,” *Phys. Med. Biol.*, vol. 52, no. 16, pp. 4739–47, 2007.